TUDelft

Delft University of Technology

A stable SPH discretization of the elliptic operator with heterogeneous coefficients

Lukyanov, Alexander; Vuik, Kees

Important note
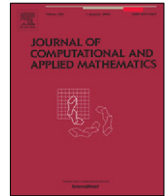To cite this publication, please use the final published version (if applicable).
Please check the document version above.

A stable SPH discretization of the elliptic operator with heterogeneous coefficients

Alexander A. Lukyanov *, Cornelis Vuik

Faculty of Electrical Engineering, Mathematics and Computer Science, Delft University of Technology, 2628 CD Delft, The Netherlands

ABSTRACT

Smoothed particle hydrodynamics (SPH) has been extensively used to model high and low Reynolds number flows, free surface flows and collapse of dams, study pore-scale flow and dispersion, elasticity, and thermal problems. In different applications, it is required to have a stable and accurate discretization of the elliptic operator with homogeneous and heterogeneous coefficients. In this paper, the stability and approximation analysis of different SPH discretization schemes (traditional and new) of the diagonal elliptic operator for homogeneous and heterogeneous media are presented. The optimum and new discretization scheme of specific shape satisfying the two-point flux approximation nature is also proposed. This scheme enhances the Laplace approximation (Brookshaw's scheme (1985) and Schwaiger's scheme (2008)) used in the SPH community for thermal, viscous, and pressure projection problems with an isotropic elliptic operator. The numerical results are illustrated by numerical examples, where the comparison between different versions of the meshless discretization methods are presented.

© 2020 Elsevier B.V. All rights reserved.

1. Introduction

Smoothed particle hydrodynamics (SPH) was developed a few decades ago to model inviscid fluid and gas flow dynamics in astrophysical problems [1–4]. The SPH is an interpolation-based numerical technique that can be used to solve systems of partial differential equations (PDEs) using either Lagrangian or Eulerian descriptions. The nature of SPH method allows to incorporate different physical and chemical effects into the discretized governing equations with relatively small code-development effort. In addition, geometrically complex and/or dynamic boundaries, and interfaces can be handled without undue difficulty. The SPH numerical procedure of calculating state variables (i.e., density, velocity, and gradient of deformation) is computed as a weighted average of values in a local region.

The SPH-method and its different variations are the basic type of a particle method. Those variations include a generalization of the finite difference method [5] (which can be used with arbitrary irregular meshes), diffuse element method (DEM) [6], element free Galerkin method (EFG) [7,8], meshless localized Petrov–Galerkin method [9–12], reproducing Kernel particle method [13–15], method of point interpolation [16–18,15], HP-cloud [19]), free meshless method [20]), and the points assemble method [21]. The method of fundamental solutions (MFS) has been used in the science and engineering community [22,23] including various form of the method of particular solutions (MPS) [24–26]. Recently, a number of different meshless techniques have been introduced. The boundary-type meshless collocation method called

---

* Corresponding author.
  E-mail address: a.lukyanov@tudelft.nl (A.A. Lukyanov).

singular boundary method (SBM) was introduced and applied for studying seismic wave scattering problems [27]. The backward substitution method (BSM) was developed and extended to solve multi-point problems [28], and fully nonlinear advection–diffusion–reaction problems [29]. A more detailed overview of different meshless methods can be found in [30–32].

Despite a few advantages of SPH method, this method is not free from disadvantages. For example, for fluids, gases, or solids with non-trivial boundaries there is incompleteness of the kernel support combined with the lack of consistency of the kernel interpolation in conventional meshless methods which results in fuzzy boundaries. In some cases, this can be fixed by an automatic incorporation of the boundary condition [1]. The completeness of mesh-free particle methods was discussed in [33]. However, care must be taken to ensure that variables whose values do not approach zero at boundaries are accurately represented.

It has been observed in the literature that meshless methods (e.g., SPH) are not free from instabilities, especially in the modeling solid mechanics problems. For example, the tensile instabilities were identified in [34] by performing the Neumann analysis of the one-dimensional governing equations (conservation laws). Therefore, different stabilization techniques have been developed. It is important to note at this point that it is very difficult to perform the general Neumann analysis in two- and three-dimensions. Furthermore, the high-frequency instability results from the low order discretization (rank deficient) of the divergence operator. The tensile instability results from the interaction between the second derivative of the Eulerian kernel (i.e., computed kernel in the Eulerian coordinates) and the tensile stress. The tensile instability only occurs for the Eulerian kernels because the Eulerian kernels depend on both the stress and the second derivative of the kernel. It has been shown [35] that in the case where the kernel is a function of the Lagrangian coordinates (the Lagrangian kernel), tensile instability does not occur. A comprehensive analysis on this subject can be found in [35]. Recently, some regularization and stabilization of SPH schemes were proposed in [36,37]. However, there is a lack of the mathematical analysis of these numerical techniques.

Since its introduction, SPH has been successfully used to model a wide range of fluid flows and the behavior of solids subjected to large deformations. For example, the SPH method was applied to simulate high energy explosions [38] and impact [39,40], most notably free surface flows and collapse of dams [41], elastoplasticity [42–44,40], to model low Reynolds number flows [45,46], to study pore-scale flow and dispersion [47,48], and for thermal problems [43,49,50]. A comprehensive overview of SPH applications to incompressible or nearly incompressible flow can be found in [51].

In different applications including, but not limited to, fluid flow related problems, it is required to have the stable and accurate discretization of the following operator (diagonal elliptic operator), which is the research subject of this paper:

$$\mathbf{L}(\mathbf{u}) = -\nabla \cdot (\mathbf{M}(\mathbf{r}) \nabla \mathbf{u}(\mathbf{r})) - g(\mathbf{r}), \quad \forall \mathbf{r} \in \Omega \subset \mathbb{R}^n,$$

$$\mathbf{M}(\mathbf{r}) \in \{\text{diag}[m(\mathbf{r})] : m(\mathbf{r}) \in \mathbb{R}_+^n, \ m(\mathbf{r}) \in L_2(\Omega)\}, \quad \text{diag} : \mathbb{R}^n \to \mathbb{R}^{n \times n},$$

(1)

where $\mathbf{u}(\mathbf{r})$ is the unknown scalar or vector variable field, $\mathbf{M}^{\alpha\beta}(\mathbf{r})$ is the diagonal matrix of the mobility field. For the reminder of the paper, lower-case Greek indices are used to describe the components of any tensor, the upper-case Latin indices are used for particle indices and lower-case Latin indices are used to describe the index of the Cartesian coordinates. One example of the mobility field includes $\mathbf{M}^{\alpha\beta}(\mathbf{r}) = m(\mathbf{r}) \delta_{\alpha\beta}$, $\alpha, \beta = 1, \dots, n$; where $m(\mathbf{r})$ is the mobility (or diffusivity, viscosity) scalar field, $\delta_{\alpha\beta}$ is the Kronecker symbol, $n = 1, 2, 3$ is the spatial dimension. It is important to note that we do not make any distinction between contravariant and covariant components of the any tensor in this paper by assuming that these tensors are defined in a Cartesian coordinate system. The sink/source term $g(\mathbf{r})$ is assumed to be zero in this paper. Consider the operator in the expression (1) with piecewise continuous coefficients $\mathbf{M}(\mathbf{r})$ in Ω. It has been noticed [52] that some of the numerical methods for elliptic equations may violate the maximum principle (i.e. lead to spurious oscillations). Therefore, proposed methods must satisfy a discrete maximum principle to avoid any spurious oscillations. This is also applicable to meshless discretizations. Usually, the oscillations are closely related to the poor approximation of the variable gradient $\nabla \mathbf{u}$ in the flux computation. In this paper, different numerical discretizations of the elliptic isotropic operator are analyzed. The objective of this paper is to develop numerical scheme satisfying the two-point flux approximation nature in the form

$$\mathbf{L}(\mathbf{u}) \approx \sum_J V_{\mathbf{r}_J} \Psi\left(\left[\mathbf{u}(\mathbf{r}_J) - \mathbf{u}(\mathbf{r}_I)\right], \mathbf{r}_J - \mathbf{r}_I\right) - g(\mathbf{r}_I),$$

(2)

where J is the neighboring particle of the particle I, $V_{\mathbf{r}_J}$ is the J-particle volume, Ψ is the special kernel. This structure (2) allows to have a better analysis of the stability and monotonicity. Furthermore, this will allow to apply upwinding strategy during the solution of nonlinear PDEs. The new optimum (i.e., high order scheme with monotonicity property) discretization scheme of the shape (2) is proposed in this paper. This scheme is based both on the Laplace approximation (Brookshaw's scheme [53]) and on a gradient approximation commonly used in the SPH community for thermal, viscous, and pressure projection problems. The proposed discretization scheme is combined with mixed corrections, which ensure linear completeness. The mixed correction utilizes Shepard Functions in combination with a correction to derivative approximations. In corrected meshless methods, the domain boundaries and field variables at the boundaries are approximated with the improved accuracy comparing to the conventional SPH method. The resulting new scheme improves the particle deficiency (kernel support incompleteness) problem. The outline of the paper is as follows. In Section 2, the existing discretizations of the Laplace operator with the building blocks necessary for these methods are

discussed. In this section, the SPH kernel and its gradient properties are also discussed. The description of meshless transmissibilities and their connections to the existing mesh-dependent discretization schemes is given in Section 3 including the construction of a new meshless discretization scheme. The approximation, stability, and monotonicity analysis are performed in Section 4. The numerical analysis of different boundary value problems is presented in Section 5. The paper is concluded by Section 6.

2. SPH discretization of the Laplace operator

The meshless approximations (SPH approximations) to the operator (1) with heterogeneous and homogeneous coefficients are presented in this section. Let us consider a rectangle in $\mathbb{R}^n$, $n = 1, 2, 3$:

$$\Omega = \left\{ \boldsymbol{r} = \{x_\alpha\} \in \mathbb{R}^n \mid \quad 0 < |x_\alpha - a_\alpha| \le l_\alpha, \ l_\alpha \in \mathbb{R}_+, \quad \forall \alpha = 1, \ldots, n \right\} \tag{3}$$

as the numerical domain. Here, a_α are the center coordinates of the rectangular and l_α are the side lengths. The following $L_p\left(\bar{\Omega}\right)$, $L_p\left(\tilde{\Omega}\right)$ norms are used to quantify the accuracy of different approximations for the entire numerical domain Ω:

$$\|\mathbf{f}\|_{\bar{\Omega}}^p = \left(\sum_{\boldsymbol{r}_K \in \bar{\Omega}} V_{\boldsymbol{r}_K} \left(|\mathbf{f}|\right)^p \right)^{\frac{1}{p}}, \qquad \|\mathbf{f}\|_{\tilde{\Omega}}^p = \left(\sum_{\boldsymbol{r}_K \in \tilde{\Omega}} V_{\boldsymbol{r}_K} \left(|\mathbf{f}|\right)^p \right)^{\frac{1}{p}}, \tag{4}$$

where $\mathbf{f}$ is the approximated physical quantity, $V_{\boldsymbol{r}_K}$ is the volume of the particle located at $\boldsymbol{r}_K$, $\bar{\Omega}$ denotes entire domain including boundary particles, $\tilde{\Omega}$ denotes only internal part of the domain Ω. The particle volumes $V_{\boldsymbol{r}_K}$ are selected to satisfy during numerical simulations only $\sum_{\boldsymbol{r}_K \in \bar{\Omega}} V_{\boldsymbol{r}_K} = V_\Omega$, where V_Ω is the volume of the domain Ω.

The proposed discretization schemes should also provide a good accuracy of the operator (1) with a discontinuous $m\left(\boldsymbol{r}\right)$ (or piecewise continuous function) coefficients since these coefficient cannot be differentiable in the classical sense. The standard SPH spatial discretization of the Laplace operator (1) arises from the following relations with $g\left(\boldsymbol{r}\right) = 0$, $\forall \boldsymbol{r} \in \tilde{\Omega}_{\boldsymbol{r}_I, \tilde{h}_I}$ and $W \in H^1\left(\Omega_{\boldsymbol{r}_I, \tilde{h}_I}\right)$ (i.e., we consider kernel functions from Sobolev space with L_2-norms of the function itself and its gradient):

$$\mathbf{L}\left(\mathbf{u}\left(\boldsymbol{r}_I\right)\right) = \lim_{\tilde{h}_I \to 0} \int_{\Omega_{\boldsymbol{r}_I, \tilde{h}_I}} \mathbf{L}\left(\mathbf{u}\left(\boldsymbol{r}\right)\right) W\left(\boldsymbol{r} - \boldsymbol{r}_I, \tilde{h}_I\right) dV_{\boldsymbol{r}} =$$

$$= \lim_{\tilde{h}_I \to 0} \left[\int_{\Omega_{\boldsymbol{r}_I, \tilde{h}_I}} \mathbf{M}\left(\boldsymbol{r}\right) \nabla \mathbf{u}\left(\boldsymbol{r}\right) \cdot \nabla W\left(\boldsymbol{r} - \boldsymbol{r}_I, \tilde{h}_I\right) dV_{\boldsymbol{r}} \right], \tag{5}$$

where $W\left(\boldsymbol{r} - \boldsymbol{r}_I, \tilde{h}_I\right)$ is the kernel that weakly approximates the Dirac delta function $\delta\left(\boldsymbol{r} - \boldsymbol{r}_I\right)$ but with finite characteristic width $\tilde{h}_I = \tilde{h}(\boldsymbol{r}_I)$ (or physical smoothing length) around the particle I (subscript is omitted if $\tilde{h}$ refers to any particles). The effective characteristic width $\tilde{h}_I$ is defined by (6) using smoothing particle length h_I around the particle I. The control volumes in the meshless discretization are the patches, which are interior to the support of the kernels $W\left(\boldsymbol{r} - \boldsymbol{r}_I, \tilde{h}_I\right)$, i.e. $\Omega_{\boldsymbol{r}_I, \tilde{h}_I} = \text{supp } W\left(\boldsymbol{r} - \boldsymbol{r}_I, \tilde{h}_I\right)$ and $\boldsymbol{r}$, $\boldsymbol{r}_I$ are points in Euclidean space $\mathbb{R}^n$, "supp" indicates the support of the kernels. Additionally, it can be required that the kernels are radially symmetric and compactly supported (supp $W = \{\boldsymbol{r}_J \mid W\left(\boldsymbol{r}_J - \boldsymbol{r}_I, \tilde{h}_I\right) \neq 0\}$) leading to following definitions:

$$\Delta\tilde{x}_I = \sup_{\boldsymbol{r}_J \in \Omega_{\boldsymbol{r}_I, \tilde{h}_I}} \Delta x_{IJ}, \ \Delta\tilde{x}_{I,m} = \inf_{\boldsymbol{r}_J \in \Omega_{\boldsymbol{r}_I, \tilde{h}_I}} \Delta x_{IJ}, \qquad \Delta x_{IJ} = \left\| \boldsymbol{r}_J - \boldsymbol{r}_I \right\|,$$

$$\tilde{h}_I = \sup_{J:\boldsymbol{r}_J \in \Omega_{\boldsymbol{r}_I, \tilde{h}_I}} \tilde{h}_{IJ}, \qquad \tilde{h}_{I,m} = \inf_{J:\boldsymbol{r}_J \in \Omega_{\boldsymbol{r}_I, \tilde{h}_I}} \tilde{h}_{IJ}, \tag{6}$$

where Δx_{IJ} is the distance between particles I and J (we assume that particles do not overlap), $\Delta\tilde{x}_{I,m}$ is the radius of space around particle I which is not filled by particles ($\Delta\tilde{x}_m$ refers to $\Delta\tilde{x}_{I,m}$ at any particle I), $\Delta\tilde{x}_I$ is the maximum distance between particles I and J inside control volume $\Omega_{\boldsymbol{r}_I, \tilde{h}_I}$ ($\Delta\tilde{x}$ refers to $\Delta\tilde{x}_I$ at any particle I), $\tilde{h}_{I,m}$ is the inner smoothing length ($\tilde{h}_{I,m} \le \tilde{h}_I$), $\tilde{h}_{IJ}$ is the effective smoothing length between particles I and J (which will be defined in Section 2.2). However, it is important to note that, in the case of the homogeneous particle distribution, it is common to use $\tilde{h}_I = \tilde{h}_{I,m} = h = f \cdot \Delta x = \text{const}$, where $\Delta\tilde{x}_{I,m} = \Delta x$ is the inter-particles distance, f is the scaling factor. Hence, it is important that pairs of length scales $(\tilde{h}_{I,m}, \Delta\tilde{x}_{I,m})$ for heterogeneous particle distribution and $(h, \Delta x)$ for homogeneous particle distribution are distinguished during the analysis.

In relation (5), if $\nabla\mathbf{u}\left(\boldsymbol{r}\right)$ is smooth and kernels are radially symmetric and compactly supported then $\nabla\mathbf{u}\left(\boldsymbol{r}\right)$ can be expanded in a Taylor series about $\boldsymbol{r}_I$ and it can be shown using integration by parts that the smoothing error due to

relation (5) is of $\mathcal{O}\left(h^2\right)$ (similar to [54]) in the largest disk in $\mathbb{R}^n$ where the Taylor series converges:

$$\mathbf{L}\left(\mathbf{u}\left(\mathbf{r}_I\right)\right) = \int_{\Omega_{\mathbf{r}_I, \tilde{h}_I}} \mathbf{M}\left(\mathbf{r}\right) \nabla \mathbf{u}\left(\mathbf{r}\right) \cdot \nabla W\left(\mathbf{r} - \mathbf{r}_I, \tilde{h}_I\right) dV_{\mathbf{r}} + \mathcal{O}\left(\tilde{h}_I^2\right). \tag{7}$$

From the definition of the $\Omega_{\mathbf{r}_I, \tilde{h}_I}$, it follows that there is an infinite cover of the numerical domain Ω:

$$\Omega = \bigcup_{\mathbf{r}_I \in \Omega} \Omega_{\mathbf{r}_I, \tilde{h}_I}. \tag{8}$$

According to the Heine–Borel theorem, there is a finite subcover (since we consider only compact numerical domain Ω), that is

$$\Omega = \text{span}\left\{\Omega_{\mathbf{r}_I, \tilde{h}_I} / I = 1, \ldots, N\right\}, \tag{9}$$

where N is the number of particles (i.e., patches) in the numerical discretization.

The SPH spatial discretization of the integral (7) is defined over the control volumes $\Omega_{\mathbf{r}_I, \tilde{h}_I}$ to obtain the final discretization of the Laplace operator. The final step in the particle method is to approximate the integral relation on the right-hand side of the (7) using Monte-Carlo expressions or any cubature rules [55,43,33,15] and which is known as the particle approximation step and resulting in the approximate form of the operator $\langle\mathbf{L}\left(\mathbf{u}\left(\mathbf{r}_I\right)\right)\rangle$, where integration is substituted by summation. Hence, using SPH discretization technique and assuming $\mathbf{M}^{\alpha\beta}\left(\mathbf{r}\right) = \delta_{\alpha\beta}$, $\mathbf{u}\left(\mathbf{r}\right) = \mathbf{r}$, the expression (5) can be written for $\forall\mathbf{r}_I \in \Omega_{\mathbf{r}_I, \tilde{h}_I}$ and $\forall\{\mathbf{r}_K, V_{\mathbf{r}_K} : \mathbf{r}_K \in \Omega_{\mathbf{r}_I, \tilde{h}_I}\}$

$$\mathbf{0} \equiv \lim_{\Delta\tilde{x}_I \to 0} \lim_{\tilde{h}_I \to 0} \sum_{\mathbf{r}_K \in \Omega_{\mathbf{r}_I, \tilde{h}_I}} \nabla W\left(\mathbf{r}_K - \mathbf{r}_I, \tilde{h}_I\right) V_{\mathbf{r}_K}, \quad \forall\mathbf{r}_I, \tag{10}$$

$$\mathbf{N}\left(\Delta\tilde{x}_I, \tilde{h}_I\right) = \sum_{\mathbf{r}_K \in \Omega_{\mathbf{r}_I, \tilde{h}_I}} \nabla W\left(\mathbf{r}_K - \mathbf{r}_I, \tilde{h}_I\right) V_{\mathbf{r}_K}, \quad \forall\mathbf{r}_I, \tag{11}$$

where $\mathbf{N}\left(\Delta\tilde{x}_I, \tilde{h}_I\right)$ is the SPH correction vector, which shows the deviation from the zero vector. The strategy of selecting $V_{\mathbf{r}_K}$ plays a crucial role depending on the particle position $\mathbf{r}_K$, kernel $W\left(\mathbf{r}_K - \mathbf{r}_I, \tilde{h}_I\right)$ and the smoothing length $\tilde{h}_I$. In the following section, we formulate the limiting condition for the particle volumes $V_{\mathbf{r}_K}$ $\forall K$ which we call the *SPH continuity condition*.

Remark 1. A sufficient condition for (10) to hold (i.e., double limit and the iterated limits exist and are equal) is Moore–Osgood theorem: If $\lim_{\tilde{h}_I \to 0} \mathbf{N}\left(\Delta\tilde{x}_I, \tilde{h}_I\right)$ exists pointwise for each $\Delta\tilde{x}_I$ different from 0 and if $\lim_{\Delta\tilde{x}_I \to 0} \mathbf{N}\left(\Delta\tilde{x}_I, \tilde{h}_I\right)$ converges uniformly for $\tilde{h}_I \neq 0$ then the double limit and the iterated limits exist and are equal.

The assumption that the boundary term from the integration by parts is zero in (5) is valid only in regions where the kernel has a full support, or the function, or the gradient of the function itself is zero. For particles near free surfaces or boundary, the neglect of these terms leads to significant errors for boundary value problems. Several techniques have been developed to address these errors through various correction methods, e.g., by calculating the boundary integrals [15]. In addition, this can be corrected as it will be shown below by applying normalized corrected meshless methods in the derivative approximations. In the following section, the commonly used SPH kernels and its gradients are considered.

2.1. SPH kernel and its gradient

A central point of the SPH formalism is the concept of the interpolating function (or kernel) through which the continuum properties of the medium are recovered from a discrete sample of N points (8) with prescribed mass (for conventional Lagrangian methods) or volume V_I (for fully Eulerian methods). In the Lagrangian formulation, these points move according to the specified governing laws, whereas these points are fixed in space for the Eulerian formulation. A good interpolating kernel must satisfy a few basic requirements: it must weakly tend to the delta function in the continuum limit and has to be a continuous function with piecewise first derivatives at least.

From a more practical point of view it is also advisable to deal with symmetric finite range kernels, the latter to avoid $\mathcal{O}\left(N^2\right)$ calculations. In addition, instead of using theoretical finite characteristic smoothing length $\tilde{h}_I$ in the definition of the kernel, the effective smoothing length $\tilde{h}_{IJ}$ between particles I and J is used directly in the definition of the kernel expression in practical calculations. Cubic and quintic splines are the commonly used kernels in SPH formulations [56,15]. Since the quintic spline does not provide the numerical advantages, the cubic spline is used in this paper:

Definition 1. The kernel function centered at particle $\boldsymbol{r}_I$ is defined as

$$W\left(z_J, \tilde{h}_{IJ}\right) = \frac{\varXi}{\tilde{h}_{IJ}^n}\hat{W} = \frac{\varXi}{\tilde{h}_{IJ}^n}\begin{cases} 1 - \frac{3}{2}z_J^2 + \frac{3}{4}z_J^3, & 0 \leqslant z_J \leqslant 1; \\ \frac{1}{4}(2 - z_J)^3, & 1 < z_J \leqslant 2; \\ 0, & z_J > 2; \end{cases} \tag{12}$$

where $z_J = \left\|\boldsymbol{r}_J - \boldsymbol{r}_I\right\|_2 / \tilde{h}_{IJ}$ is the dimensionless variable, $\hat{W}$ is the kernel in a dimensionless form, and $\varXi$ is the normalization factor equal to 3/2, $10/(7\pi)$, and $1/\pi$ in 1D, 2D, and 3D, respectively. In continuous case, the particle index is omitted as z for dimensionless variable.

The different choices of computing effective smoothing length between particles used in this paper will be discussed in the upcoming subsection. Although, the kernel is normalized in a continuous sense, it is important to note that $W\left(\boldsymbol{r}_J - \boldsymbol{r}_I, \tilde{h}_{IJ}\right)$ does not satisfy the normalization condition in the discrete space

$$\sum_{\boldsymbol{r}_J \in \Omega_{\boldsymbol{r}_I, \tilde{h}_I}} W\left(\boldsymbol{r}_J - \boldsymbol{r}_I, \tilde{h}_{IJ}\right) V_{\boldsymbol{r}_J} \neq 1$$

due to the particle distribution and incomplete kernel support near the boundary and, hence, the discretized-normalized kernel function can be considered:

$$\overline{W}\left(\boldsymbol{r}_J - \boldsymbol{r}_I, \tilde{h}_{IJ}\right) = \frac{W\left(\boldsymbol{r}_J - \boldsymbol{r}_I, \tilde{h}_{IJ}\right)}{\sum_{\boldsymbol{r}_J \in \Omega_{\boldsymbol{r}_I, \tilde{h}_I}} W\left(\boldsymbol{r}_J - \boldsymbol{r}_I, \tilde{h}_{IJ}\right) V_{\boldsymbol{r}_J}} = \frac{W\left(\boldsymbol{r}_J - \boldsymbol{r}_I, \tilde{h}_{IJ}\right)}{\nu\left(\boldsymbol{r}_I\right)}, \tag{13}$$

where $\nu\left(\boldsymbol{r}_I\right)$ is the specific concentration of particle $\boldsymbol{r}_I$ (i.e., it is approximately the inverse of the compact volume support multiplied by the particle I volume and $\nu\left(\boldsymbol{r}_I\right) \sim \mathcal{O}\left(1\right)$) which has a larger value in a dense particle region than in a dilute particle region. In regions of the high particle density, the denominator in (13) is high resulting in lower values of the kernel $\overline{W}\left(\boldsymbol{r}_I - \boldsymbol{r}_J, \tilde{h}_{IJ}\right)$. Thus, the denominator normalizes the kernel function to ensure that the kernel $\overline{W}\left(\boldsymbol{r}_J - \boldsymbol{r}_I, \tilde{h}_{IJ}\right)$ forms a local partitioning of unity

$$\sum_{\boldsymbol{r}_J \in \Omega_{\boldsymbol{r}_I, \tilde{h}_I}} \overline{W}\left(\boldsymbol{r}_J - \boldsymbol{r}_I, \tilde{h}_{IJ}\right) V_{\boldsymbol{r}_J} = 1 \tag{14}$$

regardless of the particle distribution within the $\Omega_{\boldsymbol{r}_I, \tilde{h}_I} = \text{supp}\, W\left(\boldsymbol{r}_J - \boldsymbol{r}_I, \tilde{h}_I\right)$. The discretized-normalized kernel function $\overline{W}\left(\boldsymbol{r}_J - \boldsymbol{r}_I, \tilde{h}_I\right)$ will also be used in the discretization schemes below. At this point, all possible options of computing $\overline{\nabla W}(\boldsymbol{r}_J - \boldsymbol{r}_I, \tilde{h}_{IJ})$ are listed:

Definition 2.

$$\overline{\nabla W}\left(\boldsymbol{r}_J - \boldsymbol{r}_I, \tilde{h}_{IJ}\right) := \nabla_{\boldsymbol{r}_I} W\left(\boldsymbol{r}_J - \boldsymbol{r}_I, \tilde{h}_{IJ}\right) = -\nabla_{\boldsymbol{r}_J} W\left(\boldsymbol{r}_J - \boldsymbol{r}_I, \tilde{h}_{IJ}\right), \tag{15}$$

Definition 3.

$$\overline{\nabla W}\left(\boldsymbol{r}_J - \boldsymbol{r}_I, \tilde{h}_{IJ}\right) := \nabla_{\boldsymbol{r}_I} \overline{W}\left(\boldsymbol{r}_J - \boldsymbol{r}_I, \tilde{h}_{IJ}\right) =$$

$$= \left[\frac{\nabla_{\boldsymbol{r}_I} W\left(\boldsymbol{r}_J - \boldsymbol{r}_I, \tilde{h}_{IJ}\right)}{\nu(\boldsymbol{r}_I)} - \frac{W\left(\boldsymbol{r}_J - \boldsymbol{r}_I, \tilde{h}_{IJ}\right) \nabla_{\boldsymbol{r}_I} \nu(\boldsymbol{r}_I)}{\nu^2(\boldsymbol{r}_I)}\right], \tag{16}$$

$$\nabla_{\boldsymbol{r}_I} \nu(\boldsymbol{r}_I) = \sum_{\boldsymbol{r}_K \in \Omega_{\boldsymbol{r}_I, \tilde{h}_I}} \nabla_{\boldsymbol{r}_I} W\left(\boldsymbol{r}_K - \boldsymbol{r}_I, \tilde{h}_{IK}\right) V_{\boldsymbol{r}_K},$$

where $\nu(\boldsymbol{r}_I)$ is the specific volume of the particle located at the point $\boldsymbol{r}_I$.

Additionally, two options can be written as

Definition 4.

$$\overline{\nabla W}(\boldsymbol{r}_J - \boldsymbol{r}_I, \tilde{h}_{IJ}) := \widetilde{\nabla}_{\boldsymbol{r}_I} \overline{W}\left(\boldsymbol{r}_J - \boldsymbol{r}_I, \tilde{h}_{IJ}\right) = -\frac{\nabla_{\boldsymbol{r}_J} W(\boldsymbol{r}_J - \boldsymbol{r}_I, \tilde{h}_{IJ})}{\nu(\boldsymbol{r}_I)}, \tag{17}$$

where $\nu(\boldsymbol{r}_I)$ is assumed to be a constant during the differentiation with respect to $\boldsymbol{r}_J$.

The alternative case is when we assume that $\nu(\boldsymbol{r}_I)$ can be considered as a function of the location of other particles $\boldsymbol{r}_K \in \Omega_{\boldsymbol{r}_I, \tilde{h}_I}$

$$\nu(\boldsymbol{r}_I, \boldsymbol{r}_K) = \sum_{\boldsymbol{r}_J \in \Omega_{\boldsymbol{r}_I, \tilde{h}_I}} W(\boldsymbol{r}_J - \boldsymbol{r}_I, \tilde{h}_{IJ}) V_{\boldsymbol{r}_J},$$

leading to the following relations

Definition 5.

$$\overline{\nabla W}(\boldsymbol{r}_J - \boldsymbol{r}_I, \tilde{h}_{IJ}) := \overline{\nabla}_{\boldsymbol{r}_I} \overline{W}(\boldsymbol{r}_J - \boldsymbol{r}_I, \tilde{h}_{IJ}) = -\overline{\nabla}_{\boldsymbol{r}_J} \overline{W}(\boldsymbol{r}_J - \boldsymbol{r}_I, \tilde{h}_{IJ})$$

$$= -\left[\frac{\nabla_{\boldsymbol{r}_J} W(\boldsymbol{r}_J - \boldsymbol{r}_I, \tilde{h}_{IJ})}{\nu(\boldsymbol{r}_I, \boldsymbol{r}_J)} - \frac{W(\boldsymbol{r}_J - \boldsymbol{r}_I, \tilde{h}_{IJ}) \nabla_{\boldsymbol{r}_J} \nu(\boldsymbol{r}_I, \boldsymbol{r}_J)}{\nu^2(\boldsymbol{r}_I, \boldsymbol{r}_J)} \right] \qquad . \tag{18}$$

$$\nabla_{\boldsymbol{r}_J} \nu(\boldsymbol{r}_I, \boldsymbol{r}_J) = \nabla_{\boldsymbol{r}_J} W(\boldsymbol{r}_J - \boldsymbol{r}_I, \tilde{h}_{IJ}) V_{\boldsymbol{r}_J}$$

Where $\overline{\nabla W}(\boldsymbol{r}_J - \boldsymbol{r}_I, \tilde{h}_{IJ})$ and $\nabla_{\boldsymbol{r}_I}$ in all definitions above represent the nabla operator with respect to $\boldsymbol{r}_I$. Assuming this for the rest of the paper, the $\boldsymbol{r}_I$ index is omitted for the remainder of this manuscript.

Remark 2. In general, we assume in this paper some variations of the smoothing length $\tilde{h}(\boldsymbol{r})$ and, hence, definitions of the kernel gradient should include $\nabla \tilde{h}$. However, we consider the numerical examples where $\|\nabla \tilde{h}\| \ll 1$ and terms with $\nabla \tilde{h}$ are omitted.

Similar to the Moving Least Squares (MLS) method [57], Eqs. (16) and (18) are two different forms of "full derivatives". At the same time, Eqs. (15) and (17) are two different forms of "diffuse derivatives". From these options, it follows that "full derivatives" are connected with the differentiation of a discrete function and "diffuse derivatives" are connected with the differentiation of an exact function. Two types of derivatives are different in treating the normalization factor $\nu(\boldsymbol{r}_I)$ where "full derivatives" assume $\nu(\boldsymbol{r}_I)$ as function and "diffuse derivatives" assume $\nu(\boldsymbol{r}_I)$ as constant. Both types of derivatives have some advantages and disadvantages and the choice depends on the application. The impact of different options on numerical results will be shown below.

Finally, it is important to note the following relation for the kernel gradients (15), (17), and (18):

$$\overline{\nabla_\alpha W}\left(\boldsymbol{r}_J - \boldsymbol{r}_I, \tilde{h}_{IJ}\right) = -\frac{1}{\tilde{h}_{IJ}} G(z_J, \boldsymbol{r}_I) \frac{\left[\boldsymbol{r}_J^\alpha - \boldsymbol{r}_I^\alpha\right]}{\|\boldsymbol{r}_J - \boldsymbol{r}_I\|}, \tag{19}$$

where function $G(z_J, \boldsymbol{r}_I) \leq 0$ has a different shape depending on the definitions (15), (17) and (18). Using SPH discretization technique and assuming $\mathbf{M}^{\alpha\beta}(\boldsymbol{r}) = \delta_{\alpha\beta}$, $\mathbf{u}(\boldsymbol{r}) = \|\boldsymbol{r} - \boldsymbol{r}_I\|^2$, $\boldsymbol{r} \in \mathbb{R}^n$, the expression (5) can be written as

$$\lim_{\Delta \tilde{x}_I \to 0} \lim_{\tilde{h}_I \to 0} \sum_{\boldsymbol{r}_J \in \Omega_{\boldsymbol{r}_I, \tilde{h}_I}} \left[\boldsymbol{r}_J - \boldsymbol{r}_I\right] \cdot \nabla W\left(\boldsymbol{r}_J - \boldsymbol{r}_I, \tilde{h}_I\right) V_{\boldsymbol{r}_K} =$$

$$= \lim_{\Delta \tilde{x}_I \to 0} \lim_{\tilde{h}_I \to 0} \sum_{\boldsymbol{r}_J \in \Omega_{\boldsymbol{r}_I, \tilde{h}_I}} V_{\boldsymbol{r}_K} z_J \left|G(z_J, \boldsymbol{r}_I)\right| = n, \quad \forall \boldsymbol{r}_I \tag{20}$$

The sum (20) contains only positive numbers, hence, the necessary condition to fulfill this relation (20) is to satisfy the *SPH continuity condition* for selecting particle volumes given their positions and the smoothing length:

$$V_{\boldsymbol{r}_J} \leq n \cdot \frac{1}{z_J \left|G(z_J, \boldsymbol{r}_I)\right|} \quad \forall \boldsymbol{r}_I \qquad \text{or} \qquad V_{\boldsymbol{r}_J} \leq n \cdot \min_{I \neq J: \boldsymbol{r}_J \in \Omega_{\boldsymbol{r}_I, \tilde{h}_I}} \left(\frac{1}{z_J \left|G(z_J, \boldsymbol{r}_I)\right|}\right) \tag{21}$$

The condition (21) provides an upper bound for the particle volumes $V_{\boldsymbol{r}_J}$ given the dimension of the space n, particle locations $\boldsymbol{r}_J$, kernel $W\left(\boldsymbol{r}_J - \boldsymbol{r}_I, \tilde{h}_I\right)$ and smoothing length $\tilde{h}_I$. It is important at this point to introduce the following

quantity which will be used in the error analysis of the proposed SPH schemes:

$$
\begin{aligned}
&(a)\ \ C\left(\tilde{h}_{I,m}, \Delta\tilde{x}_I\right) = \sum_{\mathbf{r}_J \in \Omega_{\mathbf{r}_I,h}} V_{\mathbf{r}_J}\left|G(z_J, \mathbf{r}_I)\right|, \\
&(b)\ \ \left\|\mathbf{N}\left(\Delta\tilde{x}_I, \tilde{h}_I\right)\right\| \le \frac{C\left(\tilde{h}_{I,m}, \Delta\tilde{x}_I\right)}{\tilde{h}_{I,m}}.
\end{aligned}
\tag{22}
$$

The condition (22)(b) is consistent with the Lemma 4 presented in [58] during the analysis of particle method for first-order symmetric systems. Furthermore, $\lim\limits_{\tilde{h}_{I,m}\to 0} \dfrac{C\left(\tilde{h}_{I,m}, \Delta\tilde{x}_I\right)}{\tilde{h}_{I,m}}$ subject to (21) exists pointwise for each $\Delta\tilde{x}_I \ne 0$. However, if $\Delta\tilde{x}_I$ is not fixed, the above limit has different values when $\tilde{h}_{I,m}$ goes to zero according to the specific choice of the ratio $\Delta\tilde{x}_I/\tilde{h}_{I,m}$ and number of particles in the kernel support. This leads to totally different results, i.e. some summations may diverge or converge according to the choice above. Although, $\lim\limits_{\tilde{h}_I\to 0} \mathbf{N}\left(\Delta\tilde{x}_I, \tilde{h}_I\right)$ exists pointwise for each $\Delta\tilde{x}_I \ne 0$, $\lim\limits_{\Delta\tilde{x}_I\to 0} \mathbf{N}\left(\Delta\tilde{x}_I, \tilde{h}_I\right)$ may not converge uniformly for $\tilde{h}_I \ne 0$ for some set of particle volumes $\{V_{\mathbf{r}_J}\}$. Hence, the relation between $\Delta\tilde{x}_I$ and $\tilde{h}_I$ (or $\tilde{h}_{I,m}$), kernel W and set of particle volumes $\{V_{\mathbf{r}_J}\}$ defines the convergence conditions of (10) and (20).

The SPH method shows good approximation properties in regions where the kernel has full support. For particles near stress-free surfaces or boundary, the SPH method shows a poor approximation. Several techniques have been developed to address these errors through various correction methods, e.g., by applying normalized-corrected meshless methods in the derivative approximations [33,15,39,40], which requires normalized-corrected definitions of the kernel gradient as follows:

$$
\overline{\nabla_\alpha^* W}\left(\mathbf{r}_J - \mathbf{r}_I, \tilde{h}_{IJ}\right) = \mathbf{C}_{\alpha\beta}\overline{\nabla_\beta W}\left(\mathbf{r}_J - \mathbf{r}_I, \tilde{h}_{IJ}\right),
\tag{23}
$$

where $\overline{\nabla_\alpha^* W}$ is also defined with respect to $\mathbf{r}_I$ and the elements $\mathbf{C}_{\alpha\beta}$ are defined by the matrix $\mathbf{C}\left(\mathbf{r}_I\right)$:

$$
\mathbf{C}\left(\mathbf{r}_I\right) = \left[\sum_{\mathbf{r}_J \in \Omega_{\mathbf{r}_I,\tilde{h}_I}} V_{\mathbf{r}_J}\left[\mathbf{r}_J - \mathbf{r}_I\right] \otimes \overline{\nabla W}\left(\mathbf{r}_J - \mathbf{r}_I, \tilde{h}_{IJ}\right)\right]^{-1},
\tag{24}
$$

$$
\sum_{\mathbf{r}_J \in \Omega_{\mathbf{r}_I,h}} V_{\mathbf{r}_J}\left[\mathbf{r}_J^\gamma - \mathbf{r}_I^\gamma\right] \overline{\nabla_\alpha^* W}\left(\mathbf{r}_J - \mathbf{r}_I, \tilde{h}_{IJ}\right) = \delta_{\gamma\alpha}, \quad \forall\gamma, \alpha;
\tag{25}
$$

where the summation by repeating Greek indices is only assumed throughout this paper, $\overline{\nabla_\alpha^* W}$ is the normalized-corrected gradient of the kernel, and $\mathbf{C}_{\alpha\beta}$ is the correction symmetric tensor [59]. It was shown [60,61] that the value of the minimum eigenvalue $\lambda^\mathbf{C}\left(\mathbf{r}_I\right)$ of the matrix $\mathbf{C}^{-1}$ based on the discretized-normalized kernel function depends on the particle distribution within the domain $\Omega_{\mathbf{r}_I,\tilde{h}_I} = \mathrm{supp}W\left(\mathbf{r}_I - \mathbf{r}, \tilde{h}_I\right)$. When going away from the $\Omega_{\mathbf{r}_I,\tilde{h}_I}$ domain this eigenvalue tends theoretically to zero, while inside this domain the eigenvalue tends theoretically to one. This important information allows determining regions of the continuum media where free-surfaces are located [60,61].

In this paper, the discretizations of the Laplace operator are based on the gradient of the kernel. Several methods of Laplace discretizations were proposed [62–65] using second derivatives of the variable $\mathbf{u}$. However, second-order derivatives can often be avoided entirely if the PDE is written in a weak form (5). It is important to note that approximations using second-order derivatives of the kernel are often noisy and sensitive to the particle distribution, particularly for spline kernels of lower orders.

2.2. SPH symmetrization of smoothing length

The true particle smoothing length h_I may vary both in space and time in general. Therefore, in general case, each particle has its own smoothing length h_I. Considering the case where $h_I \ne h_J$ for two different interacting particles I and J and the kernel support based on $\tilde{h}_I$ and located in I which covers the particle J but the kernel support located in J does not cover the particle I. In this case, the particle I acting on particle J (produces, e.g., a flux or a force) without particle J acting on the particle I, which leads to a violation of fundamental laws (e.g., mass conservation or Newton's third law) for a closed system of particles. This problem has been resolved by introducing the symmetrization of the smoothing length. In this study, the following symmetrization option is used:

$$
\tilde{h}_{IJ} = \frac{h_I + h_J}{2}.
\tag{26}
$$

It is clear that $h = \tilde{h}_I = \tilde{h}_{I,m}$, $h = \tilde{h}_{IJ}$ $\forall I, J$ and $\Delta\tilde{x}_{I,m} = \Delta x$ $\forall I$ for homogeneous particle distribution.

This completes the description of basic properties of SPH method allowing to construct all necessary building elements of SPH discretization such as list of neighbors, kernel values, and kernel gradients. The following sections describe the traditional and newly proposed discretization schemes for the Laplace operator. Without loss of generality, the discretization schemes below are build for $-\langle \mathbf{L}(\mathbf{u}(\mathbf{r}_I)) \rangle$. Hence, there are two sources of the discretization error: (a) the error (smoothing error) associated with the weak approximation of the Dirac delta function $\delta(\mathbf{r} - \mathbf{r}_I)$, which is related to the smoothing particle length $\tilde{h}_I$ and (b) the error (discretization error) associated with Monte-Carlo expressions or any cubature rules controlled by $\Delta\tilde{x}_I$, which is related to the number of particles and particle distribution within the control volume $\Omega_{\mathbf{r}_I, \tilde{h}_I}$.

2.3. Brookshaw's scheme (1985)

Brookshaw proposed [53] an approximation of the Laplacian for an inhomogeneous scalar field $m(\mathbf{r})$, i.e., $\mathbf{M}^{\alpha\beta}(\mathbf{r}) = m(\mathbf{r})\delta_{\alpha\beta}$, $\alpha, \beta = 1, \ldots, n$; that only includes first order derivatives:

$$\langle \nabla(m(\mathbf{r}_I) \nabla\mathbf{u}(\mathbf{r}_I)) \rangle =$$

$$\sum_{\mathbf{r}_J \in \Omega_{\mathbf{r}_I, \tilde{h}_I}} V_{\mathbf{r}_J} \left[\mathbf{u}(\mathbf{r}_J) - \mathbf{u}(\mathbf{r}_I) \right] \frac{(\mathbf{r}_J - \mathbf{r}_I) \cdot (m_J + m_I) \overline{\nabla W}\left(\mathbf{r}_J - \mathbf{r}_I, \tilde{h}_{IJ}\right)}{\left\| \mathbf{r}_J - \mathbf{r}_I \right\|^2}, \tag{27}$$

where $V_{\mathbf{r}_J}$ is the volume of the particle J, $\|\bullet\|$ is the Euclidean norm throughout this paper, $\mathbf{u}(\mathbf{r})$ is the unknown scalar or vector field (e.g., pressure p or velocity v) $\forall \mathbf{r} \in \Omega \subset \mathbb{R}^n$, $m_I = m(\mathbf{r}_I)$, $\mathbf{r}_I \in \Omega \subset \mathbb{R}^n$ and $m_J = m(\mathbf{r}_J)$, $\mathbf{r}_J \in \Omega \subset \mathbb{R}^n$ are the field coefficients.

This scheme can be derived by applying the particle approximation step to the right-hand side of (5) with the following assumptions

$$\nabla\mathbf{u}(\mathbf{r}_J) \approx \left[\mathbf{u}(\mathbf{r}_J) - \mathbf{u}(\mathbf{r}_I) \right] \frac{(\mathbf{r}_J - \mathbf{r}_I)}{\left\| \mathbf{r}_J - \mathbf{r}_I \right\|^2}. \tag{28}$$

Some special words need to be said about the mobility approximation, which comes in the form

$$2m(\mathbf{r}_J) \approx m_J + m_I. \tag{29}$$

The factor 2 is introduced to compensate the factor of 1/2 in the second leading term of the Taylor expansion of the relation (28). Furthermore, the relation (29) allows to capture a heterogeneous mobility field distribution.

The theoretical error analysis presented below in this paper requires smoothness properties of the considered functions, e.g., $\mathbf{u}(\mathbf{r})$, W and $m(\mathbf{r})$. The cubic kernel W (12) and $m(\mathbf{r})$ have limited smoothness properties and impact of this will be covered below.

Theorem 1. *The discretization scheme* (27) *at a given point* $\mathbf{r}_I \in \Omega \subset \mathbb{R}^n$ *sufficiently far away from the boundary* $\partial\Omega$ *(i.e., where the kernel W has a full support and particle volumes satisfy the SPH continuity condition* (21)*) has an error (discretization error) bounded by* $C\left(\tilde{h}_{I,m}, \Delta\tilde{x}_I\right) \cdot \left(\frac{\Delta\tilde{x}_I^\omega}{\tilde{h}_{I,m}}\right)$, $0 \leq \omega < 2$ *for any scalar mobility field* $m(\mathbf{r}) \in C^1(\Omega) \cap H^2(\Omega)$, $m(\mathbf{r}) \geq 0$, *where* $\Delta\tilde{x}_I = \sup_{J : \mathbf{r}_J \in \Omega} \left\| \mathbf{r}_J - \mathbf{r}_I \right\|$, $\tilde{h}_{I,m} = \inf_{J : \mathbf{r}_J \in \Omega_{\mathbf{r}_I, \tilde{h}_I}} \tilde{h}_{IJ}$.

Proof. Note that the *SPH continuity condition* (21) is the necessary condition to fulfill the relation (20) and limits the values of $V_{\mathbf{r}_J}$ $\forall J$. Using Taylor series expansions about a point $\mathbf{r}_I$, the following relations can be written:

$$\mathbf{u}(\mathbf{r}_J) = \mathbf{u}(\mathbf{r}_I) + \mathbf{u}_{,\alpha}(\mathbf{r}_I)\left[r_J^\alpha - r_I^\alpha\right] + \frac{1}{2}\mathbf{u}_{,\alpha\gamma}(\mathbf{r}_I)\left[r_J^\alpha - r_I^\alpha\right]\left[r_J^\gamma - r_I^\gamma\right] + \mathcal{O}\left(\left\| \mathbf{r}_J - \mathbf{r}_I \right\|^3\right). \tag{30}$$

Since scalar mobility field $m(\mathbf{r}) \in C^1(\Omega) \cap H^2(\Omega)$, the following relation can be written:

$$m(\mathbf{r}_J) = m(\mathbf{r}_I) + m_{,\alpha}(\mathbf{r}_I)\left[r_J^\alpha - r_I^\alpha\right] + \mathcal{O}\left(\left\| \mathbf{r}_J - \mathbf{r}_I \right\|^2\right). \tag{31}$$

Substituting relations (30)–(31) into the scheme (27), it leads to the following relations:

$$\sum_{\mathbf{r}_J \in \Omega_{\mathbf{r}_I, \tilde{h}_I}} V_{\mathbf{r}_J} \left[\mathbf{u}(\mathbf{r}_J) - \mathbf{u}(\mathbf{r}_I) \right] \frac{(\mathbf{r}_J - \mathbf{r}_I) \cdot (m_J + m_I) \cdot \overline{\nabla W}\left(\mathbf{r}_J - \mathbf{r}_I, \tilde{h}_{IJ}\right)}{\left\| \mathbf{r}_J - \mathbf{r}_I \right\|^2} = \tag{32}$$

$$= 2m(\mathbf{r}_I)\mathbf{u}_{,\alpha}(\mathbf{r}_I)\mathbf{N}_\alpha + m(\mathbf{r}_I)\mathbf{u}_{,\alpha\gamma}(\mathbf{r}_I)\Gamma_{\alpha\gamma} + m_{,\alpha}(\mathbf{r}_I)\mathbf{u}_{,\gamma}(\mathbf{r}_I)\Gamma_{\alpha\gamma} + \mathcal{E},$$

where $\mathbf{N}_\alpha\left(\mathbf{r}_I\right) = \sum_{\mathbf{r}_J \in \Omega_{\mathbf{r}_I, \tilde{h}_{IJ}}} V_{\mathbf{r}_J} \overline{\nabla_\alpha W}\left(\mathbf{r}_J - \mathbf{r}_I, \tilde{h}_{IJ}\right)$ is defined in terms of general form of the kernel gradient $\overline{\nabla_\alpha W}\left(\mathbf{r}_J - \mathbf{r}_I, \tilde{h}_{IJ}\right)$ (this is a generalization of the definition (11)) and tensor $\boldsymbol{\Gamma}_{\alpha\gamma}$ is defined by

$$\boldsymbol{\Gamma}_{\alpha\gamma}\left(\mathbf{r}_I\right) = \left(\sum_{\mathbf{r}_J \in \Omega_{\mathbf{r}_I, h}} V_{\mathbf{r}_J}\left[r_J^\alpha - r_I^\alpha\right] \overline{\nabla_\gamma W}\left(\mathbf{r}_J - \mathbf{r}_I, \tilde{h}_{IJ}\right)\right). \tag{33}$$

Here, symbols α, γ, ω represent indices such that $\alpha, \beta, \gamma = 1, \ldots, n$. While obtaining (32), the following relation has been used (which is not valid for kernel gradient (16) subject to the random particle distribution):

$$\left[r_J^\alpha - r_I^\alpha\right] \frac{\left(r_J^\gamma - r_I^\gamma\right) \overline{\nabla_\gamma W}\left(\mathbf{r}_J - \mathbf{r}_I, \tilde{h}_{IJ}\right)}{\left\|\mathbf{r}_J - \mathbf{r}_I\right\|^2} = \overline{\nabla_\alpha W}\left(\mathbf{r}_J - \mathbf{r}_I, \tilde{h}_{IJ}\right), \quad \forall \alpha. \tag{34}$$

The leading term of the error function $\mathcal{E}$ in (32) is defined by the following expression

$$\mathcal{E} = \frac{1}{6} m\left(\mathbf{r}_I\right) \mathbf{u}_{,\alpha\beta\gamma}\left(\mathbf{r}_I\right) \mathbf{U}_{\alpha\beta\gamma} + \frac{1}{2} \mathbf{u}_{,\alpha\gamma}\left(\mathbf{r}_I\right) m_{,\beta}\left(\mathbf{r}_I\right) \mathbf{U}_{\alpha\beta\gamma}, \tag{35}$$

where $\mathbf{U}_{\alpha\beta\gamma}\left(\mathbf{r}_I\right)$ is defined by

$$\mathbf{U}_{\alpha\beta\gamma}\left(\mathbf{r}_I\right) = \sum_{\mathbf{r}_J \in \Omega_{\mathbf{r}_I, h}} V_{\mathbf{r}_J}\left[r_J^\alpha - r_I^\alpha\right]\left[r_J^\beta - r_I^\beta\right] \overline{\nabla_\gamma W}\left(\mathbf{r}_J - \mathbf{r}_I, \tilde{h}_{IJ}\right). \tag{36}$$

Typically, 1D (one dimension) error analysis allows to gain a deep insight into the nature of discretization error due to the smoothing integral in (5) and a discrete version of a given scheme (e.g., widely used scheme (27)) and kernel gradient ∇W. To compute exact error in 1D SPH approximation of the following coefficients $\mathbf{N}_\alpha$, $\boldsymbol{\Gamma}_{\alpha\gamma}$, and $\mathbf{U}_{\alpha\beta\gamma}$ (indices will be omitted) at a particle I in terms of the kernel function and its derivatives at $\mathbf{r}_I$, the smoothing length, the particle distributions, the below expression derived in [54] is used for numerical domain of length $2h$.

$$-\sum_J F_J W'_J \Delta x - F'_I = \frac{h^2}{2} F'''_I \int z^2 \hat{W} dz + \mathcal{O}\left(h^4\right) -$$
$$\left(\frac{\Delta x}{h}\right)^{p+2} \frac{B_{p+2}}{(p+2)!}\left(1 - 2^{-p-1}\right) \times \left\{F'_I\left[4\hat{W}_{z=2}^{(p+2)} + 2(p+1)\hat{W}_{z=2}^{(p+1)} + \right.\right. \tag{37}$$
$$\left.\left. + \mathcal{O}\left(h^2\right)\right] + \mathcal{O}\left(\left[\frac{\Delta x}{h}\right]^{p+4}\right)\right\}$$

where Δx, h are the particles volume and smoothing length $\forall J$, F is the approximated data function with its first F' and third F''' derivatives in 1D, W' is the kernel derivative in 1D, B_{p+2} are the Bernoulli numbers, p is the highest integer such that the pth derivative and all lower derivatives are zero at the edges of the compact support of the kernel W (cubic spline (12) has $p = 2$), $\hat{W}_{z=a}^{(m)}$ is the mth derivatives of dimensionless kernel $\hat{W}$ at the point $z = a$. The conditions for expression (37) to be valid [54]: (a) uniformly spaced particle distribution in 1D, (b) smooth data functions F with its derivatives, and (c) kernel functions which are smooth (except at the support boundary), even and normalized. In addition, it is required that the particle volumes span the compact support without gaps or overlaps.

The following functions are substituted into (37): (1) $F(x) = 1$ for $\mathbf{N}(x_I)$, (2) $F(x) = (x - x_I)$ for $\boldsymbol{\Gamma}(x_I)$, (3) $F(x) = (x - x_I)^2$ for $\mathbf{U}(x_I)$. This leads to the following expressions:

$$|\mathbf{N}(x_I)| \sim \mathcal{O}\left(h^4\right) + \left(\frac{\Delta x}{h}\right)^{p+2} \frac{B_{p+2}}{(p+2)!}\left(1 - 2^{-p-1}\right) \times \mathcal{O}\left(\left[\frac{\Delta x}{h}\right]^{p+4}\right) \tag{38}$$

$$|\boldsymbol{\Gamma}(x_I) - 1| \sim \mathcal{O}\left(h^4\right) +$$
$$\left(\frac{\Delta x}{h}\right)^{p+2} \frac{B_{p+2}}{(p+2)!}\left(1 - 2^{-p-1}\right) \times \left\{\left[4\hat{W}_{z=2}^{(p+2)} + 2(p+1)\hat{W}_{z=2}^{(p+1)}\right.\right. \tag{39}$$
$$\left.\left. + \mathcal{O}(h^2)\right] + \mathcal{O}\left(\left[\frac{\Delta x}{h}\right]^{p+4}\right)\right\}$$

$$|\mathbf{U}(x_I)| \sim \mathcal{O}\left(h^4\right) + \left(\frac{\Delta x}{h}\right)^{p+2} \frac{B_{p+2}}{(p+2)!}\left(1 - 2^{-p-1}\right) \times \mathcal{O}\left(\left[\frac{\Delta x}{h}\right]^{p+4}\right) \tag{40}$$

From expressions (38), (39), (40), and (7), it follows that the error of discretization only in 1D is the sum of $\mathcal{O}\left(h^2\right)$ (smoothing error) and $\left[\mathcal{O}\left(\left[\frac{\Delta x}{h}\right]^{p+2}\right) + \mathcal{O}\left(h^4\right)\right]$ (error due to discretization scheme). Hence, as $\left(\frac{\Delta x}{h}\right)$ goes to zero,

the accuracy is controlled by smoothing error $\mathcal{O}\left(h^2\right)$. At the same time, as smoothing error h goes to zero, the accuracy is controlled by $\mathcal{O}\left(\left[\frac{\Delta x}{h}\right]^{p+2}\right)$ and parameter p defines the behavior of the error in 1D subject to the limitations of expression (37).

To examine the effects of non-uniform particle distribution, it is assumed that the numerical domain of length $2h$ is partitioned into a series of subintervals, where each of which represents the volume of a particle as was done in [54]. Each of these volumes has a value Δx_I and is centered at a location $\bar{x}_I$ which does not necessarily coincide with the particle location, x_I. These assumptions were also made in [54] to derive the following relation in 1D:

$$
\begin{aligned}
& -\sum_J F_J W_J' \Delta x_J - F_I' = \frac{h^2}{2} F_I''' \int z^2 \hat{W} dz + \mathcal{O}\left(h^4\right) + \\
& \frac{F_I}{h} \sum_J \left[\hat{W}'' z_J^2 \delta_J + \frac{1}{2} \hat{W}''' z_J^3 \left[\delta_J^2 + \delta_J + 1/12\right] \right] + \\
& F_I' \sum_J \left[\left(\hat{W}_J' + \hat{W}_J'' z_J\right) z_J^2 \delta_J + \left(\hat{W}'' + \frac{1}{2}\hat{W}''' z_J\right) z_J^3 \left[\delta_J^2 + \delta_J + 1/12\right] \right] + \\
& h F_I'' \sum_J \left[\left(\hat{W}_J' + \frac{1}{2}\hat{W}_J'' z_J\right) z_J^3 \delta_J + \frac{1}{2} \left(\hat{W}' + 2\hat{W}'' z_J + \frac{1}{2} z_J^2 \hat{W}'''\right) z_J^3 \left[\delta_J^2 + \delta_J + 1/12\right] \right] + \cdots
\end{aligned}
\tag{41}
$$

where $\delta_J = (\bar{x}_J - x_J)/\Delta x_J$. Dimensionless variables δ_J, Δz_J can be replaced by average values $\bar{\delta}$ and $\Delta \bar{z}$ and moved outside the summations (introducing a higher order error into the analysis itself) [54]. As a result, we can obtain the following asymptotic for $\mathbf{N}(x_I)$, $\boldsymbol{\Gamma}(x_I)$, and $\mathbf{U}(x_I)$ similar to the uniform particle distribution case.

$$
|\mathbf{N}(x_I)| \sim \frac{1}{h}\left[\bar{\delta} \mathcal{O}\left(\bar{z}^2\right) + \frac{1}{2}\left(\bar{\delta}^2 + \bar{\delta} + \frac{1}{12}\right)\mathcal{O}\left(\bar{z}^3\right)\right] + \mathcal{O}\left(h^4\right)
\tag{42}
$$

$$
|\boldsymbol{\Gamma}(x_I) - 1| \sim \left[\bar{\delta} \mathcal{O}\left(\bar{z}^2\right) + \frac{1}{2}\left(\bar{\delta}^2 + \bar{\delta} + \frac{1}{12}\right)\mathcal{O}\left(\bar{z}^3\right)\right] + \mathcal{O}\left(h^4\right)
\tag{43}
$$

$$
|\mathbf{U}(x_I)| \sim h\left[\bar{\delta} \mathcal{O}\left(\bar{z}^3\right) + \frac{1}{2}\left(\bar{\delta}^2 + \bar{\delta} + \frac{1}{12}\right)\mathcal{O}\left(\bar{z}^3\right)\right] + \mathcal{O}\left(h^4\right)
\tag{44}
$$

Asymptotic relations (42), (43), (44) show the interaction between parameters h, $\bar{z}$ and $\bar{\delta}$. The leading terms are second-order in $\left(\frac{\Delta \tilde{x}_I}{\tilde{h}_{I,m}}\right)$, first-order in the nonuniformity parameter $\bar{\delta}$, and order $1/\tilde{h}_{I,m}$ in smoothing length. These properties are independent of the smoothness of the kernel. The relation (42) shows that discretization error of the scheme (27) will ultimately increase if $\tilde{h}_I$ goes to zero and $\left(\frac{\Delta \tilde{x}_I}{\tilde{h}_{I,m}}\right)$ kept constant.

In general (in $\mathbb{R}^n$) and taking into account limited smoothness properties of W (12), the first term in the expression (32) can be bounded in the following way (by applying triangle inequality):

$$
\left\| 2m\left(\boldsymbol{r}_I\right) \mathbf{u}_{,\alpha}\left(\boldsymbol{r}_I\right) \mathbf{N}_\alpha\left(\boldsymbol{r}_I\right) \right\| \leq 2\left(\frac{C\left(\tilde{h}_{I,m}, \Delta \tilde{x}_I\right)}{\tilde{h}_{I,m}}\right) \cdot m\left(\boldsymbol{r}_I\right) \left\| \mathbf{u}_{,\alpha}\left(\boldsymbol{r}_I\right) \right\|.
\tag{45}
$$

$$
\|\mathcal{E}\| \leq C\left(\tilde{h}_{I,m}, \Delta \tilde{x}_I\right) \cdot \left(\frac{1}{6} m\left(\boldsymbol{r}_I\right) \left\| \mathbf{u}_{,\alpha\beta\gamma}\left(\boldsymbol{r}_I\right) \right\| + \frac{1}{2} \left\| \mathbf{u}_{,\alpha\gamma}\left(\boldsymbol{r}_I\right) \right\| \left\| m_{,\beta}\left(\boldsymbol{r}_I\right) \right\| \right) \left(\frac{\Delta \tilde{x}_I^2}{\tilde{h}_{I,m}}\right),
\tag{46}
$$

Combining the results of conservatives estimates (45), (46) and 1D analysis, we can conclude that the total error (discretization and smoothing errors) can be bounded by $C\left(\tilde{h}_{I,m}, \Delta \tilde{x}_I\right) \cdot \left(\frac{\Delta \tilde{x}_I^\omega}{\tilde{h}_{I,m}}\right) + \mathcal{O}\left(\tilde{h}_I^2\right)$, $0 \leq \omega < 2$. The structure of the error is consistent with results presented in [58].

As noted in [50], since the Hessian matrix $\mathbf{H} = \left(\mathbf{u}_{,\alpha\gamma}\left(\boldsymbol{r}_I\right)\right)$ is coupled with the tensor $\boldsymbol{\Gamma}_{\alpha\gamma}$ via inner product, it is difficult to separate them. However, using the identity $[\mathbf{H} : \boldsymbol{\Gamma}] = \text{tr}[\mathbf{H}\boldsymbol{\Gamma}^T]$, along with the fact that both $\mathbf{H}$ and $\boldsymbol{\Gamma}$ are symmetric, one can write the relation as in [50]

$$
\mathbf{u}_{,\omega\gamma} = \left(\mathbf{u}_{,\alpha\beta} \boldsymbol{\Gamma}_{\alpha\beta}\right) \frac{\boldsymbol{\Gamma}_{\omega\gamma}^{-1}}{n} + \boldsymbol{\Gamma}_{\omega\alpha}^{-1} \mathbf{Q}_{\alpha\gamma}.
\tag{47}
$$

The $\mathbf{Q}_{\alpha\beta}$ is a tensor with zero trace:

$$\mathbf{Q}_{\alpha\beta} = \left(\mathbf{u}_{,\alpha\omega}\boldsymbol{\Gamma}_{\omega\beta}\right) - \delta_{\alpha\beta}\left(\mathbf{u}_{,\omega\gamma}\boldsymbol{\Gamma}_{\omega\gamma}\right)/n. \tag{48}$$

Note that tensor $\boldsymbol{\Gamma}$ defined by (33) is identical to $\mathbf{C}^{-1}$, where $\mathbf{C}$ is defined by (24). However, a more general definition of $\boldsymbol{\Gamma}$ (which reduces in some cases to (24)) will be proposed in the upcoming sections. Hence, the maximum accuracy is achieved when

$$(a) \quad \sum_{\mathbf{r}_J \in \Omega_{\mathbf{r}_I, \tilde{h}_I}} V_{\mathbf{r}_J} \overline{\nabla_\alpha W}\left(\mathbf{r}_J - \mathbf{r}_I, \tilde{h}_{IJ}\right) = 0, \quad \forall \alpha;$$

$$(b) \quad \sum_{\mathbf{r}_J \in \Omega_{\mathbf{r}_I, \tilde{h}_I}} V_{\mathbf{r}_J} \left[\mathbf{r}_J^\alpha - \mathbf{r}_I^\alpha\right] \overline{\nabla_\gamma W}\left(\mathbf{r}_J - \mathbf{r}_I, \tilde{h}_{IJ}\right) = \boldsymbol{\Gamma}_{\alpha\beta} = \delta_{\alpha\gamma}, \quad \forall \alpha, \gamma; \tag{49}$$

which is difficult to fulfill simultaneously for different kernel gradients. Therefore, the overall discretization error is bounded by $C\left(\tilde{h}_{I,m}, \Delta\tilde{x}_I\right) \cdot \left(\frac{\Delta\tilde{x}_I^\omega}{\tilde{h}_{I,m}}\right)$, $0 \le \omega < 2$ for any scalar mobility field $m(\mathbf{r}) \in C^1(\Omega) \cap H^2(\Omega)$, $m(\mathbf{r}) \ge 0$ covering the worse and best cases. Note that in order to maintain the results of the above theorem close to the boundary points, additional ghost particles must be added outside the numerical domain. □

In Section 2.1, several options of computing kernel gradients $\overline{\nabla W}(\mathbf{r}_J - \mathbf{r}_I, \tilde{h}_{IJ})$ (i.e., $\nabla_\alpha W$, $\nabla_\alpha \overline{W}$, $\overline{\nabla_\alpha W}$, and $\widetilde{\nabla}_\alpha \overline{W}$) are proposed (15), (16), (17), and (18), respectively. Different kernel gradients have different accuracy with respect to the condition (34) and (49)(a)–(b). For example, the kernel gradient (16) satisfies for any particles distribution condition (49)(a) but not the condition (34) and (49)(b). Kernel gradients (15), (17), and (18) do satisfy (34) for any particles distribution but not the conditions (49)(a)–(b) in general. The condition (49)(a) for kernel gradients (15), (17), and (18) can be satisfied only if the particle distribution is regular enough since there is cancellation by antisymmetric contributions inside the summation.

At the same time, all corrected options $\overline{\nabla^* W}(\mathbf{r}_J - \mathbf{r}_I, \tilde{h}_{IJ})$ (i.e., $\nabla_\gamma^* W$, $\nabla_\alpha^* \overline{W}$, $\overline{\nabla_\alpha^* W}$, and $\widetilde{\nabla}_\alpha^* \overline{W}$) satisfy the condition (49)(b) for any particles distribution but not the conditions (34) and (49)(a). One may decide to use $\overline{\nabla^* W}(\mathbf{r}_J - \mathbf{r}_I, \tilde{h}_{IJ})$ in the discretization scheme (27) which leads to the error with the leading term

$$2m(\mathbf{r}_I)\,\mathbf{u}_{,\alpha}(\mathbf{r}_I) \sum_{\mathbf{r}_J \in \Omega_{\mathbf{r}_I, \tilde{h}_I}} V_{\mathbf{r}_J}\left[\mathbf{r}_J - \mathbf{r}_I\right] \frac{(\mathbf{r}_J - \mathbf{r}_I)\cdot\overline{\nabla^* W}(\mathbf{r}_J - \mathbf{r}_I, \tilde{h}_{IJ})}{\left\|\mathbf{r}_J - \mathbf{r}_I\right\|^2}. \tag{50}$$

This leads to the incorporation of the correction factor into Brookshaw's approximation to reduce the impact of the following matrix $\boldsymbol{\Gamma}_{\alpha\gamma}$ in (32) for the Laplacian approximation.

A different correction factor has been introduced and investigated in [50]. Alternatively, as was discussed in [50], the correction multiplier can be introduced in (27) defined as $[\mathbf{C}_{\alpha\alpha}]/n$ leading to:

$$\langle \nabla\left(m(\mathbf{r}_I)\,\nabla\mathbf{u}(\mathbf{r}_I)\right)\rangle^* = \frac{\mathbf{C}_{\alpha\alpha}}{n}\cdot\langle\nabla\left(m(\mathbf{r}_I)\,\nabla\mathbf{u}(\mathbf{r}_I)\right)\rangle. \tag{51}$$

Fig. 1 shows Laplacian values for the function $\nabla^2(x^2 + y^2)$ using original Brookshaw's approximation (27) with (a) conventional kernel $\nabla_\gamma W$, (b) corrected kernel $\nabla_\gamma^* W$ and corrected Brookshaw's approximation (51) with the conventional kernel $\nabla_\gamma W$. In addition, Fig. 1 shows that the discretization scheme (27) with the $\overline{\nabla^* W}(\mathbf{r}_J - \mathbf{r}_I, \tilde{h}_{IJ})$ kernel gradient is less accurate near the boundary due to the magnitude of the (50) which is related to the associated leading term of the error.

The scheme (27) is widely (almost unconditionally) used in the SPH modeling community. For example, it was used for a thermal conduction [53,66,67], for modeling a viscous diffusion [45], for a vortex spin-down [68] and Rayleigh–Taylor instability, for simulating Newtonian and non-Newtonian flows with a free surface [69] for the comparison of weakly compressible and truly incompressible algorithms, for macroscopic and mesoscopic flows [70], for a simulation of a solid–fluid mixture flow [71]. Recently, it has been used to model electrokinetic flows [72], Dam-break problem and Taylor–Green vortex [36].

There are different numerical SPH schemes used in numerical simulations. High order accuracy approximations can also be derived by using the SPH discretization on the higher order Taylor series expansion [55,15,50,73]. However, it is usually required that the discrete numerical schemes can reproduce linear fields [59,74,39,40] or polynomials up to a given order [75,14].
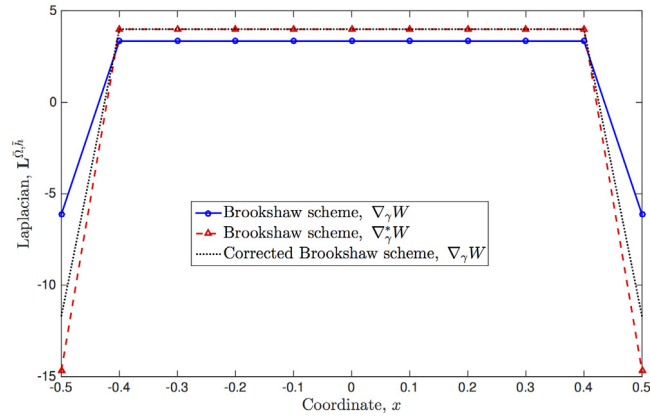
Fig. 1. Values for $\nabla^2(x^2 + y^2)$ along $y = 0$ using Brookshaw's approximation with (a) conventional kernel $\nabla_\gamma W$, (b) corrected kernel $\nabla_\gamma^* W$ and with the correction multiplier $[\mathbf{C}_{\alpha\alpha}]/n$. The numerical domain is a unit square in $\mathbb{R}^2$ with the center at $a_i = 0$, $\forall i$ and side length $L = 1$. The cubic spline (12) was used with $\tilde{h} = f \cdot \Delta x$, $\Delta x = 0.1$, $f = 1.0$.

2.4. Schwaiger's scheme (2008)

The correction terms to the Brookshaw formulation which improve the accuracy of the Laplacian operator near boundaries were proposed by Schwaiger in [50]:

$$\frac{n}{\Gamma_{kk}^{-1}} \langle \nabla \left(m\left(\mathbf{r}_I\right) \nabla \mathbf{u}\left(\mathbf{r}_I\right)\right)\rangle =$$

$$\left\{ \sum_{\mathbf{r}_J \in \Omega_{\mathbf{r}_I, \tilde{h}_I}} V_{\mathbf{r}_J} \left[\mathbf{u}\left(\mathbf{r}_J\right) - \mathbf{u}\left(\mathbf{r}_I\right)\right] \frac{\left(\mathbf{r}_J - \mathbf{r}_I\right) \cdot \left(m_J + m_I\right) \overline{\nabla W}\left(\mathbf{r}_J - \mathbf{r}_I, \tilde{h}_{IJ}\right)}{\left\|\mathbf{r}_J - \mathbf{r}_I\right\|^2} \right\} - \tag{52}$$

$$\left\{ \left[\langle \nabla_\alpha \left(m\left(\mathbf{r}_I\right) \mathbf{u}\left(\mathbf{r}_I\right)\right)\rangle - \mathbf{u}\left(\mathbf{r}_I\right) \langle \nabla_\alpha m\left(\mathbf{r}_I\right)\rangle + m\left(\mathbf{r}_I\right) \langle \nabla_\alpha \mathbf{u}\left(\mathbf{r}_I\right)\rangle \right] \mathbf{N}^\alpha \right\},$$

$$\mathbf{N}^\alpha\left(\mathbf{r}_I\right) = \left[\sum_{\mathbf{r}_J \in \Omega_{\mathbf{r}_I, \tilde{h}_I}} V_{\mathbf{r}_J} \overline{\nabla_\alpha W}\left(\mathbf{r}_I - \mathbf{r}_J, \tilde{h}_{IJ}\right) \right], \tag{53}$$

$$\langle \nabla_\alpha \mathbf{u}\left(\mathbf{r}_I\right)\rangle = \sum_{\mathbf{r}_J \in \Omega_{\mathbf{r}_I, \tilde{h}_I}} V_{\mathbf{r}_J} \left[\mathbf{u}\left(\mathbf{r}_J\right) - \mathbf{u}\left(\mathbf{r}_I\right)\right] \overline{\nabla_\alpha^* W}\left(\mathbf{r}_I - \mathbf{r}_J, \tilde{h}_{IJ}\right), \tag{54}$$

where $n = 1, 2, 3$ is the spatial dimension and the tensor $\Gamma_{\alpha\beta}$ should be defined in general as follows (differently to the expression (33))

$$\Gamma_{\alpha\beta}\left(\mathbf{r}_I\right) = \sum_{\mathbf{r}_J \in \Omega_{\mathbf{r}_I, \tilde{h}_I}} V_{\mathbf{r}_J} \frac{\left(\mathbf{r}_J^\gamma - \mathbf{r}_I^\gamma\right) \overline{\nabla_\gamma W}\left(\mathbf{r}_J - \mathbf{r}_I, \tilde{h}_{IJ}\right)}{\left\|\mathbf{r}_J - \mathbf{r}_I\right\|^2} \left(\mathbf{r}_J^\alpha - \mathbf{r}_I^\alpha\right)\left(\mathbf{r}_J^\beta - \mathbf{r}_I^\beta\right). \tag{55}$$

The gradient $\langle \nabla_\alpha \mathbf{u}\left(\mathbf{r}_I\right)\rangle$ is the corrected gradient which can reproduce linear fields [59,74]. For multi-dimensional problems, the correction tensor $\Gamma_{\alpha\beta}\left(\mathbf{r}_I\right)$ is a matrix. If the particle $\mathbf{r}_I$ has entire stencil support (i.e., the domain support for all kernels $W\left(\mathbf{r}_J - \mathbf{r}_I, \tilde{h}_{IJ}\right)$ is entire and symmetric) then $\Gamma_{\alpha\beta}\left(\mathbf{r}_I\right) \approx \delta_{\alpha\beta}$.

Lemma 1. *The following identities are valid for* $\overline{\nabla_\gamma W}\left(\mathbf{r}_J - \mathbf{r}_I, \tilde{h}_{IJ}\right)$ *described by* (15) *and* (17) *and* (18):

$$\left[\mathbf{r}_J^\alpha - \mathbf{r}_I^\alpha\right] \frac{\left(\mathbf{r}_J^\gamma - \mathbf{r}_I^\gamma\right) \overline{\nabla_\gamma W}\left(\mathbf{r}_J - \mathbf{r}_I, \tilde{h}_{IJ}\right)}{\left\|\mathbf{r}_J - \mathbf{r}_I\right\|^2} =$$

$$\tag{56}$$

$$= -\frac{1}{\tilde{h}_{IJ}} G(z_J, \mathbf{r}_I) \frac{\left[\mathbf{r}_J^\alpha - \mathbf{r}_I^\alpha\right]}{\left\|\mathbf{r}_J - \mathbf{r}_I\right\|} = \overline{\nabla_\alpha W}\left(\mathbf{r}_J - \mathbf{r}_I, \tilde{h}_{IJ}\right),$$

where $z_J = \left\|\mathbf{r}_J - \mathbf{r}_I\right\| / \tilde{h}_{IJ}$, $\forall \mathbf{r}_J, \mathbf{r}_I \in \Omega \subset \mathbb{R}^n$.

Proof. These identities can be established by applying chain rule differentiation. □

Proposition 1. *The correction tensors $\boldsymbol{\Gamma}$ (described by (55)) and $\mathbf{C}^{-1}$ (where $\mathbf{C}$ is defined by (24)) are the symmetrical and identical tensors for $\overline{\nabla_\gamma W}$ described by (15) and (17) and (18).*

Proof. The following relation can be established (using Lemma 1):

$$
\boldsymbol{\Gamma}_{\alpha\beta}\left(\mathbf{r}_I\right) = \sum_{\mathbf{r}_J \in \Omega_{\mathbf{r}_I, \tilde{h}_I}} V_{\mathbf{r}_J} \frac{\left(\mathbf{r}_J^\gamma - \mathbf{r}_I^\gamma\right) \overline{\nabla_\gamma W}\left(\mathbf{r}_J - \mathbf{r}_I, \tilde{h}_{IJ}\right)}{\left\|\mathbf{r}_J - \mathbf{r}_I\right\|^2} \left(\mathbf{r}_J^\alpha - \mathbf{r}_I^\alpha\right)\left(\mathbf{r}_J^\beta - \mathbf{r}_I^\beta\right) =
$$

$$
= -\sum_{\mathbf{r}_J \in \Omega_{\mathbf{r}_I, \tilde{h}_I}} V_{\mathbf{r}_J} \frac{G(z_J, \mathbf{r}_I)}{\tilde{h}_{IJ}} \frac{\left(\mathbf{r}_J^\alpha - \mathbf{r}_I^\alpha\right)\left(\mathbf{r}_J^\beta - \mathbf{r}_I^\beta\right)}{\left\|\mathbf{r}_J - \mathbf{r}_I\right\|} = -\sum_{\mathbf{r}_J \in \Omega_{\mathbf{r}_I, \tilde{h}_I}} V_{\mathbf{r}_J} \frac{G(z_J, \mathbf{r}_I)}{\tilde{h}_{IJ}} \frac{\left(\mathbf{r}_J^\beta - \mathbf{r}_I^\beta\right)\left(\mathbf{r}_J^\alpha - \mathbf{r}_I^\alpha\right)}{\left\|\mathbf{r}_J - \mathbf{r}_I\right\|} \tag{57}
$$

$$
= \boldsymbol{\Gamma}_{\beta\alpha}\left(\mathbf{r}_I\right) = \sum_{\mathbf{r}_J \in \Omega_{\mathbf{r}_I, \tilde{h}_I}} V_{\mathbf{r}_J} \left[\mathbf{r}_J^\alpha - \mathbf{r}_I^\alpha\right] \overline{\nabla_\beta W}\left(\mathbf{r}_J - \mathbf{r}_I, \tilde{h}_{IJ}\right), \qquad \boldsymbol{\Gamma}\left(\mathbf{r}_I\right) = \mathbf{C}^{-1}\left(\mathbf{r}_I\right). \quad □
$$

It follows that the scheme (52)–(54) requires to use the trace of $\boldsymbol{\Gamma}_{\alpha\beta}^{-1}\left(\mathbf{r}_I\right)$ or $\mathbf{C}_{\alpha\beta}\left(\mathbf{r}_I\right)$. The trace of $\boldsymbol{\Gamma}_{\alpha\beta}\left(\mathbf{r}_I\right)$ provides to us the sum of all eigenvalues. It does not give us any range for the eigenvalues which is necessary to estimates $\mathbf{C}_{\alpha\alpha}\left(\mathbf{r}_I\right)$. Even if we have a positive trace we can still theoretically have several small and large eigenvalues with an opposite sign. Before we get to the analysis of the eigenvalues, it is convenient to introduce a condition for matrices known as strictly diagonally dominant (SDD). The diagonal elements of a matrix are noted by indices $\{\alpha\alpha\}$, $1 \leq \alpha \leq n$.

Definition 6. A square matrix $\mathbf{A} = \left(a_{\alpha\beta}\right)_{1 \leq \alpha \leq n, 1 \leq \beta \leq n} \in \mathbb{R}^{n \times n}$ is called strictly diagonally dominant matrix if $|a_{\{\alpha\alpha\}}| > \sum_{\beta \neq \alpha} |a_{\alpha\beta}| \, \forall \alpha$.

Hence, the following Lemma can be formulated.

Lemma 2. *The diagonal elements of the matrix $\boldsymbol{\Gamma}_{\alpha\beta}\left(\mathbf{r}_I\right)$ are positive and the trace of $\boldsymbol{\Gamma}_{\alpha\beta}\left(\mathbf{r}_I\right)$ is bounded, i.e. $\boldsymbol{\Gamma}_{\{\alpha\alpha\}}\left(\mathbf{r}_I\right) \geq 0 \, \forall \alpha$ for all kernel $\overline{\nabla_\gamma W}\left(\mathbf{r}_J - \mathbf{r}_I, \tilde{h}_{IJ}\right)$ defined by (15) and (17) and (18) with $G(z_J, \mathbf{r}_I) \leq 0 \, \forall z_J$ and $\boldsymbol{\Gamma}_{\beta\beta}\left(\mathbf{r}_I\right) \leq \sum_{\mathbf{r}_J \in \Omega_{\mathbf{r}_I, \tilde{h}_I}} V_{\mathbf{r}_J} |G(z_J, \mathbf{r}_I)|$. Furthermore, if matrix $\boldsymbol{\Gamma}_{\alpha\beta}\left(\mathbf{r}_I\right)$ is strictly diagonally dominant matrix then all eigenvalues $\lambda\left(\boldsymbol{\Gamma}_{\alpha\beta}\left(\mathbf{r}_I\right)\right) > 0.$*

Proof. It follows from the fact that:

$$
\boldsymbol{\Gamma}_{\{\alpha\alpha\}}\left(\mathbf{r}_I\right) = -\sum_{\mathbf{r}_J \in \Omega_{\mathbf{r}_I, \tilde{h}_I}} V_{\mathbf{r}_J} \frac{\left(\mathbf{r}_J^\alpha - \mathbf{r}_I^\alpha\right)^2}{\tilde{h}_{IJ} \left\|\mathbf{r}_J - \mathbf{r}_I\right\|} G(z_J, \mathbf{r}_I) \geq 0, \quad G(z_J, \mathbf{r}_I) \leq 0 \quad \forall z_J; \tag{58}
$$

$$
\boldsymbol{\Gamma}_{\beta\beta}\left(\mathbf{r}_I\right) = -\sum_{\mathbf{r}_J \in \Omega_{\mathbf{r}_I, \tilde{h}_I}} V_{\mathbf{r}_J} \left\|\mathbf{r}_J - \mathbf{r}_I\right\| \frac{1}{\tilde{h}_{IJ}} G(z_J, \mathbf{r}_I) \geq 0, \quad \frac{\left\|\mathbf{r}_J - \mathbf{r}_I\right\|}{\tilde{h}_{IJ}} \leq 1, \quad G(z_J, \mathbf{r}_I) \leq 0 \quad \forall z_J; \tag{59}
$$

where the summation by repeating Greek indices is assumed throughout this paper. In order to figure out what range the eigenvalues of the strictly diagonally dominant matrix $\boldsymbol{\Gamma}_{\alpha\beta}\left(\mathbf{r}_I\right)$ (i.e., $-\sum_{\beta \neq \alpha} |\boldsymbol{\Gamma}_{\alpha\beta}\left(\mathbf{r}_I\right)| + \boldsymbol{\Gamma}_{\{\alpha\alpha\}}\left(\mathbf{r}_I\right) > 0$, $\boldsymbol{\Gamma}_{\{\alpha\alpha\}}\left(\mathbf{r}_I\right) > 0$) would be in, we use Gershgorin's theorem:

$$
0 < -\sum_{\beta \neq \alpha} |\boldsymbol{\Gamma}_{\alpha\beta}| + \boldsymbol{\Gamma}_{\{\alpha\alpha\}} \leq \lambda \leq \sum_{\beta \neq \alpha} |\boldsymbol{\Gamma}_{\alpha\beta}| + \boldsymbol{\Gamma}_{\{\alpha\alpha\}}, \quad \alpha \in \{1, \ldots, n\} \quad □ \tag{60}
$$

Remark 3. Since strictly diagonally dominant matrices are always nonsingular, the correction matrix $\mathbf{C}_{\alpha\beta}\left(\mathbf{r}_I\right)$ can be defined and $\mathbf{C}_{\alpha\alpha}\left(\mathbf{r}_I\right) = \sum_{\alpha=1}^{n} \frac{1}{\lambda_\alpha\left(\boldsymbol{\Gamma}_{\gamma\omega}\left(\mathbf{r}_I\right)\right)} > 0$.

The correction matrix $\boldsymbol{\Gamma}_{\alpha\beta}$ is strictly diagonally dominant for the homogeneous and symmetrical particles distribution subject to the full compact support of the kernel. In addition, it is important to note that

$$
\boldsymbol{\Gamma}_{\alpha\beta} = \sum_{\mathbf{r}_J \in \Omega_{\mathbf{r}_I, \tilde{h}_I}} V_{\mathbf{r}_J} \left(\mathbf{r}_J^\alpha - \mathbf{r}_I^\alpha\right) \cdot \overline{\nabla_\beta^* W}\left(\mathbf{r}_J - \mathbf{r}_I, \tilde{h}_{IJ}\right) = \delta_{\alpha\beta} \tag{61}
$$

in the case of using only the corrected gradient $\overline{\nabla_\beta^* W}$ and, hence, $\dfrac{\Gamma_{\alpha\alpha}^{-1}}{n} = 1$. However, $\overline{\nabla_\gamma^* W}$ does not satisfy relation (56). For multi-dimensional problems, the correction tensor $\Gamma_{\alpha\beta}(\boldsymbol{r}_I)$ is a matrix. If the particle $\boldsymbol{r}_I$ has entire stencil support (i.e., the domain support for all kernels $W\left(\boldsymbol{r}_J - \boldsymbol{r}_I, \tilde{h}_{IJ}\right)$ is entire and symmetric) then $\Gamma_{\alpha\beta}(\boldsymbol{r}_I) \approx \delta_{\alpha\beta}$. Unfortunately, $\Gamma_{\alpha\beta}(\boldsymbol{r}_I)$ deviates from $\delta_{\alpha\beta}$ for the provided algorithm and, hence, it is important to minimize this deviation from $\delta_{\alpha\beta}$ in the new methods.

Finding neighbors of a particle in SPH is computationally costly major task in meshless methods. Hence, this task has a significant impact on the overall computational cost and specifically in dynamics simulations involving repositioning of the particles with the time [76]. The typical complexity of the nearest neighbor search algorithm, which can be used in any particle method is of $\mathcal{O}(N \log N)$ [77]. To calculate coefficients in the scheme (52)–(55) is a trivial task and it is $\mathcal{O}(N)$. However, in general, it should be performed at each Newton–Raphson iteration in the non-linear case (i.e., $m = m(\mathbf{u}(\boldsymbol{r}_I))$). It also requires additional efforts to compute the correction matrices $\mathbf{C}_{\alpha\beta}$ and $\Gamma_{\alpha\beta}$ (inversion of $n \times n$ matrices per each particle, where $n = 1, 2, 3$ is the spatial dimension) when they are different (please see Proposition 1) and storage cost of $\overline{\nabla_\alpha W}\left(\boldsymbol{r}_J - \boldsymbol{r}_I, \tilde{h}_{IJ}\right)$, $\overline{\nabla_\alpha^* W}\left(\boldsymbol{r}_J - \boldsymbol{r}_I, \tilde{h}_{IJ}\right)$, and corresponding $\Gamma_{\alpha\alpha}^{-1}$ per each particle.

Theorem 2. *The discretization scheme* (52)–(55) *at a given point* $\boldsymbol{r}_I \in \Omega \subset \mathbb{R}^n$ *sufficiently far away from the boundary* $\partial\Omega$ *(i.e., where the kernel W has a full support and particle volumes satisfy the SPH continuity condition* (21)*) has an error (discretization error) bounded by* $C\left(\tilde{h}_{I,m}, \Delta\tilde{x}_I\right) \cdot \left(\dfrac{\Delta\tilde{x}_I^\omega}{\tilde{h}_{I,m}}\right)$, $1 \leq \omega < 2$ *for any scalar mobility field* $m(\boldsymbol{r}) \in C^1(\Omega) \cap$ $H^2(\Omega)$, $m(\boldsymbol{r}) \geq 0$, *where* $\Delta\tilde{x}_I = \sup_{J:\boldsymbol{r}_J \in \Omega}\|\boldsymbol{r}_J - \boldsymbol{r}_I\|$, $\tilde{h}_{I,m} = \inf_{J:\boldsymbol{r}_J \in \Omega_{\boldsymbol{r}_I,\tilde{h}_I}}\tilde{h}_{IJ}$.

Proof. Using Lemma 1 and Proposition 1, additional terms proposed by Schwaiger [50] reduce to

$$[\langle \nabla_\alpha m(\boldsymbol{r}_I)\mathbf{u}(\boldsymbol{r}_I)\rangle - \mathbf{u}(\boldsymbol{r}_I)\langle\nabla_\alpha m(\boldsymbol{r}_I)\rangle + m(\boldsymbol{r}_I)\langle\nabla_\alpha\mathbf{u}(\boldsymbol{r}_I)\rangle]\mathbf{N}^\alpha =$$

$$= 2m(\boldsymbol{r}_I)\mathbf{u}_\alpha(\boldsymbol{r}_I) \cdot \mathbf{N}^\alpha + m_{,\beta}(\boldsymbol{r}_I)\mathbf{u}_{,\omega}(\boldsymbol{r}_I)\mathbf{U}_{\omega\beta\alpha}^* \cdot \mathbf{N}^\alpha + \qquad (62)$$
$$m(\boldsymbol{r}_I)\mathbf{u}_{,\beta\omega}(\boldsymbol{r}_I)\mathbf{U}_{\omega\beta\alpha}^* \cdot \mathbf{N}^\alpha + \tilde{\mathcal{E}}$$

in the vicinity of the point $\boldsymbol{r}_I$ with the error $\tilde{\mathcal{E}}$. Where

$$\mathbf{U}_{\omega\beta\alpha}^*(\boldsymbol{r}_I) = \sum_{\boldsymbol{r}_J \in \Omega_{\boldsymbol{r}_I,h}} V_{\boldsymbol{r}_J}\left[\boldsymbol{r}_J^\omega - \boldsymbol{r}_I^\omega\right]\left[\boldsymbol{r}_J^\beta - \boldsymbol{r}_I^\beta\right]\overline{\nabla_\alpha^* W}\left(\boldsymbol{r}_J - \boldsymbol{r}_I, \tilde{h}_{IJ}\right).$$

The expression (62) has the leading term outlined in (32). Subtraction of these terms from (32) leads to

$$\langle\nabla(m(\boldsymbol{r}_I)\nabla\mathbf{u}(\boldsymbol{r}_I))\rangle = m(\boldsymbol{r}_I)\mathbf{u}_{,\alpha\beta}(\boldsymbol{r}_I)\Gamma_{\alpha\beta}^* + m_{,\alpha}(\boldsymbol{r}_I)\mathbf{u}_{,\beta}(\boldsymbol{r}_I)\Gamma_{\alpha\beta}^* + \tilde{\mathcal{E}} + \mathcal{E}, \qquad (63)$$

where

$$\Gamma_{\alpha\beta}^* = \Gamma_{\alpha\beta} - \mathbf{U}_{\alpha\beta\omega}^* \cdot \mathbf{N}^\omega \qquad (64)$$

and performing the normalization lead to the announced in the theorem result. Note that in order to maintain the results of the above theorem close to the boundary points additional ghost particles must be added outside the numerical domain. $\square$

It follows that the usage of $\Gamma_{\alpha\beta}^*$ instead of $\Gamma_{\alpha\beta}$ in (52) will improve the accuracy of the scheme (52)–(55). Furthermore, if one uses $\overline{\nabla W}(\boldsymbol{r}_J - \boldsymbol{r}_I, \tilde{h}_{IJ})$ in place of $\overline{\nabla^* W}(\boldsymbol{r}_J - \boldsymbol{r}_I, \tilde{h}_{IJ})$ in the first term of the discretization scheme (52) then the definition for $\mathbf{N}^\alpha$ has to be modified in accordance of (50) to maintain the higher order discretization accuracy, for example, as:

$$\widetilde{\mathbf{N}}^\alpha = \sum_{\boldsymbol{r}_J \in \Omega_{\boldsymbol{r}_I,\tilde{h}_I}} V_{\boldsymbol{r}_J}\left[\boldsymbol{r}_J^\alpha - \boldsymbol{r}_I^\alpha\right]\frac{(\boldsymbol{r}_J - \boldsymbol{r}_I)\overline{\nabla W}\left(\boldsymbol{r}_J - \boldsymbol{r}_I, \tilde{h}_{IJ}\right)}{\|\boldsymbol{r}_J - \boldsymbol{r}_I\|^2}, \quad \forall\alpha \qquad (65)$$

which reduces to the conventional $\mathbf{N}^\alpha$ in the case of $\overline{\nabla W}(\boldsymbol{r}_J - \boldsymbol{r}_I, \tilde{h}_{IJ}) \neq \overline{\nabla^* W}(\boldsymbol{r}_J - \boldsymbol{r}_I, \tilde{h}_{IJ})$ and subject to the conditions of Lemma 1. Fig. 2 shows the Laplacian for the function $\nabla^2(x^2 + y^2)$ using Schwaiger's approximation (52)–(55) with (a) conventional kernel $\nabla_\gamma W$ and (b) corrected kernel $\nabla_\gamma^* W$.
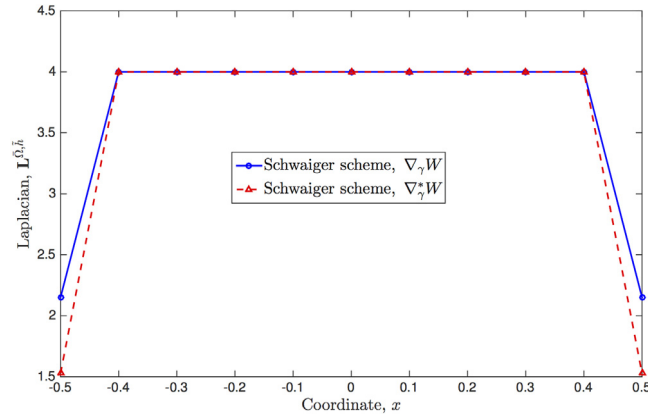
Fig. 2. Values for $\nabla^2(x^2 + y^2)$ along $y = 0$ using Schwaiger's approximation with (a) conventional kernel $\nabla_\gamma W$ and (b) corrected kernel $\nabla_\gamma^* W$. The numerical domain is a unit square in $\mathbb{R}^2$ with the center at $a_i = 0$, $\forall i$. The cubic spline (12) was used with $\tilde{h} = f \cdot \varDelta x$, $\varDelta x = 0.1$, $f = 1.0$.

3. Meshless transmissibilities

The well-known two-point flux approximation (TPFA) is a mesh dependent numerical scheme used in solving elliptic equation (1): $\mathbf{L}(\mathbf{u}) = 0$ with the diagonal matrix of coefficients $\mathbf{M}$. The net flow rate from a cell I into neighboring cells in this scheme is obtained by summing fluxes over the neighboring cells J:

$$\boldsymbol{q} = \sum_J \widetilde{T}_{JI} \left[\mathbf{u}\left(\boldsymbol{r}_J\right) - \mathbf{u}\left(\boldsymbol{r}_I\right) \right], \quad \widetilde{T}_{JI} \geq 0, \tag{66}$$

where $\widetilde{T}_{JI}$ is the transmissibility between cells J and I, $\boldsymbol{q}$ is the total flux through the boundary of the control volume located at the point $\boldsymbol{r}_I$. The transmissibility $\widetilde{T}_{JI}$ defined at an interior face f between cells J and I is calculated as

$$\widetilde{T}_{JI} = \frac{1}{\left[\dfrac{\left\| \boldsymbol{r}_{f,J} \right\|^2}{\boldsymbol{S}_f \mathbf{M} \boldsymbol{r}_{f,J}} + \dfrac{\left\| \boldsymbol{r}_{f,I} \right\|^2}{\boldsymbol{S}_f \mathbf{M} \boldsymbol{r}_{f,I}} \right]}, \tag{67}$$

where $\boldsymbol{r}_{f,J}$ and $\boldsymbol{r}_{f,I}$ are the vectors from centers of cells J and I to the face f respectively, $\boldsymbol{S}_f$ is the area vector of the face f. In the case of $\mathbf{M}$-orthogonal mesh, when $\mathbf{M}\boldsymbol{S}_f$ and $\left[\boldsymbol{r}_J - \boldsymbol{r}_I \right]$ are collinear, the expression (66) reduces to the form of the central finite difference scheme and approximates the flux with $\mathcal{O}\left(\max_J \left\| \boldsymbol{r}_J - \boldsymbol{r}_I \right\|^2 \right)$ order of accuracy for any mobility tensor field $\mathbf{M}$. The expression (67) ensures that the flux into the adjoining region is continuous [66]. The TPFA scheme (66) is an unconditionally monotone scheme [52].

It is clear that the expression (52) cannot be written in the form (66) due to terms $\langle \nabla_\alpha \left(m\left(\boldsymbol{r}_I\right) \mathbf{u}\left(\boldsymbol{r}_I\right) \right) \rangle \mathbf{N}^\alpha$ and $\mathbf{u}\left(\boldsymbol{r}_I\right) \langle \nabla_\alpha m\left(\boldsymbol{r}_I\right) \rangle \mathbf{N}^\alpha$. Hence, it is only possible in this case to introduce a definition of a partial meshless transmissibility between particles $\boldsymbol{r}_J$ and $\boldsymbol{r}_I$ as follows:

$$T^P\left(\boldsymbol{r}_J, \boldsymbol{r}_I\right) = T_{JI}^P = \frac{\boldsymbol{\varGamma}_{\beta\beta}^{-1}}{n} \times V_{\boldsymbol{r}_J}$$

$$\left\{ \frac{\left(\boldsymbol{r}_J - \boldsymbol{r}_I\right) \cdot \left(m_J + m_I\right) \cdot \overline{\nabla W}\left(\boldsymbol{r}_J - \boldsymbol{r}_I, \tilde{h}_{IJ}\right)}{\left\| \boldsymbol{r}_J - \boldsymbol{r}_I \right\|^2} - m_I \overline{\nabla W}\left(\boldsymbol{r}_J - \boldsymbol{r}_I, \tilde{h}_{IJ}\right) \mathbf{N} \right\}. \tag{68}$$

It is important to note that transmissibilities T_{JI}^P and $\widetilde{T}_{JI}^P$ have different physical units. Furthermore, it raises the question wherever the scheme (52)–(55) is monotone.

Hence, there is an additional term that has not been taken into account in (52)–(55). The following section describes an alternative numerical scheme for the heterogeneous Laplace operator. Some initial attempts were also made in [78].

3.1. New scheme

The correction terms to the Brookshaw [53] and Schwaiger [50] formulations which improve the accuracy of the Laplacian operator near boundaries can be done as follows:

$$\frac{n}{\bar{\varGamma}^{-1}_{\beta\beta}} \langle \nabla \left(\mathbf{M} \left(\mathbf{r}_I \right) \nabla \mathbf{u} \left(\mathbf{r}_I \right) \right) \rangle =$$

$$\left\{ \sum_{\mathbf{r}_J \in \Omega_{\mathbf{r}_I, \tilde{h}_I}} V_{\mathbf{r}_J} \left[\mathbf{u} \left(\mathbf{r}_J \right) - \mathbf{u} \left(\mathbf{r}_I \right) \right] \frac{\left(\mathbf{r}_J - \mathbf{r}_I \right) \cdot \left(\mathbf{M}_J + \mathbf{M}_I \right) \cdot \overline{\nabla W} \left(\mathbf{r}_J - \mathbf{r}_I, \tilde{h}_{IJ} \right)}{\left\| \mathbf{r}_J - \mathbf{r}_I \right\|^2} \right\} -$$

$$\left\{ \widetilde{\mathbf{N}} \cdot \left(\sum_{\mathbf{r}_J \in \Omega_{\mathbf{r}_I, \tilde{h}_I}} V_{\mathbf{r}_J} \cdot \left(\mathbf{M}_J + \mathbf{M}_I \right) \cdot \left[\mathbf{u} \left(\mathbf{r}_J \right) - \mathbf{u} \left(\mathbf{r}_I \right) \right] \overline{\nabla^* W} \left(\mathbf{r}_J - \mathbf{r}_I, \tilde{h}_{IJ} \right) \right) \right\}, \tag{69}$$

where $n = 1, 2, 3$ is the spatial dimension. The tensor $\bar{\varGamma}_{\alpha\beta}$ can be defined by the relation (55). It is important to stress at this point that it is also applicable to use $\bar{\varGamma}_{\alpha\beta} = \varGamma_{\alpha\beta}$ without losing the monotonicity and stability quality of the scheme. However, the higher accuracy can be achieved by taking into account higher order corrections in $\varGamma_{\alpha\beta} \left(\mathbf{r}_I \right)$ as per relation (64). Hence, the following definition can be used

$$\bar{\varGamma}_{\alpha\beta} \left(\mathbf{r}_I \right), \widetilde{\mathbf{N}} = \begin{cases} \varGamma^*_{\alpha\beta} \left(\mathbf{r}_I \right), \widetilde{\mathbf{N}} \neq 0, & \text{if } \varGamma^*_{\alpha\beta} \left(\mathbf{r}_I \right) \neq 0, \\ \\ \varGamma_{\alpha\beta} \left(\mathbf{r}_I \right), \widetilde{\mathbf{N}} \neq 0, & \text{if } \varGamma^*_{\alpha\beta} \left(\mathbf{r}_I \right) = 0 \end{cases} \tag{70}$$

where

$$\varGamma^*_{\alpha\beta} \left(\mathbf{r}_I \right) = \sum_{\mathbf{r}_J \in \Omega_{\mathbf{r}_I, \tilde{h}_I}} V_{\mathbf{r}_J} \left[r_J^\alpha - r_I^\alpha \right] \overline{\nabla_\beta W} \left(\mathbf{r}_J - \mathbf{r}_I, \tilde{h}_{IJ} \right) -$$

$$\widetilde{\mathbf{N}}^\gamma \sum_{\mathbf{r}_J \in \Omega_{\mathbf{r}_I, \tilde{h}_I}} V_{\mathbf{r}_J} \left[r_J^\alpha - r_I^\alpha \right] \left[r_J^\beta - r_I^\beta \right] \overline{\nabla^*_\gamma W} \left(\mathbf{r}_J - \mathbf{r}_I, \tilde{h}_{IJ} \right) \tag{71}$$

and

$$\varGamma^*_{\{\alpha\alpha\}} \left(\mathbf{r}_I \right) = - \sum_{\mathbf{r}_J \in \Omega_{\mathbf{r}_I, \tilde{h}_I}} V_{\mathbf{r}_J} \frac{\left(r_J^\alpha - r_I^\alpha \right)^2}{\tilde{h}_{IJ} \left\| \mathbf{r}_J - \mathbf{r}_I \right\|} G(z_J, \mathbf{r}_I) \left[1 - \widetilde{\mathbf{N}}^\gamma \left(\mathbf{r}_I \right) \mathbf{C}_{\gamma\omega} \left(\mathbf{r}_I \right) \left(r_J^\omega - r_I^\omega \right) \right], \tag{72}$$

$$\varGamma^*_{\beta\beta} \left(\mathbf{r}_I \right) = - \sum_{\mathbf{r}_J \in \Omega_{\mathbf{r}_I, \tilde{h}_I}} V_{\mathbf{r}_J} \left\| \mathbf{r}_J - \mathbf{r}_I \right\| \frac{1}{\tilde{h}_{IJ}} G(z_J, \mathbf{r}_I) \left[1 - \widetilde{\mathbf{N}}^\gamma \left(\mathbf{r}_I \right) \mathbf{C}_{\gamma\omega} \left(\mathbf{r}_I \right) \left(r_J^\omega - r_I^\omega \right) \right]. \tag{73}$$

Following (69), we only need to compute the trace of the matrix $\bar{\varGamma}^{-1}_{\alpha\beta} \left(\mathbf{r}_I \right)$. Furthermore, it is clear that one can apply results of Lemma 2 to $\varGamma^*_{\beta\beta} \left(\mathbf{r}_I \right)$ with following function

$$G^*(z_J, \mathbf{r}_I) = G(z_J, \mathbf{r}_I) \left[1 - \widetilde{\mathbf{N}}^\gamma \left(\mathbf{r}_I \right) \mathbf{C}_{\gamma\omega} \left(\mathbf{r}_I \right) \left(r_J^\omega - r_I^\omega \right) \right] \qquad \text{if } G^*(z_J, \mathbf{r}_I) \leq 0, \tag{74}$$

where

$$\widetilde{\mathbf{N}} \left(\mathbf{r}_I \right) \mathbf{C} \left(\mathbf{r}_I \right) \left(\mathbf{r}_J - \mathbf{r}_I \right) = \widetilde{\mathbf{N}} \left(\mathbf{r}_I \right) \left[\sum_{\mathbf{r}_J \in \Omega_{\mathbf{r}_I, \tilde{h}_I}} V_{\mathbf{r}_J} \left[\mathbf{r}_J - \mathbf{r}_I \right] \overline{\nabla W} \right]^{-1} \left(\mathbf{r}_J - \mathbf{r}_I \right). \tag{75}$$

The function $G^*(z_J, \mathbf{r}_I)$ is negative if

$$\left[1 - \widetilde{\mathbf{N}}^\gamma \left(\mathbf{r}_I \right) \mathbf{C}_{\gamma\omega} \left(\mathbf{r}_I \right) \left(r_J^\omega - r_I^\omega \right) \right] > 0 \quad \forall \mathbf{r}_J, \mathbf{r}_I. \tag{76}$$

The reason for having the correction factor in the form (70)–(71) is that $\varGamma^*_{\alpha\beta} \left(\mathbf{r}_I \right) = 0$ in some cases, where particles have the incomplete kernel support (e.g., at the corners and boundaries of the numerical domain). For multi-dimensional problems, the correction tensor $\bar{\varGamma}_{\alpha\beta} \left(\mathbf{r}_I \right)$ is also a matrix. If the particle $\mathbf{r}_I$ has entire stencil support (i.e., the domain support for all kernels $W \left(\mathbf{r}_J - \mathbf{r}_I, \tilde{h}_{IJ} \right)$ is completed and symmetric) then $\bar{\varGamma}_{\alpha\beta} \left(\mathbf{r}_I \right) \approx \delta_{\alpha\beta}$. The proposed correction matrix deviates less from the unit matrix compare to (55).

The computation complexity of the proposed scheme is very similar to the scheme (52)–(55). Although, the overall complexity over considered in this paper SPH schemes can be bounded by $\mathcal{O}(N \log N)$ due to nearest neighbor search algorithm, in all problems consider in this paper the nearest neighbor search algorithm is performed once at the pre-processing step. The rest of the computations has the complexity of $\mathcal{O}(N)$. We do not consider here the complexity of the linear solver required to solve resulting algebraic system of equations.

Theorem 3. *The discretization scheme* (69)–(71) *at a given point* $\boldsymbol{r}_I \in \Omega \subset \mathbb{R}^n$ *sufficiently far away from the boundary* $\partial\Omega$ *(i.e., where the kernel W has a full support and particle volumes satisfy the SPH continuity condition* (21)*) has an error (discretization error) bounded by* $C\left(\tilde{h}_{l,m}, \Delta\tilde{x}_I\right) \cdot \left(\dfrac{\Delta\tilde{x}_I^\omega}{\tilde{h}_{l,m}}\right)$, $1 \leq \omega < 2$ *for any scalar mobility field* $m(\boldsymbol{r}) \in C^1(\Omega) \cap H^2(\Omega)$, $m(\boldsymbol{r}) \geq 0$, $\Delta\tilde{x}_I = \sup_{J:\boldsymbol{r}_J \in \Omega}\|\boldsymbol{r}_J - \boldsymbol{r}_I\|$, $\tilde{h}_{l,m} = \inf_{J:\boldsymbol{r}_J \in \Omega_{\boldsymbol{r}_I,\tilde{h}_I}}\tilde{h}_{IJ}$.

Proof. Using Lemma 1, additional term proposed by new scheme (69) subject to the diagonal mobility tensor $\mathbf{M}^{\alpha\beta}(\boldsymbol{r}) = m(\boldsymbol{r})\delta_{\alpha\beta}$ reduces to

$$
\left\{\widetilde{\mathbf{N}} \cdot \left(\sum_{\boldsymbol{r}_J \in \Omega_{\boldsymbol{r}_I,\tilde{h}_I}} V_{\boldsymbol{r}_J} \cdot (m_J + m_I) \cdot \left[\mathbf{u}\left(\boldsymbol{r}_J\right) - \mathbf{u}\left(\boldsymbol{r}_I\right)\right]\overline{\nabla^* W}\left(\boldsymbol{r}_J - \boldsymbol{r}_I, \tilde{h}_{IJ}\right)\right)\right\} =
$$
$$
= 2m(\boldsymbol{r}_I)\,\mathbf{u}_\alpha(\boldsymbol{r}_I) \cdot \widetilde{\mathbf{N}}^\alpha +
$$
$$
m_{,\beta}(\boldsymbol{r}_I)\,\mathbf{u}_{,\omega}(\boldsymbol{r}_I)\left(\sum_{\boldsymbol{r}_J \in \Omega_{\boldsymbol{r}_I,\tilde{h}_I}} V_{\boldsymbol{r}_J}\left[\boldsymbol{r}_J^\omega - \boldsymbol{r}_I^\omega\right]\left[\boldsymbol{r}_J^\beta - \boldsymbol{r}_I^\beta\right]\overline{\nabla_\alpha^* W}\left(\boldsymbol{r}_J - \boldsymbol{r}_I, \tilde{h}_{IJ}\right)\right) \cdot \widetilde{\mathbf{N}}^\alpha + \quad (77)
$$
$$
m(\boldsymbol{r}_I)\,\mathbf{u}_{,\beta\omega}(\boldsymbol{r}_I)\left(\sum_{\boldsymbol{r}_J \in \Omega_{\boldsymbol{r}_I,\tilde{h}_I}} V_{\boldsymbol{r}_J}\left[\boldsymbol{r}_J^\omega - \boldsymbol{r}_I^\omega\right]\left[\boldsymbol{r}_J^\beta - \boldsymbol{r}_I^\beta\right]\overline{\nabla_\alpha^* W}\left(\boldsymbol{r}_J - \boldsymbol{r}_I, \tilde{h}_{IJ}\right)\right) \cdot \widetilde{\mathbf{N}}^\alpha + \hat{\mathcal{E}}
$$

in the vicinity of the point $\boldsymbol{r}_I$ with the error $\hat{\mathcal{E}}$ which has the leading term outlined in (32). Subtraction of these terms from (32) and performing the normalization lead to the announced in the theorem result. Note that in order to maintain the results of the above theorem close to the boundary points, additional ghost particles must be added outside the numerical domain. □

The scheme has the two-point flux approximation nature and can be written in the form of (2), which can be proved using the arguments above. The scheme (69)–(71) is in line with an alternative formulation for continuum mechanics called the peridynamic model [79,80], which was proposed several years ago.

All presented schemes in this paper do not require exact expressions for the gradient (i.e., spatial derivatives) of the mobility field $\nabla_\gamma m(\boldsymbol{r})$ to keep a higher order of accuracy for any mobility field. Hence, this scheme can be used with the discontinuous (or piecewise continuous) mobility field $m(\boldsymbol{r}) \in L_2(\Omega)$. It is important to note that Brookshaw [53] and Schwaiger [50] schemes can also be written for the diagonal mobility matrix $\mathbf{M}^{\alpha\beta}(\boldsymbol{r})$ by substituting $\mathbf{M}^{\alpha\beta}$ into (27) and (52) instead of $m(\boldsymbol{r})$ and performing summation by repeating indices.

4. Approximation, stability, and monotonicity

The approximation, stability and monotonicity are important properties of numerical schemes which provide and quantify the confidence in the numerical modeling and results from corresponding simulations. Therefore, in order to be confident that the proposed numerical schemes provide the adequate accuracy of the elliptic operator (1), several numerical analyses to identify the order of approximation, stability and monotonicity have been performed. It is important to recall that all numerical schemes are characterized by two length scales $\tilde{h}$ and $\Delta\tilde{x}_m$: $\tilde{h} = f \cdot \Delta\tilde{x}_m$. Hence, while investigating the approximation of the meshless discretization scheme, it is important to distinguish two cases: (a) the neighborhood number of particles is fixed $f = $ const with varying the inter-particle distance, (b) the inter-particle distance is fixed $\Delta\tilde{x}_m = $ const with varying the neighborhood number of particles. The first case will be analyzed by looking at the error defined by

$$
\|E\|_\Omega^{L_2} = \left[\frac{1}{\sum_J V_{\boldsymbol{r}_J}}\sum_J V_{\boldsymbol{r}_J}\left(\mathbf{L}\left[\mathbf{u}\left(\boldsymbol{r}_J\right)\right] - \langle\mathbf{L}\rangle\left[\mathbf{u}\left(\boldsymbol{r}_J\right)\right]\right)^2\right]^{1/2}, \quad (78)
$$

where $\mathbf{L}[\cdot]$ is the analytical Laplacian at the particle $\boldsymbol{r}_J$ and $\langle\mathbf{L}\rangle[\cdot]$ is the approximation of the Laplacian at the particle $\boldsymbol{r}_J$, $\|E\|_\Omega^{L_2}$ is the averaged error over the entire domain. In the following paragraph, the numerical analysis is performed for various functions, particle distributions, and media properties.
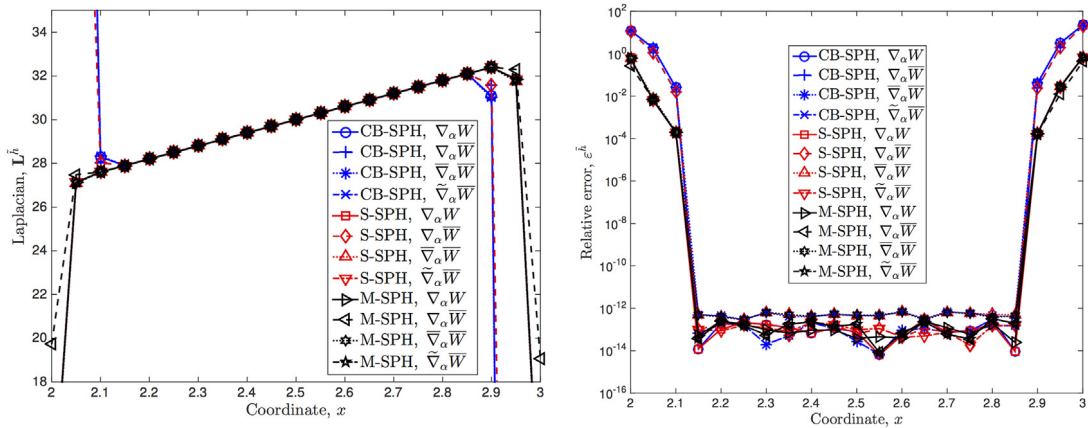
Fig. 3. Cross-section of the test patch at $y = 2.5$. Three SPH approximations of $\nabla^2\left(x^3 + y^3\right)$ with different kernel gradients are shown. Corrected Brookshaw's scheme (CB-SPH) is given by (51) with the correction multiplier, while Schwaiger's scheme (S-SPH) is given by (52)–(55). New approximation (M-SPH) considered here is the SPH form (69)–(71). In this case, the Schwaiger's scheme and new scheme have comparable accuracy at the boundaries and are accurate in the interior to the machine precision. Four different options of computing kernel gradients (i.e., $\nabla_\gamma W$, $\nabla_\alpha W$, $\overline{\nabla}_\alpha \overline{W}$, and $\widetilde{\nabla}_\alpha \overline{W}$) with corresponding corrected kernel gradients are shown.

Following the work [50], the ability of the discretization to reproduce the Laplacian was tested for several functions in $\mathbb{R}^n$, $n = 1, 2, 3$:

$$(a)\; \boldsymbol{u}^s\left(\boldsymbol{x}\right) = \sum_{i=1}^{n} x_i^s, \qquad (b)\; \boldsymbol{u}_m^s\left(\boldsymbol{x}\right) = \prod_{i=1}^{n} x_i^{m_i},\;\; |m| = s; \tag{79}$$

where $m = (m_1, \ldots, m_n)$, $\forall i\; :\; m_i \geq 0$ is the n-dimensional multi-index with the property $|m| = \sum_{i=1}^{n} m_i$. The reason for selecting these testing polynomials is as follows. Since the functional space $L_p\left(\Omega\right)$ is separable, the above polynomials form the everywhere dense subset of the $L_p\left(\Omega\right)$. Hence, any function $\mathbf{u} \in L_p$ can be approximated in L_p using linear combination of the above polynomials leading to the following relations:

$$\mathbf{u}(\boldsymbol{r}) \approx \sum_{k=1}^{\infty} \sum_{|m|\leq k} a_m \left(\prod_{i=1}^{n} x_i^{m_i}\right), \qquad \mathbf{M}\left(\boldsymbol{r}\right) \approx \sum_{k=1}^{\infty} \sum_{|m|\leq k} b_m \left(\prod_{i=1}^{n} x_i^{m_i}\right). \tag{80}$$

The approximation error produced by the discretization schemes and considered in this paper for the polynomials $\boldsymbol{u}^s\left(\boldsymbol{x}\right)$ and $\boldsymbol{u}_m^s\left(\boldsymbol{x}\right)$ gives the information about the error growth for the arbitrary function $\mathbf{u}(\boldsymbol{r})$. In each test, the homogeneous and heterogeneous particle distribution varying the smoothing length $\tilde{h}$ and inter-particle distance $\Delta\tilde{x}_m$ are used to study the approximation properties of the proposed discretization scheme.

4.1. Isotropic homogeneous media

Note that in the limit of the homogeneous isotropic media (i.e., $\mathbf{M}^{\alpha\beta}\left(\boldsymbol{r}\right) = m\left(\boldsymbol{r}\right)\delta_{\alpha\beta}$, $m\left(\boldsymbol{r}\right) = 1$) and without the source term, the aforementioned operator $\mathbf{L}\left(\mathbf{u}\right)$ in (1) reduces to the conventional Laplacian operator (i.e., $\mathbf{L}\left(\mathbf{u}\right) \equiv \nabla^2\mathbf{u}$). The domain for the patch test is a unit square similar to [50] for $n = 2$:

$$\Omega = \left\{\boldsymbol{r} = \{x_\alpha\} \in \mathbb{R}^n \mid\; |x_\alpha - 2.5| \leqslant \frac{1}{2}\;\;\; \forall\alpha\right\}$$

with $N = 21$ particles in each direction characterized by two length scales: $\tilde{h} = f \cdot \Delta\tilde{x}_m$, $\Delta\tilde{x}_m = 0.05, f = 1.2$.

In all of the following tests, the results are displayed along the cross-section $y = 2.5$ in $\mathbb{R}^n$, $n = 2$ (similar to [50] for $n = 2$). In each test, the following discretizations are compared: corrected Brookshaw's scheme (CB-SPH) (51), Schwaiger's scheme (S-SPH) (52)–(55), and new proposed scheme (M-SPH) (69)–(71). Note that the Schwaiger's scheme was tested against several schemes published in [62,49] and show better accuracy; hence, schemes in [62,49] are not considered in this paper. The comparison of different schemes starts with test functions of the form $\boldsymbol{u}^s\left(\boldsymbol{x}\right)$ described by (79)(a) in $\mathbb{R}^n$, $n = 2$. Plots of the Laplacian approximations and the relative errors defined by (78) for the case $m = 3$ are shown in Fig. 3. Note that it is important for the accurate solution of different boundary value problems to have an accurate approximation of the considered Laplace operator in the internal particles only. The additional relation will be supplied to approximate boundary conditions in the following section, e.g. (100).

The new scheme (M-SPH) has the greatest accuracy at the boundary and is accurate to machine precision ε in the interior. The same behavior is observed in 3D where the M-SPH scheme with the $\nabla_\alpha \overline{W}$ is the most accurate scheme.
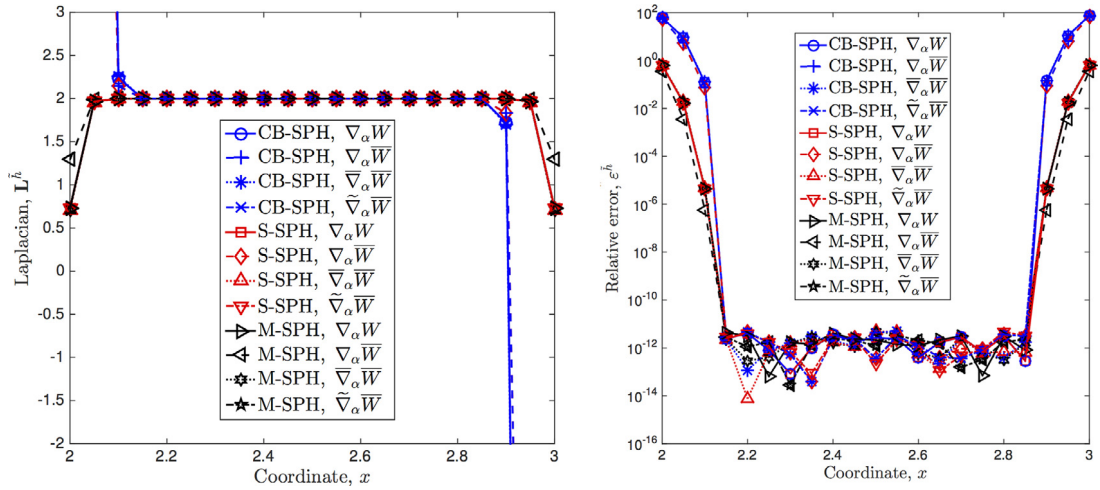
Fig. 4. Cross-section of the test patch at $y = 2.5$. Three SPH approximations of $\nabla((x + y)(\nabla(x + y)))$ with different kernel gradients are shown. The different schemes and kernel gradients are described in the caption of Fig. 3.

Furthermore, the new scheme should be tested for the functions requiring cross-derivatives as was reported in [50]. To examine the effect of the cross-derivative terms, the same suite of tests was run with the function $\boldsymbol{u}_m^s(\boldsymbol{x})$ described by (79)(b) in $\mathbb{R}^n$, $n = 2, 3$. Relative errors for $(xy)^m$ on a same array as in Fig. 3 along $y = 2.5$ were computed and again the proposed scheme (69)–(71) was uniformly more accurate for the various experiments. The behavior of each discretization is similar to that shown in Fig. 3. The proposed new scheme (M-SPH) performed nearly as well as the Schwaiger's scheme at the boundary. The CB-SPH and S-SPH forms also perform with greater accuracy than all other forms in the interior except in the case with the highest exponent.

An additional concern is that although it deviates from the exact solution near boundaries, it acquires no off-diagonal terms due to the alignment of the array of particles and the boundaries with the coordinate axes. To test the accuracy of the new approximations when there are off-diagonal terms, an array with particles rotated $45°$ was used with the test function $(xy)^m$ (similar to [50]). The new proposed scheme formulation performs consistently well for lower exponents.

4.2. Isotropic heterogeneous media

In isotropic heterogeneous media, i.e., $\mathbf{M}^{\alpha\beta}(\boldsymbol{r}) = m(\boldsymbol{r})\delta_{\alpha\beta}$, the Laplace operator takes the general form written in (1). The numerical domain is the same as in the previous section with the same number of particles and particle length scales: $\tilde{h} = f \cdot \varDelta \tilde{x}_m$, $\varDelta \tilde{x}_m = 0.05$, $f = 1.2$. Plots of the Laplacian approximations and the relative errors defined by (78) for the case of heterogeneous mobility with $m = 1$ (see (80)) are shown in Fig. 4. The new scheme (M-SPH) has the best accuracy at the boundary and is accurate to machine precision ε in the interior. The error has also been computed for test functions with exponents from $m = 2, \ldots, 5$. For these functions, the proposed scheme (69)–(71) is uniformly more accurate for the different increasing exponents. The same behavior is observed in 3D where M-SPH scheme with the $\nabla_\alpha \overline{W}$ is the most accurate scheme.

4.3. von Neumann stability analysis

For linear PDEs, there is the Lax-equivalence theorem which connects the consistency and stability with the convergence. The idea of the von Neumann stability analysis is to study the growth of waves $\lambda e^{i\boldsymbol{k}\cdot\boldsymbol{r}}$ (similar to Fourier methods). After applying one of the discretization methods above to the Laplace operator (1), the following relation can be written:

$$\frac{\{\mathbf{u}\}^{n+1} - \{\mathbf{u}\}^n}{\tau} - \mathbf{L}^{\tilde{h}}\left[\{\mathbf{u}\}^n\right] = \{\boldsymbol{b}\}, \tag{81}$$

where τ is the iteration parameter (e.g., time step), n is the iteration index (e.g., time index), $\{\mathbf{u}\}^n = \left(\boldsymbol{u}_1^n, \ldots, \boldsymbol{u}_N^n\right)$ is a vector of all N particle values $\boldsymbol{u}_i^n$, $i = 1, \ldots, N$, $\{\boldsymbol{b}\} = (\boldsymbol{b}_1, \ldots, \boldsymbol{b}_N)$ is the right-hand side vector. The expression (81) may represent, for example, discretization of the parabolic PDE or an iterative solver of the linear system of equations arising from discretization of elliptic boundary value problem. Substituting into the left-hand side of the relation (81) the following form of perturbation

$$\boldsymbol{u}_j^n = \lambda^n e^{i\boldsymbol{k}_j \cdot \boldsymbol{r}_j} = \lambda^n \cdot \prod_{l=1}^n e^{ik_j^l \cdot x_j^l} \tag{82}$$
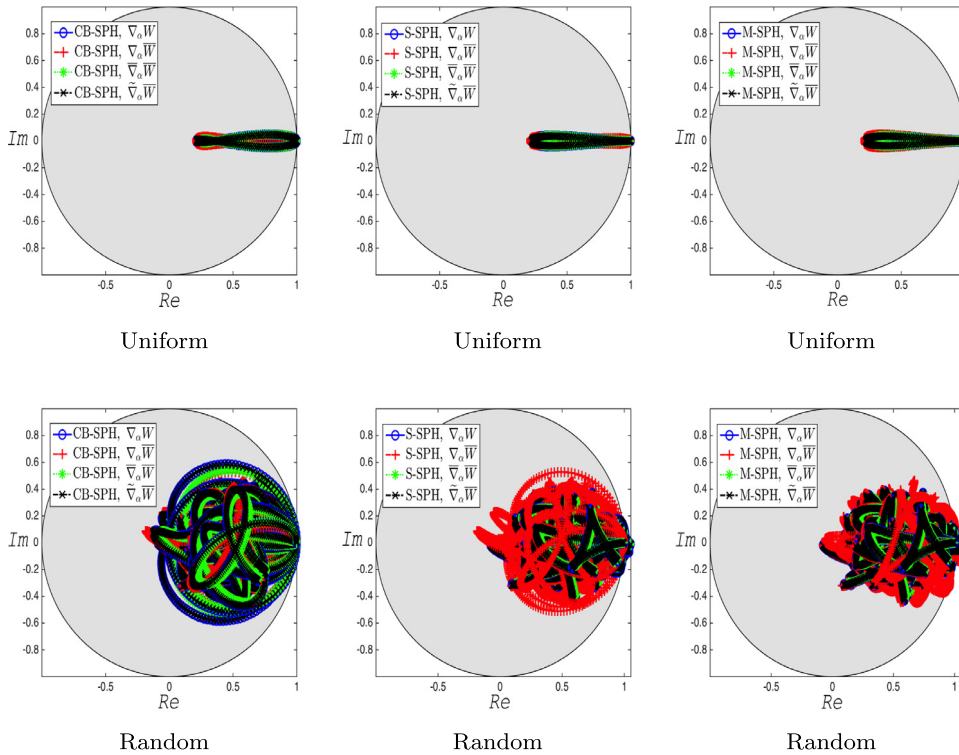
Fig. 5. von Neumann growth factor for different discretization schemes. Corrected Brookshaw's scheme (CB-SPH) is given by (51) with the correction multiplier, while Schwaiger's scheme (S-SPH) is given by (52)–(55). New approximation (M-SPH) considered here are the SPH form (69)–(71). Four different options of computing kernel gradients (i.e., $\nabla_\gamma W$ (blue color), $\nabla_\alpha \overline{W}$ (red color), $\overline{\nabla}_\alpha \overline{W}$ (green color), and $\widetilde{\nabla}_\alpha \overline{W}$ (black color)) with corresponding corrected kernel gradients are shown. (For interpretation of the references to color in this figure legend, the reader is referred to the web version of this article.)

leads to the expression for the von Neumann growth factor subject to (81) and linear Laplace operator:

$$\lambda_j(\tau) = 1 + \tau \cdot e^{-\mathbf{i}\mathbf{k}_j \cdot \mathbf{r}_j} \cdot \mathbf{L}^{\bar{h}}\left[\left\{e^{\mathbf{i}\mathbf{k}\cdot\mathbf{r}}\right\}\right], \quad \mathbf{r} \in \mathbb{R}^n, \ n = 1, 2, 3; \tag{83}$$

where $\left\{e^{\mathbf{i}\mathbf{k}\cdot\mathbf{r}}\right\} = \left(e^{\mathbf{i}\mathbf{k}_1 \cdot \mathbf{r}_1}, \dots, e^{\mathbf{i}\mathbf{k}_N \cdot \mathbf{r}_N}\right)$ and $\lambda_j(\tau)$ is the von Neumann growth factor. For the discretization to be stable, it is required that $\left|\lambda_j(\tau)\right| \leq 1, \ \forall j$. The von Neumann growth factor is shown for three main discretization schemes: Corrected Brookshaw's scheme (CB-SPH) (51), Schwaiger's scheme (S-SPH) (52)–(55) and new approximation (M-SPH) (69)–(71) for uniform and pseudo random particle distribution with $\tau = 0.25$ and $\mathbf{M}^{\alpha\beta}(\mathbf{r}) = \delta_{\alpha\beta}$ (see, Fig. 5). In case of uniform particle distribution, the von Neumann growth factor clusters around the real axis for all schemes and satisfies the requirement $\left|\lambda_j(\tau)\right| \leq 1, \ \forall j$. In case of pseudo random particle distribution, the von Neumann growth factor has both real and imaginary parts forming complex shape but satisfying the requirement $\left|\lambda_j(\tau)\right| \leq 1, \ \forall j$ almost everywhere (i.e., it could be some problems at the boundary particles).

4.4. Numerical stability analysis

The results of von Neumann stability analysis are validated using the following 2D numerical example considering a laminar flow of an incompressible ($\partial v_x / \partial x + \partial v_y / \partial y = 0$) Newtonian fluid through a parallel plate slit. The governing equations in this case are given by:

$$\frac{\partial v_x}{\partial t} = -\frac{\partial w}{\partial x} + \frac{1}{Re}\left(\frac{\partial^2 v_x}{\partial x^2} + \frac{\partial^2 v_x}{\partial y^2}\right), \qquad \frac{\partial v_y}{\partial t} = -\frac{\partial w}{\partial y} + \frac{1}{Re}\left(\frac{\partial^2 v_y}{\partial x^2} + \frac{\partial^2 v_y}{\partial y^2}\right), \tag{84}$$

where $w = p/\rho_0$ is the specific (per unit mass) thermodynamic work, ρ_0 is the density, and t is the time, v_x and v_y are the velocity in the x-longitudinal and y-transverse directions of a parallel plate slit, p is the pressure. Eq. (84) is written in dimensionless form. The dimensionless Reynolds number is defined as $Re = (U \cdot L \cdot \rho)/\mu$, where U is the characteristic velocity, L is the characteristic length, and μ is the dynamic viscosity of the fluid.

Table 1

The error $\log_{10} E^n$ decay for the explicit method applied to a laminar flow of an incompressible Newtonian fluid through a parallel plate slit (84) using the New Scheme (69)–(71), where $\nu = \dfrac{\Delta t}{(Re \cdot \tilde{h}_{I,m}^2)}$.

Time	$\nu = 0.1$	$\nu = 0.2$	$\nu = 0.25$	$\nu = 0.26$
1	−3.790	−4.099	−3.699	−3.608
2	−4.825	−5.137	−4.738	−3.296
3	−5.894	−6.206	−5.807	−2.098
4	−6.965	−7.277	−6.878	−0.900
5	−8.037	−8.349	−7.950	0.298
6	−9.108	−9.420	−9.021	1.496
7	−10.180	−10.491	−10.092	2.693
8	−11.256	−11.554	−11.161	3.891
9	−12.379	−12.539	−12.195	5.089
10	−12.975	−13.019	−12.922	6.287

We consider a square of 2 by 2 in $\mathbb{R}^2$. The homogeneous particle distribution is used to discretize the computational domain. The initial and boundary conditions for $\mathbf{v} = \{v_x, v_y\}$ required to solve (84) are given by:

$$\begin{aligned} \mathbf{v}(t, x = 0) = \mathbf{v}^* \quad &\text{and} \quad \mathbf{v}(t, x = 2) = \mathbf{v}^{**}; \\ \mathbf{v}(t = 0) = 0 \quad &\text{and} \quad \mathbf{v}(t, y = \pm 1) = 0; \end{aligned} \tag{85}$$

where $\mathbf{v}^*$ and $\mathbf{v}^{**}$ are prescribed velocities as some functions of time. The specific thermodynamic work is defined up to a constant.

We consider flow through a truncated section of a pipe with prescribed specific (per unit mass) thermodynamic work $\Delta w/L$ gradient governed by:

$$\frac{\partial v_x}{\partial t} = -\frac{\Delta w}{L} + \frac{1}{Re} \frac{\partial^2 v_x}{\partial y^2}, \quad v_y = 0. \tag{86}$$

The solution to (86) subject to the conditions in (85) and infinite in the longitudinal direction pipe yields to the following analytical velocity profile:

$$v_x^a = \frac{Re\Delta w}{L} \left[\frac{1}{2}\left(1 - y^2\right) - \right.$$

$$\left. \frac{16}{\pi^3} \sum_{n=0}^{\infty} \frac{(-1)^n}{(2n+1)^3} \cos\left(\frac{(2n+1)\pi y}{2}\right) e^{-\left(\frac{2n+1}{2}\pi\right)^2 \frac{t}{Re}} \right]. \tag{87}$$

where $\Delta w/L$ is the imposed gradient of the specific thermodynamic work and $w(x = 0) = w_1$, $w(x = 2) = w_2$, $\Delta w = w_2 - w_1$. We will use this v_x^a profile to set up the boundary conditions for inlet and outlet particles velocity, which are placed at the boundary of the computational domain.

The temporal discretization is as follows

$$\frac{v_x^{n+1} - v_x^n}{\Delta t} = -\frac{\Delta w}{L} + \frac{1}{Re}\mathbf{L}\left(v_x^n\right), \qquad \frac{v_y^{n+1} - v_y^n}{\Delta t} = \frac{1}{Re}\mathbf{L}\left(v_y^n\right), \tag{88}$$

where $\mathbf{v}^{n+1} = \{v_x^{n+1}, v_y^{n+1}\}$ and $\mathbf{v}^n = \{v_x^n, v_y^n\}$ are the divergence-free velocities at time $n+1$ and n, respectively and $\mathbf{L}()$ is the meshless discretization of the Laplace operator using M-SPH method. We introduce the maximum error at time step n as follows:

$$E^n = \max\{|[v_x^n]_J - [v_x^a]_J|, \ J = 1, \ldots, N\}, \tag{89}$$

where J is the particle index and N is the number of particles. As a result, the M-SPH spatial discretization is able to correctly simulate flow in a parallel plate slit. As an example, Table 1 shows the error $\log_{10} E^n$ decay for the explicit method (88) during the numerical simulation obtained using the M-SPH method (69)–(71) and different characteristic diffusivity $\left(Re \cdot \tilde{h}_{I,m}^2\right)/\Delta t$ with $Re = 1$, $\Delta w/L = 1$. The error curve is interpolated by using cubic splines to obtain values at the selected times presented in Table 1. From the previous section, it follows that the stability requirement is met for $\nu \le 0.25$. Table 1 shows that the solution is stable under this condition and has smaller error around $\nu = 0.2$ approaching steady-state solution in the optimum way. The solution is strictly speaking unstable for $\nu > 0.25$ and as it shown in the last column of Table 1.

4.5. Monotonicity and convergence

In real life applications, the numerical domains are large and, therefore, many degree of freedom (i.e., unknowns) is required. The resulting matrix is usually sparse, but because of fill-in a direct method requires significant amount of

memory and time in general case. Hence, iterative solvers are used to overcome these issues. The iterative solvers converge only if the matrix satisfies certain properties related to the property of the diagonal dominance. However, these properties are only sufficient conditions for the method to converge.

The proof of the convergence of linear meshless schemes applied to a linear elliptic boundary value problem can be done in the following steps (see, Bouchon (2007) [81], Bouchon and Peichl (2007) [82], Matsunaga and Yamamoto (2000) [83], Thomée (2001) [84]: if it is shown that the truncation error ε tends to 0 as the maximum smoothing length $\bar{h}_{max} = \max_{I \in N} \tilde{h}_I$ goes to 0, then the linear system $\mathbf{A}\delta u = \varepsilon$ that couples the variable error δu with ε proves the convergence of the schemes, given that the matrix of the discretized meshless operator is monotone.

Definition 7. A square matrix $\mathbf{A} = \left(a_{\alpha\beta}\right)_{1 \leq \alpha \leq n, 1 \leq \beta \leq n} \in \mathbb{R}^{n \times n}$ is called $\mathcal{M}$-matrix if $a_{\alpha\beta} \leq 0 \ \forall \alpha \neq \beta$, $a_{\{\alpha\alpha\}} > 0 \ \forall \alpha$ and $\mathbf{A}$ is strictly diagonally dominant matrix.

The $\mathcal{M}$-matrix is monotone since its inverse is positive, i.e. $\mathbf{A}^{-1} \geq 0$. Furthermore, the monotone schemes do satisfy a discrete maximum principle producing solutions without spurious oscillations.

It is clear that the new scheme (69)–(71) can be written in the form (66), where meshless transmissibility between particles $\mathbf{r}_J$ and $\mathbf{r}_I$ can be defined as $T\left(\mathbf{r}_J, \mathbf{r}_I\right) = \dfrac{\bar{\Gamma}_{\beta\beta}^{-1}}{n}\left(m_I + m_J\right)\bar{T}_{IJ}$ with:

$$\bar{T}_{IJ} = V_{\mathbf{r}_J}\left\{\frac{\left(\mathbf{r}_J - \mathbf{r}_I\right)\cdot\overline{\nabla W}\left(\mathbf{r}_J - \mathbf{r}_I, \tilde{h}_{IJ}\right)}{\left\|\mathbf{r}_J - \mathbf{r}_I\right\|^2} - \overline{\nabla_\alpha^* W}\left(\mathbf{r}_J - \mathbf{r}_I, \tilde{h}_{IJ}\right)\widetilde{\mathbf{N}}^\alpha\right\}, \tag{90}$$

where $\widetilde{\mathbf{N}}^\alpha\left(\mathbf{r}_I\right)$ is defined by (53). Applying the relation (19) valid for kernel gradients (15), (17), (18) and the definition of the corrected kernel gradient (23), (24) leading to

$$\bar{T}_{IJ} = \frac{V_{\mathbf{r}_J}}{\tilde{h}_{IJ}\left\|\mathbf{r}_J - \mathbf{r}_I\right\|}G(z_J, \mathbf{r}_I)\left[1 - \widetilde{\mathbf{N}}^\alpha\left(\mathbf{r}_I\right)\mathbf{C}_{\alpha\beta}\left(\mathbf{r}_I\right)\left(\mathbf{r}_J^\beta - \mathbf{r}_I^\beta\right)\right]. \tag{91}$$

The sign of the transmissibility coefficient is described by the following Lemma.

Lemma 3. *If matrix $\bar{\Gamma}_{ij}\left(\mathbf{r}_I\right)$ is strictly diagonally dominant matrix then the coefficients $T\left(\mathbf{r}_J, \mathbf{r}_I\right)$ are positive in the following cases $\forall \mathbf{r}_I$:*
(a) Case $\Gamma_{\alpha\beta}^*\left(\mathbf{r}_I\right) \neq 0$: if we have the following relation $\forall \mathbf{r}_J, \mathbf{r}_K \in \Omega_{\mathbf{r}_I, \tilde{h}_I}$

$$sgn\left[1 - \widetilde{\mathbf{N}}\left(\mathbf{r}_I\right)\mathbf{C}\left(\mathbf{r}_I\right)\left(\mathbf{r}_J - \mathbf{r}_I\right)\right] = sgn\left[1 - \widetilde{\mathbf{N}}\left(\mathbf{r}_I\right)\mathbf{C}\left(\mathbf{r}_I\right)\left(\mathbf{r}_K - \mathbf{r}_I\right)\right], \tag{92}$$

where sgn is the sign function.
(b) Case $\Gamma_{\alpha\beta}^*\left(\mathbf{r}_I\right) = 0$: if we have the following relation $\forall \mathbf{r}_J \in \Omega_{\mathbf{r}_I, \tilde{h}_I}$

$$\left[1 - \widetilde{\mathbf{N}}\left(\mathbf{r}_I\right)\mathbf{C}\left(\mathbf{r}_I\right)\left(\mathbf{r}_J - \mathbf{r}_I\right)\right] > 0. \tag{93}$$

Proof. Taking into account (72), (73), (74) and Lemma 2, we need to ensure that $\bar{\Gamma}_{\beta\beta}^{-1}/n$ and $\bar{T}_{IJ}$ are of the same sign. This can be achieved by the conditions of Lemma 3 since both $\bar{\Gamma}_{\beta\beta}^{-1}/n$ and $\bar{T}_{IJ}$ have the same sign subject to the conditions of Lemmas 2 and 3. □

It is clear that the sufficient conditions (92) and (93) are fulfilled for the homogeneous and symmetrical particles distribution due to $\widetilde{\mathbf{N}}\left(\mathbf{r}_I\right) = 0$. In general, one can note that

$$\widetilde{\mathbf{N}}\left(\mathbf{r}_I\right)\mathbf{C}\left(\mathbf{r}_I\right)\left(\mathbf{r}_K - \mathbf{r}_I\right) = \left\|\boldsymbol{\xi}_I\right\|\left\|\Delta\mathbf{r}_{JI}\right\| \cdot \cos(\boldsymbol{\xi}_I, \Delta\mathbf{r}_{JI}), \tag{94}$$

where $\boldsymbol{\xi}_I^\beta$ is the vector $\widetilde{\mathbf{N}}^\alpha\left(\mathbf{r}_I\right)\mathbf{C}\left(\mathbf{r}_I\right)_{\alpha\beta}$, $\Delta\mathbf{r}_{JI}$ is the vector $\left(\mathbf{r}_J - \mathbf{r}_I\right)$, $\cos(\boldsymbol{\xi}_I, \Delta\mathbf{r}_{JI})$ is the *cos* of angle between $\boldsymbol{\xi}_I^\beta$ and $\Delta\mathbf{r}_{JI}$. The maximum of absolute values in (94) is achieved when vectors $\boldsymbol{\xi}_I^\beta$ and $\Delta\mathbf{r}_{JI}$ are collinear. Fig. 6 shows the mean value distribution of $\left\|\boldsymbol{\xi}_I\right\|$ and its dispersion as a function of neighboring particles in a unit circle. The smoothing length for all particles $\tilde{h}_I = 1 \ \forall I$ and $f = 0.5005$ are assumed. The 50 random configurations of the neighboring particles distribution are considered starting from 4 to 500 neighboring particles in 2D. It is clear from Fig. 6 that sufficient conditions (92) and (93) are fulfilled in statistical sense for heterogeneous particles distribution for large number of neighboring particles. A consequence of Lemma 3 is the statement of the next Theorem.

Theorem 4. *The proposed discretization scheme (69)–(71) subject to the conditions of Lemma 3 is monotone for the medium with the scalar heterogeneous $-m\left(\mathbf{r}\right)$ coefficients.*

Lemma 3 provides sufficient (not necessary) conditions for the monotonicity of the proposed new discretization scheme (69)–(71).
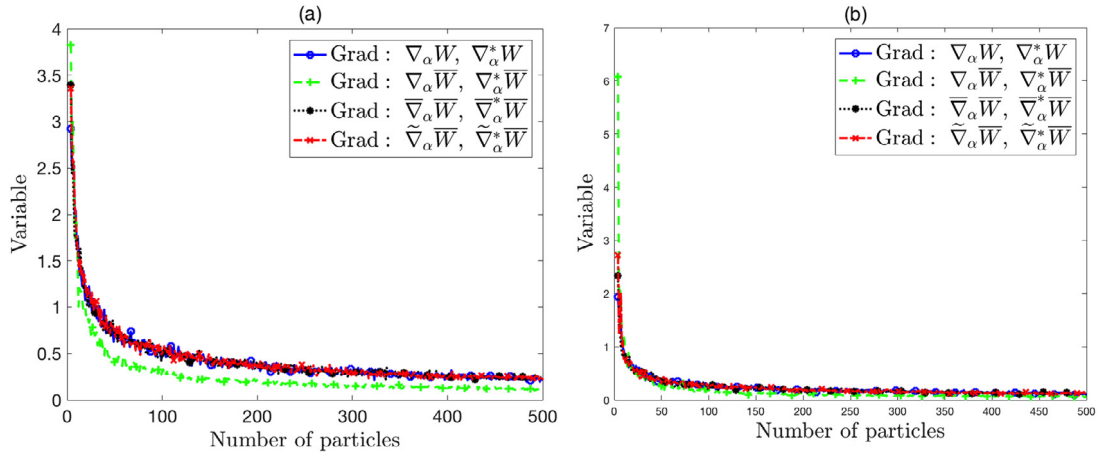
Fig. 6. (a) The mean value distribution of $\|\boldsymbol{\xi}_I\|$ for 50 random configurations; (b) The dispersion $\sigma\left(\|\boldsymbol{\xi}_I\|\right)$ of the $\|\boldsymbol{\xi}_I\|$ distribution for 50 random configurations .

5. Solution of boundary value problems

Following the work by [50], the numerical tests for inhomogeneous Dirichlet, Neumann and mixed boundary conditions are considered for homogeneous and heterogeneous media with the characteristics $\mathbf{M}(\boldsymbol{r})$. To illustrate the performance of the proposed scheme, a modeling of a single phase steady-state fluid flow in fully anisotropic porous media with different type of boundary conditions is also presented in this section. The square 2D and 3D domains (3) are considered.

The relative error used to quantify the accuracy of the proposed schemes in the subsections 2.3, 2.4, and 3.1 during numerical simulation in this section is given by:

$$\|E_R\|_{\Omega}^{L_2} = \left[\frac{1}{\sum_{\boldsymbol{r}_J \in \Omega} V_{\boldsymbol{r}_J}} \sum_{\boldsymbol{r}_K \in \Omega} V_{\boldsymbol{r}_K} \left(\frac{\mathbf{u}(\boldsymbol{r}_K) - \langle \mathbf{u}(\boldsymbol{r}_K)\rangle}{\mathbf{u}(\boldsymbol{r}_K)}\right)^2\right]^{1/2} \tag{95}$$

where $\mathbf{u}(\boldsymbol{r})$ is the analytical or reference solution field and $\langle \mathbf{u}(\boldsymbol{r}_K)\rangle$ is the approximated solution field. Several numerical results using considered in this paper schemes for uniform and pseudo random particle distributions are shown in the following sections that confirm the theoretical results from the previous sections.

5.1. Inhomogeneous boundary condition

Firstly, the homogeneous properties of the porous media $\mathbf{M}(\boldsymbol{r}) = \mathbf{I}$ are assumed for simplicity of the derivation. The analytical solution of (1) subject to the assumption that $g(\boldsymbol{r}) \equiv 0$ for $\boldsymbol{r} \in \Omega \subset \mathbb{R}^2$ and constant boundary conditions is the following:

$$\begin{aligned}
\mathbf{u}(x, y) = &\sum_{n=odd}\left[\frac{4\psi_1}{n\pi \sinh\left(\frac{n\pi H}{L}\right)}\right]\sin\left(\frac{n\pi}{L}x\right)\sinh\left(\frac{n\pi}{L}(H-y)\right) + \\
&+ \sum_{n=odd}\left[\frac{4\psi_2}{n\pi \sinh\left(\frac{n\pi L}{H}\right)}\right]\sin\left(\frac{n\pi}{H}y\right)\sinh\left(\frac{n\pi}{H}x\right) + \\
&+ \sum_{n=odd}\left[\frac{4\psi_3}{n\pi \sinh\left(\frac{n\pi L}{H}\right)}\right]\sin\left(\frac{n\pi}{H}y\right)\sinh\left(\frac{n\pi}{H}x\right) + \\
&+ \sum_{n=odd}\left[\frac{4\psi_4}{n\pi \sinh\left(\frac{n\pi L}{H}\right)}\right]\sin\left(\frac{n\pi}{H}y\right)\sinh\left(\frac{n\pi}{H}(L-x)\right),
\end{aligned} \tag{96}$$

where ψ_1 is the boundary at $y = 0$, ψ_2 at $x = L$, ψ_3 at $y = H$, and ψ_4 at $x = 0$.

Tables 2, 3 show the convergence rate of different schemes for uniform particle distribution for different number of degrees of freedom (DoF). The solutions with MPFA and Mimetic schemes were obtained using MATLAB Reservoir Simulation Toolbox (MRST) [85]. It is clear from the convergence results that schemes (52)–(55) and (69)–(71) are identical and they over perform the scheme (51). This is due to the fact that a regular grid of particles does not activate the

Table 2
The error of convergence for different schemes (uniform particle distribution) and $f = 0.5005$.

DoF	MPFA	Mimetic	Brookshaw (51)	Schwaiger (52)–(55)	New Scheme (69)–(71)
25	$1.318 \cdot 10^{-1}$	$1.240 \cdot 10^{-1}$	$1.314 \cdot 10^{0}$	$6.608 \cdot 10^{-2}$	$6.608 \cdot 10^{-2}$
100	$3.296 \cdot 10^{-2}$	$3.078 \cdot 10^{-2}$	$3.925 \cdot 10^{-1}$	$1.865 \cdot 10^{-2}$	$1.865 \cdot 10^{-2}$
400	$8.233 \cdot 10^{-3}$	$7.685 \cdot 10^{-3}$	$1.105 \cdot 10^{-1}$	$4.714 \cdot 10^{-3}$	$4.714 \cdot 10^{-3}$
1600	$2.058 \cdot 10^{-3}$	$1.920 \cdot 10^{-3}$	$3.025 \cdot 10^{-2}$	$1.179 \cdot 10^{-3}$	$1.179 \cdot 10^{-3}$
6400	$5.318 \cdot 10^{-4}$	$4.968 \cdot 10^{-4}$	$8.152 \cdot 10^{-3}$	$3.213 \cdot 10^{-4}$	$3.213 \cdot 10^{-4}$
25600	$3.007 \cdot 10^{-4}$	$2.955 \cdot 10^{-4}$	$2.193 \cdot 10^{-3}$	$2.807 \cdot 10^{-4}$	$2.807 \cdot 10^{-4}$

Table 3
The error of convergence for different schemes (uniformed particle distribution) and $f = 1.001$.

DoF	Brookshaw (51)	Schwaiger (52)–(55)	New Scheme (69)–(71)
25	$2.312 \cdot 10^{-1}$	$1.091 \cdot 10^{-1}$	$1.091 \cdot 10^{-1}$
100	$1.120 \cdot 10^{-1}$	$2.698 \cdot 10^{-2}$	$2.698 \cdot 10^{-2}$
400	$3.998 \cdot 10^{-2}$	$6.737 \cdot 10^{-3}$	$6.737 \cdot 10^{-3}$
1600	$1.262 \cdot 10^{-2}$	$1.684 \cdot 10^{-3}$	$1.684 \cdot 10^{-3}$
6400	$3.737 \cdot 10^{-3}$	$4.418 \cdot 10^{-4}$	$4.418 \cdot 10^{-4}$
25600	$1.097 \cdot 10^{-3}$	$2.919 \cdot 10^{-4}$	$2.919 \cdot 10^{-4}$

Table 4
The error of convergence for different schemes (random particle distribution) and $f = 0.6006$.

DoF	Brookshaw (51)	Schwaiger (52)–(55)	New Scheme (69)–(71)
25	$1.102 \cdot 10^{+0} \pm 1.966 \cdot 10^{-2}$	$1.940 \cdot 10^{-1} \pm 3.954 \cdot 10^{-2}$	$3.707 \cdot 10^{-1} \pm 1.319 \cdot 10^{-1}$
100	$3.361 \cdot 10^{-1} \pm 4.923 \cdot 10^{-3}$	$5.511 \cdot 10^{-2} \pm 1.205 \cdot 10^{-2}$	$9.074 \cdot 10^{-2} \pm 2.668 \cdot 10^{-2}$
400	$9.576 \cdot 10^{-2} \pm 8.705 \cdot 10^{-4}$	$1.376 \cdot 10^{-2} \pm 2.440 \cdot 10^{-3}$	$2.299 \cdot 10^{-2} \pm 6.972 \cdot 10^{-3}$
1600	$2.640 \cdot 10^{-2} \pm 2.551 \cdot 10^{-4}$	$4.157 \cdot 10^{-3} \pm 7.485 \cdot 10^{-4}$	$5.912 \cdot 10^{-3} \pm 1.289 \cdot 10^{-3}$
6400	$7.185 \cdot 10^{-3} \pm 5.982 \cdot 10^{-5}$	$1.044 \cdot 10^{-3} \pm 1.465 \cdot 10^{-4}$	$1.406 \cdot 10^{-3} \pm 3.090 \cdot 10^{-4}$
25600	$1.944 \cdot 10^{-3} \pm 1.451 \cdot 10^{-5}$	$3.858 \cdot 10^{-4} \pm 5.887 \cdot 10^{-5}$	$4.960 \cdot 10^{-4} \pm 8.425 \cdot 10^{-5}$

Table 5
The error of convergence for different schemes (random particle distribution) and $f = 1.2012$.

DoF	Brookshaw (51)	Schwaiger (52)–(55)	New Scheme (69)–(71)
25	$3.578 \cdot 10^{-1} \pm 2.879 \cdot 10^{-2}$	$2.162 \cdot 10^{-1} \pm 2.800 \cdot 10^{-2}$	$1.842 \cdot 10^{-1} \pm 8.871 \cdot 10^{-3}$
100	$1.261 \cdot 10^{-1} \pm 4.859 \cdot 10^{-3}$	$5.696 \cdot 10^{-2} \pm 5.518 \cdot 10^{-3}$	$4.596 \cdot 10^{-2} \pm 1.999 \cdot 10^{-3}$
400	$4.224 \cdot 10^{-2} \pm 1.092 \cdot 10^{-3}$	$1.493 \cdot 10^{-2} \pm 1.546 \cdot 10^{-3}$	$1.157 \cdot 10^{-2} \pm 5.691 \cdot 10^{-4}$
1600	$1.299 \cdot 10^{-2} \pm 2.031 \cdot 10^{-4}$	$3.934 \cdot 10^{-3} \pm 3.969 \cdot 10^{-4}$	$2.889 \cdot 10^{-3} \pm 1.451 \cdot 10^{-4}$
6400	$3.862 \cdot 10^{-3} \pm 3.452 \cdot 10^{-5}$	$1.037 \cdot 10^{-3} \pm 8.443 \cdot 10^{-5}$	$7.507 \cdot 10^{-4} \pm 4.060 \cdot 10^{-5}$
25600	$1.133 \cdot 10^{-3} \pm 2.125 \cdot 10^{-5}$	$4.087 \cdot 10^{-4} \pm 5.405 \cdot 10^{-5}$	$3.475 \cdot 10^{-4} \pm 3.814 \cdot 10^{-5}$

additional correction terms at both schemes and only leads to the same correction factor $\bar{\boldsymbol{\Gamma}}_{\beta\beta}^{-1} = \boldsymbol{\Gamma}_{\beta\beta}^{-1}$. This case was computed and is shown to verify that M-SPH (69)–(71) reduces to S-SPH (52)–(55) in this special case, but that once the disorder starts, M-SPH out-performs S-SPH in some cases as it is shown below.

The convergence rate as was predicted theoretically is at least $\mathcal{O}\left(h^{\omega}\right)$, $1 \leq \omega \leq 2$. Tables 4, 5 shows the convergence rate for different schemes and pseudo random distribution. The reason for starting from $f = 0.5005$ is that we want to force the same number of non-zero entries in the matrix as for MPFA or Memetic methods. This procedure may lead to a badly conditioned matrix since $\left\|\overline{\nabla W}\left(\boldsymbol{r}_J - \boldsymbol{r}_I, h\right)\right\| \ll 1$. This distribution of particles was generated by perturbing the regularly distributed particles using a uniform random variable varying between $+10\%$ and -10% of the maximum smoothing length $\tilde{h}_{max} = 1.001$. Since random realizations are used to compute errors, the statistical data about 30 realizations are used to compute mean values and standard deviations. This data is presented in Tables 4, Table 5. The positive trends of the scheme remain the same as for the case of uniform particle distributions. The scheme (51) has higher error compare to schemes (52)–(55) and (69)–(71). However, the dispersion of the approximation error is higher in the scheme (69)–(71). Fig. 7 shows the numerical solution of the boundary value problem obtained using different discretization methods. The solution was obtained using 40 particles/cells in each direction.

It is important to stress that the new scheme is not always outperforming Schwaiger scheme (52)–(55) for random particle distribution. In Table 5 the new scheme shows higher accuracy, compared with Schwaiger scheme. In order to gain insight into the error distribution, we should notice from 1D analysis that leading term of the correction $\mathbf{U}_{\omega\beta\alpha}^{*} \cdot \mathbf{N}^{\omega}$ term of tensor $\boldsymbol{\Gamma}_{\alpha\beta}$ has the following asymptotic:

$$|\mathbf{N}\left(x_I\right)\mathbf{U}\left(x_I\right)| \sim \mathcal{O}\left(\bar{\delta}^4 \Delta \bar{z}^6\right) + \mathcal{O}\left(h^4\right) \tag{97}$$
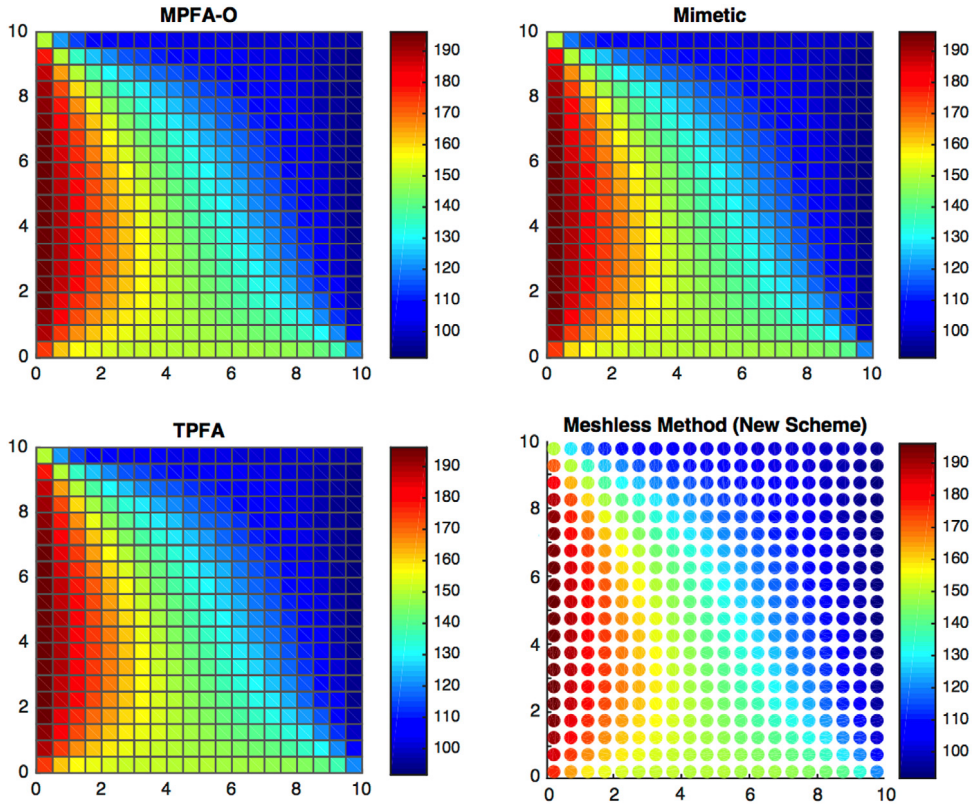
Fig. 7. Comparison of solutions of the Dirichlet problem for the Laplace equation. The method used are MPFA-O, Mimetic, TPFA, and Meshless methods (New Method: (69)–(71)).

and having independent of smoothing length term and, hence, should improve the accuracy if we take this into account while computing the correction factor. On the other hand, we cannot control the error introduced to the tensor $\mathbf{Q}_{\alpha\gamma}$ (essential to the magnitude of the error) defined by (47), which can be sometimes larger for new scheme.

5.2. Inhomogeneous mixed boundary condition test

The general steady-state solution for a Dirichlet condition along the base of the plate and Neumann conditions elsewhere is given in [50] by

$$\mathbf{u}(x, y) = \psi_1 + \psi_3 y + \sum_{n=1}^{\infty} \frac{2\psi_2 \cosh(\lambda_n x) + 2\psi_4 \cosh(\lambda_n (L - x))}{H \lambda_n^2 \sinh(\lambda_n L)} \sinh(\lambda_n y), \tag{98}$$

where ψ_1 is the boundary value of $\mathbf{u}$ at $y = 0$, ψ_2 is the flux at $x = L$, ψ_3 is the flux at $y = H$, and ψ_4 is the flux at $x = 0$, and $\lambda_n = \dfrac{(2n - 1)\pi}{2H}$. The following parameters (dimensionless) were chosen: $\psi_1 = 150$, $\psi_3 = 150$, $\psi_4 = 200$, $\psi_2 = 90$. Again, for uniform and regular particles distribution, MPFA method reduces to the TPFA. Similar to the previous section, the regular and pseudo random particles distributions are considered to access the convergence properties of the proposed schemes.

Remark 4. Let $\Upsilon_N = \varnothing$ (Neumann boundary) and $\Upsilon_D = \varnothing$ (Dirichlet boundary), $\partial\Omega = \Upsilon_N \cup \Upsilon_D$ (where $\partial\Omega$ is the boundary of the domain Ω), $g(\mathbf{r}) \geq 0$, $\mathbf{r} \in \Omega$, $g_N(\mathbf{r}) \geq 0$, $\mathbf{r} \in \Upsilon_N$, $g_D(\mathbf{r}) \geq 0$, $\mathbf{r} \in \Upsilon_D$ and the solution of

$$\mathbf{L}(\mathbf{u}) = 0 \quad \text{or} \quad \nabla(\mathbf{M}(\mathbf{r})\nabla\mathbf{u}(\mathbf{r})) = g(\mathbf{r}), \quad \forall \mathbf{r} \in \Omega \subset \mathbb{R}^n, \tag{99}$$

exists then it can be discretized in all internal particles by the following schemes Brookshaw (51), Schwaiger (52)–(55), and New Scheme (69)–(71) and compounded with the following condition for all $\mathbf{r} \in \Upsilon_N$:

$$\langle v^\alpha \mathbf{n}_\alpha \rangle = \mathbf{n}_\alpha \mathbf{M}^{\alpha\beta}(\mathbf{r}) \sum_{\mathbf{r}_J \in \Omega_{\mathbf{r},\tilde{h}}} V_{\mathbf{r}_J} \left[\mathbf{u}(\mathbf{r}_J) - \mathbf{u}(\mathbf{r}_I) \right] \overline{\nabla_\beta^* W}(\mathbf{r}_J - \mathbf{r}_I, h) \tag{100}$$

Table 6
The error of convergence for different schemes (uniform particle distribution) and $f = 0.5005$.

DoF	MPFA	Mimetic	Brookshaw (51)	Schwaiger (52)–(55)	New Scheme (69)–(71)
25	$1.489 \cdot 10^{-1}$	$2.651 \cdot 10^{-2}$	$1.489 \cdot 10^{6}$	$8.244 \cdot 10^{-1}$	$8.244 \cdot 10^{-1}$
100	$2.015 \cdot 10^{-2}$	$4.424 \cdot 10^{-3}$	$9.471 \cdot 10^{5}$	$2.178 \cdot 10^{-1}$	$2.178 \cdot 10^{-1}$
400	$2.727 \cdot 10^{-3}$	$6.889 \cdot 10^{-4}$	$5.378 \cdot 10^{5}$	$5.550 \cdot 10^{-2}$	$5.550 \cdot 10^{-2}$
1600	$3.666 \cdot 10^{-4}$	$1.024 \cdot 10^{-4}$	$2.859 \cdot 10^{5}$	$1.398 \cdot 10^{-2}$	$1.398 \cdot 10^{-2}$
6400	$4.951 \cdot 10^{-5}$	$1.522 \cdot 10^{-5}$	$1.473 \cdot 10^{5}$	$3.504 \cdot 10^{-3}$	$3.504 \cdot 10^{-3}$
25600	$7.309 \cdot 10^{-6}$	$2.920 \cdot 10^{-6}$	$7.474 \cdot 10^{4}$	$8.770 \cdot 10^{-4}$	$8.770 \cdot 10^{-4}$

Table 7
The error of convergence for different schemes (uniform particle distribution) and $f = 1.001$.

DoF	Brookshaw (51)	Schwaiger (52)–(55)	New Scheme (69)–(71)
25	$1.163 \cdot 10^{0}$	$1.078 \cdot 10^{-1}$	$1.078 \cdot 10^{-1}$
100	$1.208 \cdot 10^{0}$	$1.488 \cdot 10^{-2}$	$1.488 \cdot 10^{-2}$
400	$8.291 \cdot 10^{-1}$	$2.244 \cdot 10^{-3}$	$2.244 \cdot 10^{-3}$
1600	$4.831 \cdot 10^{-1}$	$4.215 \cdot 10^{-4}$	$4.215 \cdot 10^{-4}$
6400	$2.606 \cdot 10^{-1}$	$9.858 \cdot 10^{-5}$	$9.858 \cdot 10^{-5}$
25600	$1.353 \cdot 10^{-1}$	$2.502 \cdot 10^{-5}$	$2.502 \cdot 10^{-5}$

Table 8
The error of convergence for different schemes (random particle distribution) and $f = 0.6006$.

DoF	Brookshaw (51)	Schwaiger (52)–(55)	New Scheme (69)–(71)
25	$5.608 \cdot 10^{1} \pm 1.019 \cdot 10^{0}$	$8.815 \cdot 10^{-1} \pm 4.248 \cdot 10^{-1}$	$1.242 \cdot 10^{0} \pm 5.058 \cdot 10^{-1}$
100	$3.769 \cdot 10^{1} \pm 5.708 \cdot 10^{-1}$	$3.454 \cdot 10^{-1} \pm 1.977 \cdot 10^{-1}$	$4.361 \cdot 10^{-1} \pm 2.425 \cdot 10^{-1}$
400	$2.154 \cdot 10^{1} \pm 1.757 \cdot 10^{-1}$	$8.454 \cdot 10^{-2} \pm 5.111 \cdot 10^{-2}$	$1.525 \cdot 10^{-1} \pm 1.195 \cdot 10^{-1}$
1600	$1.159 \cdot 10^{1} \pm 7.457 \cdot 10^{-2}$	$2.245 \cdot 10^{-2} \pm 1.055 \cdot 10^{-2}$	$4.563 \cdot 10^{-2} \pm 2.328 \cdot 10^{-2}$
6400	$6.027 \cdot 10^{0} \pm 2.312 \cdot 10^{-2}$	$1.104 \cdot 10^{-2} \pm 7.523 \cdot 10^{-3}$	$1.848 \cdot 10^{-2} \pm 9.276 \cdot 10^{-3}$
25600	$3.054 \cdot 10^{0} \pm 1.174 \cdot 10^{-2}$	$4.123 \cdot 10^{-3} \pm 2.059 \cdot 10^{-3}$	$5.879 \cdot 10^{-3} \pm 4.253 \cdot 10^{-3}$

Table 9
The error of convergence for different schemes (random particle distribution) and $f = 1.2012$.

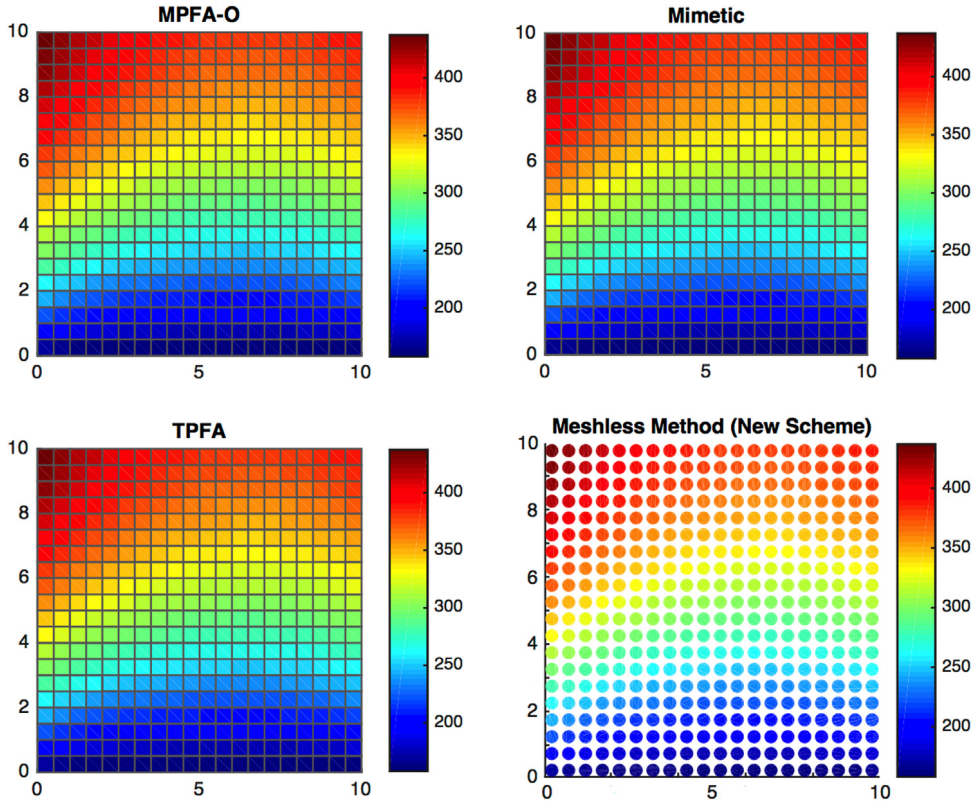| DoF	Brookshaw (51)	Schwaiger (52)–(55)	New Scheme (69)–(71)
25	$5.177 \cdot 10^{-1} \pm 7.312 \cdot 10^{-2}$	$3.143 \cdot 10^{-1} \pm 7.543 \cdot 10^{-2}$	$4.302 \cdot 10^{-1} \pm 1.461 \cdot 10^{-1}$
100	$5.160 \cdot 10^{-1} \pm 4.035 \cdot 10^{-2}$	$5.959 \cdot 10^{-2} \pm 4.713 \cdot 10^{-3}$	$1.106 \cdot 10^{-1} \pm 1.739 \cdot 10^{-2}$
400	$4.349 \cdot 10^{-1} \pm 1.715 \cdot 10^{-2}$	$1.515 \cdot 10^{-2} \pm 1.973 \cdot 10^{-3}$	$3.015 \cdot 10^{-2} \pm 1.045 \cdot 10^{-2}$
1600	$2.745 \cdot 10^{-1} \pm 9.059 \cdot 10^{-3}$	$3.926 \cdot 10^{-3} \pm 6.865 \cdot 10^{-4}$	$1.133 \cdot 10^{-2} \pm 5.486 \cdot 10^{-3}$
6400	$1.508 \cdot 10^{-1} \pm 2.822 \cdot 10^{-3}$	$1.595 \cdot 10^{-3} \pm 8.144 \cdot 10^{-4}$	$3.187 \cdot 10^{-3} \pm 1.438 \cdot 10^{-3}$
25600	$7.958 \cdot 10^{-2} \pm 1.146 \cdot 10^{-3}$	$5.354 \cdot 10^{-4} \pm 2.036 \cdot 10^{-4}$	$9.201 \cdot 10^{-4} \pm 5.201 \cdot 10^{-4}$

where $\boldsymbol{n}_\alpha$ are the component of the external normal to the boundary $\boldsymbol{r} \in \varUpsilon_N$.

The following smoothing multiplication factors $f = 0.5005$, $f = 1.001$, and $f = 2.002$ are considered. Tables 6, Table 7 show the convergence rate for different schemes using the uniform and pseudo random particle distribution. The convergence rate as was predicted theoretically is at least $\mathcal{O}(h^\omega)$, $1 \leq \omega < 2$. Interestingly, the scheme (51) shows a very bad convergence rate for $f = 0.5005$. This explains by the fact that we have one particle from each side in the kernel support almost next to the boundary of the kernel support leading to $\left\| \overline{\nabla W} \left(\boldsymbol{r}_J - \boldsymbol{r}_I, h\right) \right\| \ll 1$ and, hence, to a badly conditioned matrix. This cannot be observed for other schemes due to the normalization coefficient. As a result, the scheme (51) should be used with more than one particle in the compact support in each direction leading to a larger bandwidth in the matrix.

Tables 8, 9 show the convergence rate for different schemes with pseudo random particle distribution. The pseudo random distribution of particles was again generated by perturbing the regularly distributed particles using the uniform random variable varying between $+10\%$ and -10% of the maximum smoothing length $\tilde{h}_{max} = 1.001$. Similar to the above case, the statistical data about 30 realizations are used to compute mean values and standard deviations. These data are presented in Tables 8, 9. The general trends of the scheme prosperities remain the same as for uniform particle distributions. The scheme (51) has higher error compared to schemes (52)–(55) and (69)–(71). However, the dispersion of the approximation error is higher in the scheme (69)–(71). Results of the numerical solutions are shown in Fig. 8.

Remark 5. The solution of boundary value problems with inhomogeneous Dirichlet only and mixed boundary conditions shows that new scheme has identical accuracy with Schwaiger (2008) scheme (52)–(55) for uniform particle distribution as expected theoretically due to

$$\widetilde{\mathbf{N}}^\alpha = \mathbf{N}^\alpha = 0 \quad \forall \alpha; \qquad \bar{\boldsymbol{\Gamma}}_{\alpha\beta} = \boldsymbol{\Gamma}^*_{\alpha\beta} = \boldsymbol{\Gamma}_{\alpha\beta} \quad \forall \alpha, \beta.$$

Fig. 8. Comparison of solutions of the inhomogeneous mixed boundary problems for the Laplace equations. The methods used are MPFA-O, Mimetic, TPFA, and Meshless methods (New Method: (69)–(71)).

and a regular grid of particles does not activate the additional correction terms in both schemes. However, for random particle distributions subject to the $\overline{\nabla_\gamma W}\left(\boldsymbol{r}_J - \boldsymbol{r}_I, \tilde{h}_{IJ}\right)$ described by (15), (17) and (18), we have

$$\widetilde{\mathbf{N}}^\alpha = \mathbf{N}^\alpha \neq 0 \quad \forall \alpha; \qquad \bar{\boldsymbol{\varGamma}}_{\alpha\beta} \neq \boldsymbol{\varGamma}^*_{\alpha\beta} \neq \boldsymbol{\varGamma}_{\alpha\beta} \quad \forall \alpha, \beta.$$

Finally, we must stress that advantages of the new scheme are related to desirable properties (i.e., satisfying the two-point flux approximation nature in the form (2), stability and proven monotonicity but not the accuracy which has the same order as Schwaiger (2008) scheme (52)–(55) in general and better in some cases. Furthermore, desirable properties of the new scheme will allow to apply upwinding strategy during the solution of nonlinear PDEs.

5.3. SPE10

In addition, we investigate the accuracy of the numerical schemes using a well-known SPE10 benchmark [86] with the Laplace equation:

$$\mathbf{L}(\mathbf{u}) = -\nabla(\mathbf{M}(\boldsymbol{r})\nabla\mathbf{u}(\boldsymbol{r})) = 0, \ \forall \boldsymbol{r} \in \Omega \subset \mathbb{R}^n,$$

$$\mathbf{M}^{\alpha\beta}(\boldsymbol{r}) = K^{\alpha\beta}(\boldsymbol{r}), \ K^{\alpha\beta}(\boldsymbol{r}) = 0 \quad \forall \alpha \neq \beta; \ \alpha, \beta = 1, \ldots, n;$$

(101)

where $\mathbf{u}(\boldsymbol{r})$ is the unknown pressure field, $K^{\alpha\beta}(\boldsymbol{r})$ is the diagonal permeability field. The original model contains 85 layers, where layers from 1 to 35 have smooth permeability with lognormal distribution and layers 36 to 85 have channelized formations that are considered to be significantly more challenging for numerical simulations. The subset of this model is defined by the global Cartesian indices I, J, K. The 85 layer was used as a permeability field for 2D simulation with Cartesian indices $I = 1 : 60$ and $J = 1 : 60$. In 3D, the subsection Cartesian indices $I = 1 : 60, J = 1 : 60$, and $K = 1 : 60$. The permeability fields K^{11} for both cases are shown in Fig. 9. The boundary conditions correspond to the unit pressure drop over the entire domain in J-direction (i.e., $y_{min} = 0$ and $y_{max} = 1$). The numerical results using new scheme for the SPE10 cases are presented in Fig. 10. The relative error distribution is also shown for 2D and 3D cases, where the error is computed using (95) and numerical solution based on TPFA. Figs. 11 and 12 compare the convergence rates of the various discretizations subject to different preconditioners. Furthermore, if we notice the convergence comparison for this test in
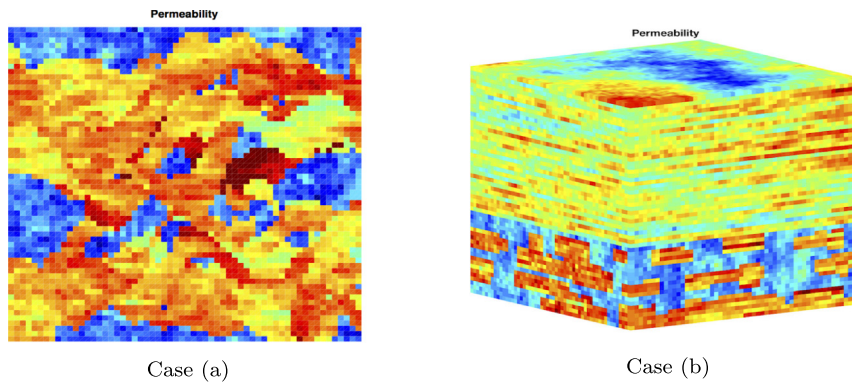
Fig. 9. The lognormal permeability field in the SPE10 benchmark test. Case (a) 60 × 60cells of 85 layer. Case (b) subsection of the SPE10 model defined by 60 × 60 × 60 cells.
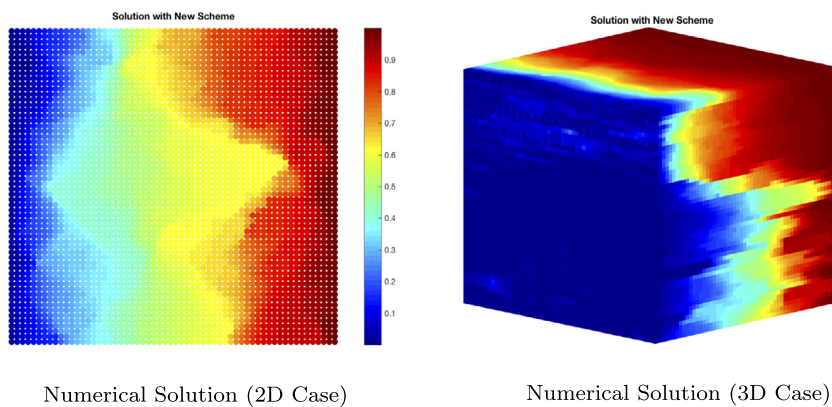

Fig. 10. Numerical solution obtained with the new scheme for the SPE10 cases. The solution is compared with the numerical solution based on TPFA. The maximum of the relative error (95) was 0.06% and 0.3% was obtained in 2D and 3D, respectively.
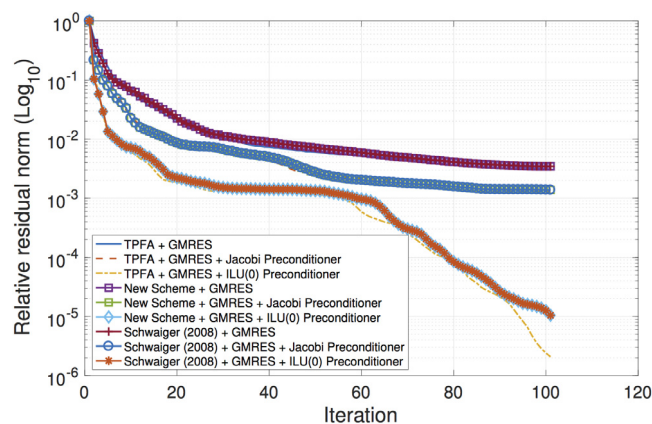
Fig. 11. Comparison of the convergence rate of the GMRES iterative method with and without preconditioner for different numerical discretization methods (TPFA, New Scheme (69)–(71), Schwaiger (52)–(55)). The linear system of equations is built using 2D case.

Figs. 11 and 12, the proposed new method offers similar convergence as compared to the Schwaiger's scheme (52)–(55). The reason for such convergence is the similarity between condition numbers of the linear system of equations resulting from these methods.
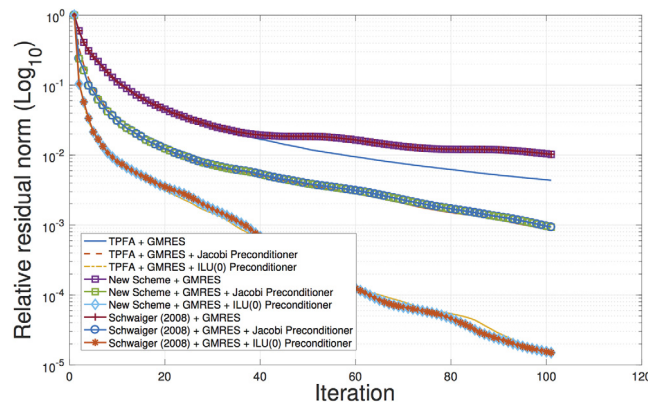
Fig. 12. Comparison of the convergence rate of the GMRES iterative method with and without preconditioner for different numerical discretization methods (TPFA, New Scheme (69)–(71), Schwaiger (52)–(55)). The linear system of equations is built using 3D case.

Another interesting observation in this numerical test is the small values of the relative error between the TPFA solution and proposed new method for both 2D and 3D cases. This observation exhibits the efficiency of the proposed meshless discretization scheme, which explains the higher accuracy of linear reproduction.

6. Conclusion

In this paper, the new stable SPH discretization of the elliptic operator for heterogeneous media is proposed. The scheme has the two-point flux approximation nature and can be written in the form of (2). Using this structure, it was possible to make some theoretical monotonicity analysis, which is difficult to perform for other schemes (e.g., Schwaiger's method). The paper also discusses the monotonicity and convergence properties of the new proposed scheme. The sufficient monotonicity condition is also formulated leading to the constraint on the kernel shape and particles distribution (see, Lemma 3 and Theorem 4). Furthermore, it follows from the Taylor's series analysis that proposed scheme is the optimum (i.e., high order with monotonicity property) one in this class (2) for a diagonal matrix of the operator coefficients. In addition, the proposed scheme allows to apply upwinding strategy during the solution of nonlinear PDEs.

The new scheme is based on a gradient approximation commonly used in thermal, viscous, and pressure projection problems and can be extended to include higher-order terms in the appropriate Taylor series. The proposed new scheme is combined with mixed corrections which ensure linear completeness. The mixed correction utilizes Shepard Functions in combination with a correction to derivative approximations. Incompleteness of the kernel support combined with the lack of consistency of the kernel interpolation in conventional meshless method results in fuzzy boundaries. In the presented meshless method, the domain boundary conditions and internal field variables are approximated with the default accuracy of the method. The resulting new scheme offers a higher order of accuracy, but also minimize the impact of the particle deficiency (kernel support incompleteness) problem. Furthermore, different kernel gradients and their impact on the property of the scheme and accuracy are discussed. The model was tested by solving an inhomogeneous Dirichlet and mixed boundary value problems for the Laplacian equation with good accuracy confirming our theoretical results. The accuracy of Schwaiger's scheme and new scheme is the same for homogeneous particle distribution and different for the distorted particles. The stability analysis shows that von Neumann growth factor has both real and imaginary parts forming complex shape for general particle distribution but satisfying the stability requirement almost everywhere.

As was previously mentioned in the introduction, several methods have been proposed to address the difficulties involved in calculating second-order derivatives with SPH. In contrast to the present formulation, many of these methods achieve a high accuracy through fully calculating the Hessian or requiring that the discrete equations exactly reproduce quadratic functions. The primary attraction of the present method is that it provides a weak formulation for Darcy's law which can be of use in further development of meshless methods. The SPH model was previously used to model three-dimensional miscible flow and transport in porous media with complex geometry, and we are planning to use this model in future work for large (field) scale simulation of transport in porous media with general permeability distributions.

Acknowledgment

The authors thank anonymous referees who contributed to the substantial improvement of the paper.

Appendix. Main symbols related to SPH discretization

The appendix comprises main notations of the symbols used in the SPH discretization in Table A.10.

Table A.10

Table of main symbols related to SPH discretization.

Symbol	Description
$\mathbf{L}()$	Laplace operator
$\langle\mathbf{L}()\rangle$	SPH discretization of Laplace operator
$\tilde{h}$ (or $\tilde{h}_I$)	Physical smoothing length at any particle (or around the particle I)
h_I	Characteristic smoothing length of the particle I (user defined)
h	Homogeneous particle smoothing length
$\tilde{h}_{max}$	Maximum physical smoothing length
$\tilde{h}_{IJ}$	Effective smoothing length between particles I and J
$\Delta\tilde{x}_I$ (or $\Delta\tilde{x}_I$)	Maximum distance between particles I and J inside control volume $\Omega_{\mathbf{r}_I,\tilde{h}_I}$
Δx	Homogeneous inter-particles distance
$\delta(\mathbf{r}-\mathbf{r}_I)$	Dirac delta function
$W\left(\mathbf{r}-\mathbf{r}_I,\tilde{h}_I\right)$	Kernel function (continuous case)
$\nabla W\left(\mathbf{r}-\mathbf{r}_I,\tilde{h}_I\right)$	Gradient of the kernel function (continuous case)
$dV_{\mathbf{r}}$ (or $dV_{\mathbf{r}_I}$ or $V_{\mathbf{r}_I}$)	Volume of the particle located at point $\mathbf{r}$ (or particle I)
$\mathbf{r}$ (or $\mathbf{r}_I$)	Point in Euclidean space
$\Omega_{\mathbf{r}_I,\tilde{h}_I}$	Support of the kernel
supp $W\left(\mathbf{r}-\mathbf{r}_I,\tilde{h}_I\right)$	Support of the kernel (i.e., $\Omega_{\mathbf{r}_I,\tilde{h}_I}$)
z_J	Dimensionless variable defined by $\left\|\mathbf{r}_J-\mathbf{r}_I\right\|_2/\tilde{h}_{IJ}$
$\overline{W}\left(\mathbf{r}_J-\mathbf{r}_I,\tilde{h}_{IJ}\right)$	Normalized kernel in discrete case
$\nu(\mathbf{r}_I)$	Inverse of the normalization factor in discrete case
$\overline{\nabla W}(\mathbf{r}_J-\mathbf{r}_I,\tilde{h}_{IJ})$	General notation for the gradient of kernel in discrete case
$\nabla_{\mathbf{r}_J}W\left(\mathbf{r}_J-\mathbf{r}_I,\tilde{h}_{IJ}\right)$	Gradient of kernel ("full derivatives") in discrete case (form 1)
$\nabla_{\mathbf{r}_I}\overline{W}\left(\mathbf{r}_J-\mathbf{r}_I,\tilde{h}_{IJ}\right)$	Gradient of kernel ("diffuse derivatives") in discrete case (form 1)
$\widetilde{\nabla}_{\mathbf{r}_I}\overline{W}\left(\mathbf{r}_J-\mathbf{r}_I,\tilde{h}_{IJ}\right)$	Gradient of kernel ("full derivatives") in discrete case (form 2)
$\overline{\nabla}_{\mathbf{r}_I}\overline{W}(\mathbf{r}_J-\mathbf{r}_I,\tilde{h}_{IJ})$	Gradient of kernel ("diffuse derivatives") in discrete case (form 2)
$\mathbf{C}$ or $\mathbf{C}_{\alpha\beta}$	Correction tensor or inverse of the distortion tensor in discrete case
$\mathbf{N}$	SPH correction vector
$\widetilde{\mathbf{N}}$	General form of SPH correction vector
Γ or $\Gamma_{\alpha\beta}$	Correction tensor to the SPH Hessian discretization
$\Gamma^*_{\alpha\beta}$ or $\Gamma^*_{\alpha\beta}$	Modified correction tensor to the SPH Hessian discretization
$\overline{\Gamma}$ or $\overline{\Gamma}_{\alpha\beta}$	Hybrid correction tensor to the SPH Hessian discretization

References

[1] L. Lucy, A numerical approach to testing the fission hypothesis, Astron. J. 82 (12) (1977) 1013–1024.
[2] R. Gingold, J. Monaghan, Smoothed particle hydrodynamics: theory and applications to non-spherical stars, Mon. Not.R. Astron. Soc. 181 (1977) 375–389.
[3] R. Gingold, J. Monaghan, Kernel estimates as a basis for general particle methods in hydrodynamics, J. Comput. Phys. 46 (3) (1982) 429–453.
[4] J. Monaghan, Smoothed particle hydrodynamics, Ann. Rev. Astron. Astrophys. 30 (1992) 543–574.
[5] T. Liszka, J. Orkisz, The finite difference method at arbitrary irregular grids and its applications in applied mechanics, Comput. Struct. 11 (1-2) (1980) 83–95.
[6] B. Nayroles, G. Touzot, P. Villon, Generalizing the finite element: diffuse approximation and defuse elements, Comput. Mech. 10 (5) (1992) 307–318.
[7] T. Belytschko, Y. Lu, L. Gu, Element-free Galerkin methods, Internat.J. Numer. Methods Engrg. 37 (2) (1994) 229–256.
[8] P. Krysl, T. Belytschko, Analysis of thin plates by the element-free Galerkin method, Comput. Mech. 17 (1-2) (1996) 26–35.
[9] S. Atluri, T. Zhu, A new meshless local Petrov-Galerkin (MPLG) approach in computational mechanics, Comput. Mech. 22 (2) (1998) 117–127.
[10] S. Atluri, J. Cho, H. Kim, Analysis of thin beams, using the meshless local Petrov-Galerkin (MLPG) method, with generalized moving least squares interpolation, Comput. Mech. 24 (5) (1999) 334–347.
[11] S. Li, W. Hao, W. Liu, Numerical simulation of large deformation of thin shell structures using meshfree methods, Comput. Mech. 25 (2000) 102–116.
[12] S. Atluri, S. Shen, The basis of meshless domain discretization: the meshless local Petrov - Galerkin (MLPG) method, Adv. Comput. Math. 23 (1–2) (2005) 73–93.
[13] W. Liu, S. Jun, F. Zhang, Reproducing kernel particle methods, Internat. J. Numer. Methods Fluids 20 (8-9) (1995) 1081–1106.
[14] W. Liu, S. Jun, Multiple-scale reproducing kernel particle method for large deformation problems, Internat.J. Numer. Methods Engrg. 41 (7) (1998) 1339–1362.
[15] G. Liu, M. Liu, Smoothed Particle Hydrodynamics: A Meshfree Particle Method, World Scientific Publishing Co. Pte. Ltd., 2003, p. 472.
[16] Y. Gu, G. Liu, A meshless local Petrov-Galerkin (MLPG) formulation for static and free vibration analysis of thin plates, Comput. Model. Eng. Sci. 2 (4) (2001) 463–476.
[17] Y. Gu, G. Liu, A boundary radial point interpolation method (BRPIM) for 2-D structural analyses, Struct. Eng. Mech. 15 (5) (2002) 535–550.
[18] G. Liu, Y. Gu, A local point interpolation method for stress analysis of two-dimensional solids, Struct. Eng. Mech. 11 (2) (2001) 221–236.
[19] C. Duarte, J. Oden, An HP adaptive method using clouds, Comput. Methods Appl. Mech. Engrg. 139 (1-4) (1996) 237–262.
[20] G. Yagawa, T. Yamada, Free mesh method: a new meshless finite element method, Comput. Mech. 18 (1996) 383–386.
[21] G. Liu, Mesh free method for stress analysis for solids, in: V. Shim, et al. (Eds.), Impact Response of Materials and Structures, Oxford, 1999, pp. 475–480.

[22] G. Fairweather, A. Karageorghis, The method of fundamental solutions for elliptic boundary value problems, Adv. Comput. Math. 9 (1998) 69–95.

[23] J. Lin, C. Chen, C.-S. Liu, J. Lu, Fast simulation of multi-dimensional wave problems by the sparse scheme of the method of fundamental solutions, Comput. Math. Appl. 72 (3) (2016) 555–567.

[24] K. Atkinson, The numerical evaluation of particular solutions for Poisson's equation, IMA J. Numer. Anal. 5 (1985) 319–338.

[25] A. Muleshkov, M. Golberg, C. Chen, Particular solutions of Helmholtz-type operators using higher order polyharmonic splines, Comput. Mech. 23 (5) (1999) 411–419.

[26] M. Golberg, A. Muleshkov, C. Chen, A.-D. Cheng, Polynomial particular solutions for certain partial differential operators, Numer. Methods Partial Differential Equations 19 (1) (2003) 112–133.

[27] J. Lin, C. Zhang, L. Sun, J. Lu, Simulation of seismic wave scattering by embedded cavities in an elastic half-plane using the Novel singular boundary method, Adv. Appl. Math. Mech. 10 (2) (2018) 322–342.

[28] S. Reutskiy, The backward substitution method for multipoint problems with linear Volterra–Fredholm integro-differential equations of the neutral type, J. Comput. Appl. Math. 296 (C) (2016) 724–738.

[29] J. Lin, S. Reutskiy, J. Lu, A Novel meshless method for fully nonlinear advection–diffusion-reaction problems to model transfer in anisotropic media, Appl. Math. Comput. 339 (C) (2018) 459–476.

[30] S. Li, W. Liu, Meshfree Particle Methods, Springer-Verlag. Berlin, 2003, p. 502.

[31] G. Liu, M. Liu, Smoothed Particle Hydrodynamics: A Meshfree Particle Method, World Scientific Publishing Co. Pte. Ltd., 2004, p. 449.

[32] D. Violeau, Fluid Mechanics and the SPH Method: Theory and Applications, Oxford University Press, 2012, p. 594.

[33] T. Belytschko, Y. Krongauz, J. Dolbow, C. Gerlach, On the completeness of meshfree particle methods, Internat.J. Numer. Methods Engrg. 43 (5) (1998) 785–819.

[34] J. Swegle, D. Hicks, S. Attaway, Smoothed particle hydrodynamics stability analysis, J. Comput. Phys. 116 (1) (1995) 123–134.

[35] T. Belytschko, Y. Guo, W. Liu, S. Xiao, A unified stability analysis of meshless particle methods, Internat.J. Numer. Methods Engrg. 48 (9) (2000) 1359–1400.

[36] C. Zhang, X. Hu, N. Adams, A generalized transport-velocity formulation for smoothed particle hydrodynamics, J. Comput. Phys. 337 (C) (2017) 216–232.

[37] A. Khayyer, H. Gotoh, Y. Shimizu, Comparative study on accuracy and conservation properties of two particle regularization schemes and proposal of an optimized particle shifting scheme in ISPH context, J. Comput. Phys. 332 (2017) 236–256.

[38] M. Liu, G. Liu, K. Lam, Computer simulation of high explosive explosion using smoothed particle hydrodynamics methodology, Comput. & Fluids 32 (3) (2003) 305–322.

[39] A. Lukyanov, Numerical modelling of the material failure under shock loading using particle method, Izvetiya Tula State Univ. Estestvennonauchn. Ser. 1 (2007) 54–65.

[40] A. Lukyanov, V. Penkov, Numerical simulation of solids deformation by a meshless method, Vestn. Samar. Gos. Univ. Estestvennonauchn. Ser. 6 (56) (2007) 62–70.

[41] J. Monaghan, Simulating free surface flows with SPH, J. Comput. Phys. 110 (2) (1994) 399–406.

[42] G. Johnson, R. Stryk, S. Beissel, SPH for high velocity impact computations, Comput. Methods Appl. Mech. Eng. 139 (1-4) (1996) 347–373.

[43] J. Chen, J. Beraun, C. Jih, Completeness of corrective smoothed particle method for linear elastodynamics, Comput. Mech. 24 (4) (1999) 273–285.

[44] J. Chen, J. Beraun, C. Jih, A corrective smoothed particle method for transient elastoplastic dynamics, Comput. Mech. 27 (3) (2001) 177–187.

[45] J. Morris, P. Fox, Y. Zhu, Modeling low Reynolds number incompressible flows using SPH, J. Comput. Phys. 136 (1) (1997) 214–226.

[46] D. Holmes, J. Williams, P. Tilke, Smooth particle hydrodynamics simulations of low Reynolds number flows through porous media, Int. J. Numer. Anal. Methods Geomech. 35 (4) (2011) 419–437.

[47] Y. Zhu, P. Fox, J. Morris, A pore-scale numerical model for flow through porous media, Int. J. Numer. Anal. Methods Geomech. 23 (9) (1999) 881–904.

[48] Y. Zhu, P. Fox, Smoothed particle hydrodynamics model for diffusion through porous media, Transp. Porous Media 43 (3) (2001) 441–471.

[49] A. Chaniotis, D. Poulikakos, P. Koumoutsakos, Remeshed smoothed particle hydrodynamics for the simulation of viscous and heat conduction flows, J. Comput. Phys. 182 (1) (2002) 67–90.

[50] H. Schwaiger, An implicit corrected SPH formulation for thermal diffusion with linear free surface boundary conditions, Internat. J. Numer. Methods Engrg. 75 (6) (2008) 647–671.

[51] J. Monaghan, Smoothed particle hydrodynamics and its diverse applications, Annu. Rev. Fluid Mech. 44 (1) (2012) 323–346.

[52] E. Keilegavlen, I. Aavatsmark, Monotonicity for MPFA methods on triangular grids, Comput. Geosci. 15 (1) (2011) 3–16.

[53] L. Brookshaw, A method of calculating radiative heat diffusion in particle simulations, Proc. Astron. Soc. Aust. 6 (2) (1985) 207–210.

[54] N. Quinlan, M. Basa, M. Lastiwka, Truncation error in mesh-free particle methods, Internat. J. Numer. Methods Engrg. 66 (2006) 2064–2085.

[55] D. Fulk, D. Quinn, An analysis of 1-D smoothed particle hydrodynamics kernels, J. Comput. Phys. 126 (1) (1996) 165–180.

[56] S. Li, W. Liu, Meshfree and particle methods and their applications, Appl. Mech. Rev. 55 (1) (2002) 1–34.

[57] P. Breitkopf, A. Huerta, Meshless & Particle Based Approaches in Computational Mechanics, ISTE Publishing Company, 2004, p. 176.

[58] S. Mas-Gallic, P. Raviart, A particle method for first-order symmetric systems, Numer. Math. 51 (3) (1987) 323–352.

[59] P. Randles, L. Libersky, Smoothed particle hydrodynamics: some recent improvements and applications, Comput. Methods Appl. Mech. Eng. 139 (1–4) (1996) 375–408.

[60] M. Doring, Développement d'une Méthode SPH Pour Les Applications à Surface Libre en Hydrodynamique (Ph.D. thesis), Ecole Centrale Nantes, 2005.

[61] S. Marrone, A. Colagrossi, D.L. Touzé, G. Graziani, Fast free-surface detection and level-set function definition in SPH solvers, J. Comput. Phys. 229 (10) (2010) 3652–3663.

[62] J. Chen, J. Beraun, T. Carney, A corrective smoothed particle method for boundary value problems in heat conduction, Internat.J. Numer. Methods Engrg. 46 (2) (1999) 231–252.

[63] J. Chen, J. Beraun, C. Jih, An improvement for tensile instability in smoothed particle hydrodynamics, Comput. Mech. 23 (4) (1999) 279–287.

[64] J. Bonet, S. Kulasegaram, Correction and stabilization of smooth particle hydrodynamics methods with applications in metal forming simulations, Internat. J. Numer. Methods Engrg. 47 (6) (2000) 1189–1214.

[65] F. Colin, R. Egli, F. Lin, Computing a null divergence velocity field using smoothed particle hydrodynamics, J. Comput. Phys. 217 (2) (2006) 680–692.

[66] P. Cleary, J. Monaghan, Conduction modelling using smoothed particle hydrodynamics, J. Comput. Phys. 148 (1) (1999) 227—264.

[67] M. Jubelgas, V. Springel, K. Dolag, Thermal conduction in cosmological SPH simulations, Mon. Not. R. Astron. Soc. 351 (2) (2004) 423–435.

[68] S. Cummins, M. Rudman, An SPH projection method, J. Comput. Phys. 152 (2) (1999) 584–607.

[69] E. Lee, C. Moulinec, R. Xu, D. Violeau, D. Laurence, P. Stansby, Comparison of weakly compressible and truly incompressible algorithms for the SPH mesh free particle method, J. Comput. Phys. 227 (18) (2008) 8417–8436.

[70] X. Hu, N. Adams, A multi-phase SPH method for macroscopic and mesoscopic flows, J. Comput. Phys. 213 (2) (2006) 844–861.

[71] S. Zhang, S. Kuwabara, T. Suzuki, Y. Kawano, K. Morita, K. Fukuda, Simulation of solid-fluid mixture flow using moving particle methods, J. Comput. Phys. 228 (7) (2009) 2552–2565.

[72] W. Pan, K. Kim, M. Perego, A. Tartakovsky, M. Parks, Modeling electrokinetic flows by consistent implicit incompressible smoothed particle hydrodynamics, J. Comput. Phys. 334 (2017) 125–144.

[73] J. Fang, A. Parriaux, A regularized Lagrangian finite point method for the simulation of incompressible viscous flows, J. Comput. Phys. 227 (20) (2008) 8894–8908.

[74] J. Bonet, T. Lok, Variational and momentum preservation aspects of smoothed particle hydrodynamic formulations, Comput. Methods Appl. Mech. Engrg. 180 (1–2) (1999) 97–115.

[75] W. Liu, S. Jun, F. Zhang, Reproducing kernel particle methods, Internat. J. Numer. Methods Fluids 20 (8–9) (1995) 1081–1106.

[76] P. Diehl, M. Schweitzer, Efficient Neighbor Search for Particle Methods on GPUs, INS Preprint No. 1405, 2014.

[77] J. Onderik, R. Ďurikovič, Efficient neighbor search for particle-based fluids, J. Appl. Math. Stat. Inform. 2 (3) (2007).

[78] A.A. Lukyanov, C. Vuik, Meshless multi-point flux approximation, in: E. Griebel, M.A. Schweitzer (Eds.), Meshfree Methods for Partial Differential Equations, 2017, pp. 67–84.

[79] S. Silling, Reformulation of elasticity theory for discontinuities and long-range forces, J. Mech. Phys. Solids 48 (1) (2000) 175–209.

[80] A. Katiyar, J. Foster, H. Ouchi, M. Sharma, A peridynamic formulation of pressure driven convective fluid transport in porous media transport in porous media, J. Comput. Phys. 261 (2014) 209–229.

[81] F. Bouchon, Monotonicity of some perturbations of irreducibly diagonally dominant M-matrices, Numer. Math. 105 (4) (2007) 591–601.

[82] F. Bouchon, G. Peichl, A second order immersed interface technique for an elliptic Neumann problem, Numer. Methods Partial Differential Equations 23 (2) (2007) 400–420.

[83] N. Matsunaga, T. Yamamoto, Superconvergence of the Shortley–Weller approximation for Dirichlet problems, J. Comput. Appl. Math. 116 (2) (2000) 263–273.

[84] V. Thomée, From finite differences to finite elements. A short history of numerical analysis of partial differential equations, J. Comput. Appl. Math. 128 (1–2) (2001) 1–54.

[85] K.-A. Lie, An Introduction to Reservoir Simulation using Matlab: User Guide for the Matlab Reservoir Simulation Toolbox (MRST), SINTEF ICT, 2016, p. 392.

[86] M. Christie, M. Blunt, Tenth SPE comparative solution project: A comparison of upscaling techniques, in: SPE 66599, presented at the SPE Symposium on Reservoir Simulation, Houston, 2001.